

DEPARTAMENTO DE MATEMÁTICA APLICADA

**HIGH ORDER ACCURATE SHOCK CAPTURING SCHEMES
FOR HYPERBOLIC CONSERVATION LAWS BASED ON A
NEW CLASS OF LIMITERS**

SUSANA SERNA SALICHES

**UNIVERSITAT DE VALENCIA
Servei de Publicacions
2005**

Aquesta Tesi Doctoral va ser presentada a València el dia 15 de Febrer de 2005 davant un tribunal format per:

- D. Alfredo Bermúdez De Castro López-Varela
- D. José María Ibáñez Cabanell
- D. Francisco Michavila Pitarch
- D. Hans Joachim Schroll
- D. Javier De Frutos Baraja

Va ser dirigida per:

D. Antonio Marquina Vila

©Copyright: Servei de Publicacions
Susana Serna Salichs

Depòsit legal:

I.S.B.N.:84-370-6148-2

Edita: Universitat de València
Servei de Publicacions
C/ Artes Gráficas, 13 bajo
46010 València
Spain
Telèfon: 963864115

UNIVERSIDAD DE VALENCIA

**High Order Accurate Shock Capturing Schemes
for Hyperbolic Conservation Laws based on a
new Class of Limiters**

A dissertation submitted for the degree

Doctor en Ciencias Matemáticas, especialidad Matemática Aplicada

by

Susana Serna Salichs

2005

Prof. Antonio Marquina Vila, Catedrático de Matemática Aplicada de la Facultad de Matemáticas de la Universidad de Valencia,

Certifica:

Que la presente memoria, *High Order Accurate Shock Capturing Schemes for Hyperbolic Conservation Laws based on a new Class of Limiters*, ha sido realizada bajo mi dirección por Susana Serna Salichs, Licenciada en Ciencias Matemáticas, y constituye su Tesis para optar al grado de Doctor en Ciencias Matemáticas.

Valencia, dos de diciembre de 2004

Antonio Marquina Vila

A todos los que han creido en este proyecto . . .

TABLE OF CONTENTS

1	Introduction	1
2	Shock Capturing Methods for Hyperbolic Conservation Laws .	5
3	An extended class of limiters	19
3.1	Introduction	19
3.2	Power limiters	24
4	Piecewise Smooth Reconstructing Functions	31
4.1	Introduction	31
4.2	Hyperbolic reconstructions	37
4.2.1	Power Piecewise Hyperbolic Method	38
4.3	Parabolic reconstructions	44
4.3.1	PowerENO method	45
4.3.2	Weighted PowerENO method	48
5	Numerical Experiments	61
5.1	Introduction	61
5.2	Numerical Implementation	61
5.3	Euler equations	68
5.4	PowerPHM method. Experiments	71

5.4.1	Linear advection	71
5.4.2	Euler equations: One dimensional experiments	73
5.4.3	Euler equations: Two-dimensional Riemann problem . . .	76
5.5	Power ENO and Weighted Power ENO methods. Experiments . .	76
5.5.1	Study of convergence	76
5.5.2	Linear advection	80
5.5.3	Euler equations: One dimensional experiments	83
5.5.4	Euler equations: Two-dimensional Riemann Problems . . .	90
5.5.5	Euler equations: Two dimensional Mach 3 Wind Tunnel with a Step	93
6	Applications: Numerical simulations of Rayleigh-Taylor and Richtmyer-Meshkov Instabilities	99
6.1	Introduction	99
6.2	Rayleigh-Taylor instability	100
6.3	Richtmyer-Meshkov instability	101
6.3.1	Model equations	103
6.3.2	One dimensional model problems	106
6.3.3	Two-dimensional problems	107
7	Summary and Conclusions	117
References		119

8 Resumen de la Memoria en castellano	123
8.1 Introducción	123
8.2 Métodos de Captura de Ondas de Choque para Leyes de Conservación Hiperbólicas	126
8.3 Una clase extendida de limitadores	128
8.3.1 Power limiters	131
8.4 Funciones de reconstrucción suaves a trozos	135
8.4.1 Reconstrucciones Hiperbólicas	142
8.4.2 Reconstrucciones parabólicas	146
8.5 Experimentos Numéricos	158
8.6 Aplicaciones: Simulaciones Numéricas de inestabilidades de Rayleigh-Taylor y Richtmyer-Meshkov	160
8.7 Resumen y Conclusiones	160
References	163

LIST OF FIGURES

3.1 Second order TVD region and $\phi^3(\theta)$	28
4.1 A comparison of smoothness measurements for a jump discontinuity: Weighted Power ENO5 (top), WENO5 (bottom)	56
4.2 A comparison of smoothness measurements for two discontinuities in derivative: Weighted Power ENO5 (top), WENO5 (bottom).	57
5.1 Numerical solution of linear advection at $t=10$, $CFL=0.8$ and 200 points for PHM-GOD scheme “+” and PowerPHM-GOD schemes “o”.	72
5.2 Numerical solution of the density profile for the Lax’s problem at $t=1.3$, $CFL=0.8$, 200 points for the PHM-MFF scheme “+” and PowerPHM-MFF scheme “o”.	74
5.3 Zoomed regions of the density profile of Lax’s problem	74
5.4 Zoomed region of the numerical solution of the density profile for the shock-entropy wave interaction with PHM-MFF “+” and PowerPHM-MFF “o”, using a grid of 200 points with $CFL=0.8$ until time 1.8	75
5.5 Zoomed region of the density contour lines of the numerical solution of the two-dimensional Riemann problem using 400×400 points, $CFL=0.8$, at time 0.8 for the PHM-MFF scheme (left) and PowerPHM-MFF (right).	77

5.6 Comparison of the numerical solution of linear advection of Example 1 for ENO3 "+" and PowerENO3 "o"	81
5.7 Comparison of the numerical solution of linear advection of Example 2 for ENO3 "+" and PowerENO3 "o"	82
5.8 Comparison of the numerical solution of linear advection. Example 1 for WENO5 "+" , WPowerENO5 "o"	83
5.9 Comparison of the numerical solution of linear advection of Example 2 for WENO5 "+" , WPowerENO5 "o"	84
5.10 Numerical solution of the density profile for the Sod's Tube for WENO5-MFF "+" and WPowerENO5-MFF "o"	85
5.11 Numerical solution of the density profile for the Lax's Tube for WENO5-MFF "+" , WPowerENO5-MFF "o". Bottom, zoomed regions	86
5.12 Numerical solution of the density profile of the Shock entropy wave interaction for WENO5 "+" and WPowerENO5 "o". Zoomed regions.	88
5.13 Numerical solution of the density profile of the Two interacting blast waves for: WENO5 left pictures with 400 and 800 points and WPowerENO5 right pictures with 400 and 800 points	89
5.14 Top: Density profile of the Four contacts problem for WENO5 (left), WPowerENO5 (right). Bottom: Zoomed vortex regions.	91

5.15 Top, section of density profile at $x = 0.2575$. Bottom, zoomed regions of the x-section. WENO5 "+" , WPowerENO5 "o"	92
5.16 Zoomed region of the density profile for the Four shocks problem: WENO5 (Top), WPowerENO5 (Bottom)	94
5.17 Density profile, WENO5 (top), WPowerENO5 (bottom)	96
5.18 Adiabatic constant P/ρ^γ , WENO5 (top), WPowerENO5 (bottom)	97
5.19 Sections of density profile at $x = 0.8$ (left) and $y = 0.5$ (right), WENO5 '+' , WPowerENO5 'o'	97
6.1 Comparison of the numerical solution of the Rayleigh-Taylor instability for MFF-WENO5 (left) and MFF-Weighted PowerENO (right).	102
6.2 Density and Pressure profiles of the Helium-Air case for Weighted PowerENO method. Bottom, zoom of the spike region of the pressure	108
6.3 Density and Pressure profiles of the R22-Air case for Weighted PowerENO method. Bottom, zoom of the spike region of the pressure	109
6.4 Two dimensional initial data for the Richtmyer-Meshkov instability	110
6.5 Snapshots of the Air-He Richtmyer-Meshkov instability evolution	112
6.6 Snapshots of the Air-R22 Richtmyer-Meshkov instability evolution	113
6.7 Comparison of the numerical solution of the Air-Helium RM instability for MFF-PowerPHM (left), MFF-WENO5 (center) and MFFWeighted PowerENO (right).	114

6.8 Comparison of the numerical solution of the Air-R22 RM instability for MFF-PowerPHM (left), MFF-WENO5 (center) and MFF-Weighted PowerENO (right)	115
--	-----

LIST OF TABLES

5.1	<i>Third order TVD Runge-Kutta scheme</i>	63
5.2	<i>Absolute Errors for Weighted Power ENO5 and WENO5 methods</i>	78
5.3	<i>Numerical Orders for Weighted Power ENO5 and WENO5 methods</i>	79
5.4	<i>Absolute Errors for Weighted Power ENO5 and WENO5, excluding inflection points</i>	79

ACKNOWLEDGMENTS

First, I would like to thank Vicente F. Candela for his encouragement, support and friendship. I am indebted to him for all his help.

I deeply want to thank my advisor Antonio Marquina for his dedication, good advice, confidence, guidance, friendship and great support during the last four years.

I want to thank especially Prof. Stanley Osher for his kind invitation and all the people in the UCLA Math Department who helped me during my year there.

Thanks are also due to Prof. Ewald Muller and the people of the Max-Planck-Institut fur Astrophysik, for all the human and material resources they offered me during my stay there.

I heartedly thank Prof. Schroll and the people at the Department of Numerical Analysis, Lund University, to make my life easier during my stay, for the warm welcome and friendly atmosphere I enjoyed.

I owe an especial acknowledgement to Prof. Russo for his careful reading of this work and his exhaustive correction and many valuable suggestions.

I want to thank Prof. Kroener, Prof. Russo and Prof. Schroll for accepting to write a report on this thesis.

I would like to express my gratitude to many friends who backed me up and, specially, my to my parents who have always supported me and my decisions.

Finally, I acknowledge the confidence and great support of my friends Vicente and Antonio.

DISSERTATION

**High Order Accurate Shock Capturing Schemes
for Hyperbolic Conservation Laws based on a
new Class of Limiters**

by

Susana Serna Salichs

Departamento de Matemática Aplicada

Universidad de Valencia, 2005

CHAPTER 1

Introduction

Hyperbolic systems of conservation laws have been used as models for a wide variety of physical phenomena, from aerodynamics to hydrodynamical models for semiconductors through astrophysical flows and weather prediction. Our field of interest focuses on the numerical approximation of the solution of systems of conservation laws with high order accuracy in space. The qualitative properties of the solution of systems of conservation laws make their numerical simulation particularly interesting since they develop jump discontinuities in finite time and fine structure near non stable interfaces. The accurate numerical simulation of the time evolution of these processes is important to explain and predict natural phenomena and to use it in industrial applications.

Along the last forty years a great progress has taken place in the research and development of high order accurate shock capturing schemes for numerical simulation of complex flows, starting from the original work by S.K. Godunov in 1959. The introduction of essentially non oscillatory (ENO) schemes in the eighties using polynomial interpolation as the main ingredient of high accurate shock capturing schemes, has been the turning point to consider the research of new piecewise smooth reconstructing functions a field of increasing research

interest in computational fluid dynamics.

The main goal of high order methods is to reduce smearing at discontinuities with high accuracy along the smooth regions of the flow.

This research work focuses on the investigation of high order shock capturing schemes based on reconstructing procedures that reduce smearing at discontinuities, avoid spurious oscillations and resolve smooth regions of the flow with high order accuracy in space. We explore non oscillatory piecewise polynomial and non polynomial reconstructing functions, with total variation near discontinuities locally bounded.

In this research work we introduce some new high order accurate shock capturing schemes that improve the behavior of essentially non oscillatory schemes at jump discontinuities. We construct and analyze various reconstructions procedures for the approximation of the solution of hyperbolic conservation laws, based on a new class of limiter functions that we have introduced for this purpose. Numerical tests are presented to show the good behavior of the proposed schemes. We apply our schemes to compute Richtmyer-Meshkov and Rayleigh-Taylor instabilities.

Chapter 2 is devoted to a general overview on numerical methods for hyperbolic conservation laws, focused on the essentials of the so-called shock capturing schemes. We have included a discussion on the main issues concerning the high order accurate numerical approximation of the solution of hyperbolic conservation laws, that is, numerical diffusion and spurious oscillations.

In Chapter 3 we make an analysis of the role of the limiter functions in

the design of high order accurate conservative finite difference methods and we introduce a new extended class of limiter functions, the power limiters, that include some of the classical ones. We present a closer study of the power limiters in the context of the Total Variation Diminishing Lax-Wendroff based methods and we propose the *powermod* and *powereno* limiters, satisfying the necessary properties to be useful for the design of non oscillatory reconstruction procedures.

Chapter 4 is dedicated to the study of piecewise smooth reconstructions as the essential tool for the design of high order accurate shock capturing schemes. We make an analysis of the piecewise hyperbolic reconstructions using the powermod and powereno limiters instead of the harmonic ones to limit the first order divided differences and we show that the resulting method is local total variation bounded. We explore the use of the power limiters in the piecewise parabolic reconstruction by means of limiting the consecutive second order differences. We obtain an improvement of the third order accurate ENO method we call Power ENO method. At the end of this chapter we introduce a fifth order accurate Weighted Power ENO method as a nonlinear convex combination of the three Power ENO parabolas, obtaining a new method that improves the behavior of the classical fifth order Weighted ENO, (WENO), method near discontinuities.

After this analytical approach, we go into the numerical results. In Chapter 5 we present a set of numerical tests using the standard model problems to verify numerically the accuracy, stability and convergence of the different high order accurate schemes presented in this work.

In Chapter 6 we show an application of our schemes to the resolution of

Rayleigh-Taylor and Richtmyer-Meshkov instabilities, to demonstrate the ability of the proposed schemes to capture subscales of the flow.

CHAPTER 2

Shock Capturing Methods for Hyperbolic Conservation Laws

A continuum model for a physical system is described by laws of conservation of mass, momentum and energy. A conservation law for a physical quantity is a balance equation establishing that the rate of change of the total amount contained in some region G is given by its flux (convective or diffusive) through the region boundary, plus other possible internal sources. The integral form of this conservation law is

$$\frac{d}{dt} \int_G u dV + \int_{\partial G} \bar{f}(u) \cdot \bar{n} dS = \int_G s(u) dV \quad (2.1)$$

where u is the density of the conserved quantity, $f(u)$ is the flux and $s(u)$ is the source rate.

By using G to be an infinitesimal volume and applying the divergence theorem we obtain the differential form for the conservation law,

$$\frac{\partial u}{\partial t} + \nabla \cdot \bar{f}(u) = s(u) \quad (2.2)$$

which is the formulation for the numerical modelling of continuum physical systems.

We can write a system of conservation laws as:

$$u_t^i + \nabla \cdot \bar{f}^i = 0, \quad i = 1, \dots, s \quad (2.3)$$

where $\bar{u}(x, t) = (u^1, u^2, \dots, u^s)$ and its initial state is given by

$$u_t^i(x, 0) = u_0^i(x) \quad (2.4)$$

A system of conservation laws is said to be **hyperbolic** if the Jacobian in each spatial direction is locally diagonalizable with real eigenvalues in every neighborhood of the solution.

Many of the fundamental ideas were developed for compressible flows (Euler equations) for applications in aerodynamics, astrophysics, detonation waves and related flows where shock waves arise. Those flows are modelled by using convective fluxes only, and they are written as a hyperbolic system of conservation laws as defined before.

We restrict our discussion to the one-dimensional case for the aim of clarity. A hyperbolic system of conservation laws in one space dimension is written as:

$$\frac{\partial}{\partial t} u^i + \frac{\partial}{\partial x} f^i = 0, \quad i = 1, \dots, s \quad (2.5)$$

and the Jacobian of the system flux \bar{f} is:

$$(\bar{f}')_{ij} = \frac{\partial f^i}{\partial u^j}, \quad j = 1, \dots, s \quad (2.6)$$

When the flux is nonlinear, i.e., the Jacobian depends on u , the numerical approximation of the solution is a difficult problem because the solution develops discontinuities (shock waves, contact discontinuities) in finite time that propagate with finite speed.

From the above we conclude that “convective fluxes” (the ones appearing in hyperbolic conservation laws), require specialized numerical treatment. However, diffusive and reactive effects can be treated with standard numerical methods such as central differencing. Stiff reactive terms can present numerical difficulties added to the ones of convective terms.

The meaningful physical phenomena described by hyperbolic conservation laws are, ([3], [16], [14] and [19]):

1. **Advective transport** (Bulk convection) is simply bulk movement of matter (flow velocity).
2. **Waves**, which are small-amplitude smooth disturbances that propagate at the “speed of sound” in the system, depending on the physical properties of the media.
3. **Contact discontinuities** which are discontinuous jumps in mass density moving by bulk convection. For example, a contact separating oil from water.
4. **Shock waves.** A shock is a spatial jump in material magnitudes, like pressure, that develops spontaneously in a smooth flow and self-maintains.

5. **Rarefaction waves.** A rarefaction wave is a smooth expansion wave that propagates at the sound speed, relative to the flow velocity.

The analysis of numerical methods for compressible flows is studied in simpler equations, used as model problems, to check their stability, consistency, accuracy and convergence although the ultimate goal is their application to the Euler equations.

The model problems used for this purpose are

1. Linear advection:

$$u_t + cu_x = 0, \quad c = \text{constant}. \quad (2.7)$$

The analytic solution is expressed in terms of the initial state u_0 as

$$u(x, t) = u(x - ct, 0) = u_0(x - ct) \quad (2.8)$$

2. Nonlinear scalar conservation law:

$$u_t + f(u)_x = 0 \quad (2.9)$$

The inviscid Burgers equation

$$u_t + \left(\frac{u^2}{2} \right)_x = 0, \quad u(x, 0) = u_0(x) \quad (2.10)$$

is the most important example used to check stability and accuracy

- 3. Hyperbolic systems:** The one-dimensional Euler equations for ideal gas dynamics is the most important model for systems of hyperbolic conservation laws. The one-dimensional system is

$$\bar{u}_t + \bar{f}(\bar{u})_x = 0, \quad \bar{u} = (\rho, M, E)^T, \quad f(\bar{u}) = v\bar{u} + (0, P, vP) \quad (2.11)$$

where ρ , v , M , E and P are the density, velocity, momentum, energy and pressure respectively. The momentum is computed by $M = \rho v$ and the pressure is computed by means of the ideal equation of state (EOS),

$$P = (\gamma - 1)\rho\epsilon \quad (2.12)$$

where γ is the adiabatic exponent and ϵ is the specific internal energy related to the total energy E , by

$$E = \frac{1}{2}\rho v^2 + \rho\epsilon \quad (2.13)$$

The most successful strategy for the design of numerical schemes to approximate the solution of hyperbolic conservation laws is to follow Godunov's idea ([8]), i.e., to solve an initial value problem consisting of two constant states in every interface of the computational grid (this specific problem is called the Riemann problem) and then, integrate the conservation law in every computational cell computing the fluxes through the interfaces using the solution of this Riemann problem.

The numerical schemes based on the exact (approximate) solution of the Riemann problem have been the paradigm of the so-called *shock capturing schemes* originally introduced by Godunov.

We consider a nonlinear scalar conservation law in one space dimension,

$$u_t + f(u)_x = 0 \quad (2.14)$$

together with the initial data

$$u(x, 0) = u_0(x) \quad (2.15)$$

Let $x_j = jh$ be the spatial discretization (with h the spatial step), $t_n = n\Delta t$, the time discretization, (Δt the time step), $I_j = [x_{j-\frac{1}{2}}, x_{j+\frac{1}{2}}]$ the spatial cell, where $x_{j+\frac{1}{2}} = x_j + \frac{h}{2}$ is the cell interface, and $C_j^n = [x_{j-\frac{1}{2}}, x_{j+\frac{1}{2}}] \times [t_n, t_{n+1}]$ the computational cell. Let u_j^n be an approximation of the mean value in I_j ,

$$u_j^n = \frac{1}{h} \int_{x_{j-\frac{1}{2}}}^{x_{j+\frac{1}{2}}} u(x, t_n) dx \quad (2.16)$$

of the exact solution $u(x, t_n)$ of the initial value problem.

Integrating the conservation law in C_j^n we have that

$$V(j, n) = \int \int_{C_j}^n [u_t + f(u)_x] dx dt = 0 \quad (2.17)$$

Applying the divergence theorem we obtain:

$$\frac{1}{h} \int_{I_j} u(x, t_{n+1}) dx = \frac{1}{h} \int_{I_j} u(x, t_n) dx - \frac{\Delta t}{h} [G_{j+\frac{1}{2}}^n - G_{j-\frac{1}{2}}^n] \quad (2.18)$$

where (numerical) fluxes at the interfaces are

$$G_{j+\frac{1}{2}}^n = \frac{1}{\Delta t} \int_{t_n}^{t_{n+1}} f(u(x_{j+\frac{1}{2}}, s)) ds \quad (2.19)$$

$$G_{j-\frac{1}{2}}^n = \frac{1}{\Delta t} \int_{t_n}^{t_{n+1}} f(u(x_{j-\frac{1}{2}}, s)) ds \quad (2.20)$$

Thus we obtain the so-called conservation form

$$u_j^{n+1} = u_j^n - \frac{\Delta t}{h} \left[G_{j+\frac{1}{2}}^n - G_{j-\frac{1}{2}}^n \right] \quad (2.21)$$

where u_j^n represents the mean value of the solution $u(x, t_n)$ in the cell I_j . Hence, we introduce the following concept:

Definition 1 *A numerical scheme of the form:*

$$u_j^{n+1} = u_j^n - \frac{\Delta t}{h} (g_{j+\frac{1}{2}}^n - g_{j-\frac{1}{2}}^n) \quad (2.22)$$

is “conservative” if $g_{j+\frac{1}{2}}^n$ called “numerical flux” is a function of the neighboring values:

$$g_{j+\frac{1}{2}}^n = g(u_{j-L}^n, \dots, u_j^n, \dots, u_{j+R}^n)$$

where R and L are nonnegative integers and g is consistent with the flux of the equation (2.14), i.e.

$$g(u, u, \dots, u, u) = f(u)$$

Using the Theorem of Lax and Wendroff (1960), ([17]), we know that if a scheme in conservation form converges, then the limit is a weak solution of the conservation law (2.14). A piecewise smooth function which satisfies the equation in the smooth regions is a weak solution if and only if the Rankine-Hugoniot jump condition is satisfied at discontinuities, i.e., the velocity of the discontinuity is the ratio between the difference of the fluxes at both sides of the discontinuity and the difference of the values of the solution (Lax, [16]). Indeed, if s is the discontinuity speed then $[f(u)] = s[u]$ where $[u] = u_R - u_L$ and $[f(u)] = f(u_R) - f(u_L)$

being u_L and u_R the values of u at the left and the right side of the discontinuity respectively.

There are many weak solutions to (2.14)-(2.15), but there is only one which is physically consistent being the limit of the parabolic regularization

$$u_t + f(u)_x = \epsilon u_{xx}$$

with $\epsilon \downarrow 0$ ($\epsilon > 0$). This unique weak solution is characterized by means of the “entropy condition” that can be expressed in terms of the flux of the equation (see Lax, [16]). The discussion on this point is out of the scope of this research.

The unique entropy satisfying weak solution to (2.14)-(2.15) satisfies the following maximum principle:

Theorem 1 (Douglis-Oleinik) *[J. Smoller,[37]] The solution operator for the initial value problem (2.14)-(2.15), $u(x, t) = S_t[u(x, 0)]$, is monotone, i.e., if $u_0 \leq v_0$ then $S_t[u_0] \leq S_t[v_0]$.*

A numerical scheme is said to be monotone if the scheme preserves the order of the initial data exactly as in the continuous case.

Hence, a numerical scheme of the form

$$u_j^{n+1} = F(u_{j-L}^n, \dots, u_j^n, \dots, u_{j+R}^n) \quad (2.23)$$

is monotone if F is monotone for each variable.

Using the maximum principle it can be shown that a monotone numerical scheme in conservation form converges to the unique weak solution satisfying the entropy condition (Godunov, ([19])).

The most important monotone schemes are:

1. LAX-FRIEDRICH ([15, 14, 19]):

The Lax-Friedrichs scheme is defined by

$$u_j^{n+1} = u_j^n - \frac{\Delta t}{h} \left(g_{LF}(u_j^n, u_{j+1}^n) - g_{LF}(u_{j-1}^n, u_j^n) \right) \quad (2.24)$$

where

$$g_{LF}(u, v) := \frac{1}{2} \left[f(u) + f(v) \right] - \frac{1}{2} \frac{h}{\Delta t} [v - u] \quad (2.25)$$

This scheme is monotone provided the following Courant-Friedrichs-Lowy, (CFL), restriction on the ratio $\lambda := \frac{\Delta t}{h}$,

$$|\lambda \cdot f'| < 1. \quad (2.26)$$

is satisfied.

2. ENGQUIST-OSHER ([5]): We define $g^+ := \max(g, 0)$ and $g^- := \min(g, 0)$, for an arbitrary function g . We consider a reference value \bar{u} that could be taken a “sonic point”, i.e., $f'(\bar{u}) = 0$ and we define

$$f_-(u) = \int_{\bar{u}}^u [f'(s)]^- ds, \quad (2.27)$$

and

$$f_+(u) = \int_{\bar{u}}^u [f'(s)]^+ ds. \quad (2.28)$$

Then, from

$$g_{EO}(u, v) := f_+(v) + f_-(u) \quad (2.29)$$

we define the Engquist-Osher scheme, ([5]), as the one given by

$$u_j^{n+1} = u_j^n - \frac{\Delta t}{h} \left[g_{EO}(u_j^n, u_{j+1}^n) - g_{EO}(u_{j-1}^n, u_j^n) \right] \quad (2.30)$$

This scheme is conservative and monotone under the same CFL restriction as the Lax-Friedrichs scheme. This scheme is upwind, which means that if $f'(u) > 0$ for u running in the interval defined by u_{j-1}^n and u_{j+1}^n , then $g_{EO}(u_{j-1}^n, u_j^n) = f(u_{j-1}^n)$ and $g_{EO}(u_j^n, u_{j+1}^n) = f(u_j^n)$, and if $f'(u) < 0$ for u running in the same interval then $g_{EO}(u_{j-1}^n, u_j^n) = f(u_j^n)$ and $g_{EO}(u_j^n, u_{j+1}^n) = f(u_{j+1}^n)$,

3. GODUNOV ([8]):

The Godunov scheme is based on the solution of a sequence of Riemann problems located at the interfaces. More precisely, for each j we consider the Riemann problem localized at the interface $x_{j+\frac{1}{2}}$ at time t_n

$$u_t + f(u)_x = 0 \quad (2.31)$$

with the initial data:

$$u(x, t_n) := \begin{cases} u_j^n, & \text{if } x_{j-1/2} \leq x < x_{j+1/2}; \\ u_{j+1}^n, & \text{if } x_{j+1/2} < x \leq x_{j+3/2}. \end{cases} \quad (2.32)$$

The solution for short time, i.e., satisfying a CFL restriction in a way that the solution of each Riemann problem does not interact to the ones of the next cells, is a self-similar function of the form

$$u_\Delta(x, t) = V\left(\frac{x - x_{j+1/2}}{t - t_n}, u_j^n, u_{j+1}^n\right) \quad (2.33)$$

The Godunov scheme is defined as

$$u_j^{n+1} = u_j^n - \frac{\Delta t}{h} [g_{GOD}(u_j^n, u_{j+1}^n) - g_{GOD}(u_{j-1}^n, u_j^n)] \quad (2.34)$$

where

$$g_{GOD}(u_j^n, u_{j+1}^n) := f(V(0, u_j^n, u_{j+1}^n)) \quad (2.35)$$

is the so-called **Godunov flux**.

The Godunov scheme is conservative and monotone since it is the composition of two monotone operators namely, the one giving the exact solution of the local Riemann problems (Douglis-Oleinik theorem) and the cell average operator under the restriction $|\frac{\Delta t}{h} f'| < 1$.

From the analytical formulas for the solution of the Riemann problem given for a convex conservation law ($f''(u) > 0$), (see ([15])), we can get a simple expression for the Godunov flux in this case

$$g_{GOD}(u_j^n, u_{j+1}^n) := \begin{cases} \min_{u_j^n \leq u \leq u_{j+1}^n} f(u), & \text{si } u_j^n < u_{j+1}^n; \\ \max_{u_j^n \geq u \geq u_{j+1}^n} f(u), & \text{si } u_j^n > u_{j+1}^n. \end{cases} \quad (2.36)$$

Using this last formula it is easy to see that the Godunov scheme is also upwind.

The main properties of monotone schemes are:

1. They converge to the weak solution satisfying the entropy condition.
2. They avoid spurious oscillations and Gibbs' phenomenon.
3. They are first order accurate in the smooth regions of the solution.

Since the principal term of the truncation error for the monotone schemes is given in terms of the second derivative in space, the diffusive effect of this term is significant and the resolution of discontinuities is poor due to the smearing.

The viscosity of a numerical scheme is the coefficient of the second derivative in space. If a numerical scheme in conservation form is defined from a numerical flux function of two variables, $g(u, v)$, (see Harten, [11]), then we define the viscosity as the function $Q(u, v)$ that satisfy

$$g(u, v) = \frac{1}{2} [f(u) + f(v)] - \frac{1}{2} Q(u, v) [v - u]. \quad (2.37)$$

For the Lax-Friedrichs scheme, $Q_{LF} = \frac{1}{\lambda}$ where $\lambda = \frac{\Delta t}{h}$, and for the Engquist-Osher scheme is

$$Q_{EO}(u, v) = \frac{1}{v - u} \int_u^v |f'(s)| ds, \quad (2.38)$$

for $v \neq u$

It can be shown that the viscosity of the Godunov's scheme is the minimum one among the ones corresponding to monotone and conservative schemes, ([27]). The viscosity of the Lax-Friedrichs scheme is larger than the one of Engquist-Osher scheme.

The main feature of monotone shock capturing schemes (in conservation form) is that they avoid spurious oscillations near discontinuities and propagate them at the correct speed. Their main disadvantage is the smearing (diffusion) generated at discontinuities due to the numerical viscosity.

In order to reduce the numerical viscosity the need of high order accurate shock capturing schemes becomes unavoidable. Second order accurate methods such as the Lax-Wendroff (see next Chapter) give much better accuracy on smooth regions of the solution than the monotone shock capturing schemes (first order), but they usually fail near discontinuities where spurious oscillations are generated. The spectral methods were designed to get higher order of accuracy, ([9]), but when used for the approximation of the solution with moving jump discontinuities they usually suffer the so-called Gibbs' phenomena, which consists in low-frequency spurious waves that contaminate the solution along the evolution.

In summary, the basic pathologies associated with numerical approximation of the solution (with jumps) of hyperbolic conservation laws are

1. Numerical diffusion
2. Spurious oscillations

Both phenomena are undesirable and in certain sense are opposite one to the other since numerical diffusion dump oscillations (spurious or not).

The main goal of this research is to design high order accurate shock capturing schemes that give high accuracy on smooth regions of the solution with a reduced numerical viscosity at discontinuities avoiding spurious oscillations.

There are extensive monographs on “Numerical schemes for conservation laws” like [14] and [19] where many other theoretical and numerical issues are treated, different from the one addressed in this research work.

CHAPTER 3

An extended class of limiters

3.1 Introduction

The first attempt to get high order accuracy was done by Lax and Wendroff in 1960 ([17]). The Lax-Wendroff scheme is a shock capturing scheme in conservation form as in (2.22) such that

$$g_{j+\frac{1}{2}}^n = g_{LW}(u_j^n, u_{j+1}^n)$$

where the numerical flux, defined by

$$g_{LW}(u, v) = \frac{1}{2} \left[f(u) + f(v) \right] - \frac{\Delta t}{2h} f\left(\frac{u+v}{2}\right) [f(v) - f(u)], \quad (3.1)$$

is consistent with the flux of the equation. This scheme is in conservation form but is not monotone. The Lax-Wendroff scheme is second order accurate in space and time but generates spurious oscillations near discontinuities.

We restrict our discussion to the linear advection model problem

$$u_t + cu_x = 0 \quad (3.2)$$

The Lax-Wendroff scheme for this problem can be deduced from the Taylor

expansion of the solution to (8.6)

$$u(x, t_{n+1}) = u(x, t_n) + \Delta t u_t(x, t_n) + \frac{1}{2} (\Delta t)^2 u_{tt}(x, t_n) + \dots \quad (3.3)$$

From (8.6) we have that $u_t = -cu_x$ and differentiating we obtain

$$u_{tt} = -cu_{xt} = c^2 u_{xx} \quad (3.4)$$

using $u_{xt} = u_{tx}$.

We plug (8.8) into the Taylor expansion and we obtain

$$u(x, t_{n+1}) = u(x, t_n) - \Delta t c u_x(x, t_n) + \frac{1}{2} (\Delta t)^2 c^2 u_{xx}(x, t_n) + \dots \quad (3.5)$$

If we truncate the last expansion keeping the three first terms and replacing spatial derivatives by central finite difference approximations, we get the Lax-Wendroff scheme for the linear advection

$$u_j^{n+1} = u_j^n - \frac{\Delta t}{2h} c (u_{j+1}^n - u_{j-1}^n) + \frac{1}{2} (\Delta t)^2 c^2 \frac{u_{j+1}^n - 2u_j^n + u_{j-1}^n}{h^2} \quad (3.6)$$

In this case the flux function becomes

$$g_{LW}(u, v) = \frac{1}{2} c(u + v) - \frac{1}{2} \Delta t h c^2 (v - u) \quad (3.7)$$

Thus, the analytical viscosity of the Lax-Wendroff scheme is $\frac{1}{2} (\Delta t)^2 c^2$ for the linear advection equation.

Van Leer in [40] designed a second order accurate shock capturing scheme without spurious oscillations near discontinuities by means of a function that limits the slopes.

The simplest way to measure how oscillatory is either a function or a numerical approximation, is looking at its total variation. Harten in [11] proposed to compute the total variation of u^n as

$$TV(u^n) := \sum_j |u_{j+1}^n - u_j^n| \quad (3.8)$$

The linear advection propagates the signal u at speed c without changing the shape and, therefore, the total variation (TV) of the solution must be constant in time. A numerical approximation to this equation might not preserve the TV and, if the approximation is oscillatory, the TV of the solution may increase when evolves in time.

Harten, in [11], introduced the following important concept:

Definition 2 *A numerical scheme is Total Variation Diminishing (TVD) if*

$$TV(u^{n+1}) \leq TV(u^n) \quad (3.9)$$

for all n .

Thus, TVD schemes are not oscillatory.

Harten proposed a simple criteria for a numerical scheme to satisfy the TVD property ([11]):

Theorem 2 (Harten) *If a numerical scheme is of the form*

$$u_j^{n+1} = u_j^n - C_{j-1}^n (u_j^n - u_{j-1}^n) + D_j^n (u_{j+1}^n - u_j^n) \quad (3.10)$$

where the coefficients C_{j-1}^n , D_j^n are arbitrary values (which may depend on u^n in a nonlinear way), then

$$TV(u^{n+1}) \leq TV(u^n) \quad (3.11)$$

provided the following conditions

$$C_{j-1}^n \geq 0, \quad \forall j \quad (3.12)$$

$$D_j^n \geq 0, \quad \forall j \quad (3.13)$$

$$C_j^n + D_j^n \leq 1, \quad \forall j \quad (3.14)$$

are satisfied.

It is easy to see that a first order monotone shock capturing scheme is TVD but the converse is not true. This fact opened the possibility to design second order accurate TVD methods. Osher and Chakravarty designed in [27] TVD schemes of any order of accuracy.

We may modify the Lax-Wendroff scheme to preserve second order accuracy and to satisfy the TVD property.

To simplify we set $c > 0$ in (8.6) and $\lambda = \frac{\Delta t}{h}$.

We write the Lax-Wendroff flux as a correction of Godunov (upwind) flux

$$g_{LW}(u, v) = cu + \frac{1}{2}c(1 - \lambda c)(v - u) \quad (3.15)$$

where

$$g_{GOD}(u, v) = cu, \quad (3.16)$$

in this case.

To define a flux-limiter scheme we replace the Lax-Wendroff numerical flux (8.5) by

$$g_{LW}^\phi(u, v) = cu + \frac{1}{2}c(1 - \lambda c)(v - u)\phi \quad (3.17)$$

being ϕ a function of u, v and additional neighboring values.

There are different ways we might limit the size of the flux. Here we focus on flux-limiter methods based on Lax-Wendroff scheme of the following specific form

$$g_{LW}^\phi(u_j, u_{j+1}) = cu_j + \frac{1}{2}c(1 - \lambda c)(u_{j+1} - u_j)\phi(\theta_j) \quad (3.18)$$

where

$$\theta_j = \frac{u_j - u_{j-1}}{u_{j+1} - u_j}$$

is the ratio of neighboring gradients and ϕ is a given real function of θ_j .

If θ_j is close to 1 then the data is smooth near u_j , but if θ_j is far from 1 then there is some sort of singularity around u_j . Let us observe that near extreme points, θ_j might be arbitrarily large and/or negative, then the size of θ_j is not a good measure of smoothness. This is the reason why TVD methods based on this approach cannot maintain second order accuracy at local extrema.

The following conditions on ϕ are sufficient to preserve second order accuracy away from local extrema.

1. $\phi(\theta) = 0$ if $\theta \leq 0$.
2. $\phi(1) = 1$ and ϕ is Lipschitz continuous at $\theta = 1$.

3. ϕ is a bounded function.

To know what conditions are required for a flux limiter scheme based on the Lax-Wendroff flux to give a TVD method, we may use Harten's theorem. If a function ϕ satisfies the above conditions and

$$0 \leq \frac{\phi(\theta)}{\theta} \leq 2, \quad \text{and} \quad 0 \leq \phi(\theta) \leq 2 \quad (3.19)$$

for all θ under the CFL restriction $|\lambda c| \leq 1$, then the flux limiter scheme is TVD.

For example, the minmod limiter introduced by Van Leer,

$$\text{minmod}(x, y) = \frac{(\text{sign}(x) + \text{sign}(y))}{2} \min(|x|, |y|) \quad (3.20)$$

satisfies the above conditions by defining

$$\phi(\theta) = \text{minmod}(1, \theta) \quad (3.21)$$

since $0 \leq \frac{\phi(\theta)}{\theta} \leq 1$ and $0 \leq \phi(\theta) \leq 1$, and therefore this limiter makes the flux limiter method a TVD scheme.

3.2 Power limiters

The ENO, minmod (defined in the previous section), and harmonic limiters were introduced to control the behavior of reconstructions around discontinuities in order to avoid the Gibbs' phenomena and over/under-shoots. We want to get high order accurate reconstruction methods without spurious oscillations near discontinuities.

The limiters are usually based on a mean of two nonnegative numbers. Indeed,

$$\text{minmod}(x, y) = \frac{(\text{sign}(x) + \text{sign}(y))}{2} \min(|x|, |y|) \quad (3.22)$$

$$\text{mineno}(x, y) = \text{minsign}(x, y) \min(|x|, |y|) \quad (3.23)$$

$$\text{harmod}(x, y) = \frac{(\text{sign}(x) + \text{sign}(y))}{2} \frac{2|x||y|}{|x| + |y|} \quad (3.24)$$

$$\text{hareno}(x, y) = \text{minsign}(x, y) \frac{2|x||y|}{|x| + |y|} \quad (3.25)$$

where $\text{sign}(x)$ is the sign function, and

$$\text{minsign}(x, y) = \begin{cases} \text{sign}(x); & |x| \leq |y| \\ \text{sign}(y); & \text{otherwise} \end{cases}$$

These limiters are based on the minimum and harmonic mean respectively between two nonnegative numbers.

We propose a wide class of averages, bounded above by the arithmetic mean, containing the harmonic mean and the minimum as particular cases. Indeed, if $x > 0$ and $y > 0$, then, for a natural number p , we define the power- p mean, (as we did in ([33])), as:

$$\text{power}_p(x, y) = \frac{(x + y)}{2} \left(1 - \left| \frac{x - y}{x + y} \right|^p \right) \quad (3.26)$$

The function $\text{power}_p(x, y)$ is homogeneous of degree one as a function of two variables. It is easy to see that

$$\text{power}_p(x, y) = \min(x, y) \left[1 + \left| \frac{y-x}{y+x} \right| + \cdots + \left| \frac{y-x}{y+x} \right|^{p-1} \right] \quad (3.27)$$

In particular, if $0 < x < y$ then

$$\text{power}_p(x, y) = x \left[1 + \left(\frac{y-x}{y+x} \right) + \cdots + \left(\frac{y-x}{y+x} \right)^{p-1} \right] \quad (3.28)$$

This is a truncated geometric series with ratio $r = \frac{y-x}{y+x} > 0$ and $r < 1$. The infinite series converges to $\frac{x+y}{2}$. Then, the following inequalities are satisfied for any $x > 0$ and $y > 0$:

$$\min(x, y) \leq \text{power}_p(x, y) \leq \text{power}_q(x, y) \leq \frac{x+y}{2}$$

for $0 < p < q$.

Moreover, for any $x > 0$ and $y > 0$ we have

$$\text{power}_1(x, y) = \min(x, y) \quad (3.29)$$

$$\text{power}_2(x, y) = \frac{2xy}{x+y} \quad (3.30)$$

The above identities are very useful to compute the discrepancy between the arithmetic mean and the Power _{p} means, in order to get simple expressions of the truncation errors, as we will see in the next Chapter.

The following proposition describes a necessary condition for an average to be useful to design limiters in the reconstruction procedures that are piecewise smooth and their total variation in cells next to discontinuities is bounded. This property is not satisfied for the arithmetic mean, nor the geometric mean.

Proposition 1 If $x(h) > 0$ and $y(h) > 0$ are functions of the real parameter $h > 0$, such that $x(h) = O(1)$ and $y(h) = O(\frac{1}{h})$, then $\text{power}_p(x(h), y(h)) = O(1)$.

This assertion follows easily from the identity (8.25).

Next, we discuss the above defined means in order to know their scope when used in the design of limiters.

Now we can define the corresponding limiters:

$$\text{powermod}_p(x, y) = \frac{(\text{sign}(x) + \text{sign}(y))}{2} \text{power}_p(|x|, |y|) \quad (3.31)$$

$$\text{powereno}_p(x, y) = \text{minsign}(x, y) \text{power}_p(|x|, |y|) \quad (3.32)$$

The following identities show that minmod, ENO and harmonic limiters are particular cases of the Power_p limiters:

$$\text{powermod}_1(x, y) = \text{minmod}(x, y) \quad (3.33)$$

$$\text{powereno}_1(x, y) = \text{mineno}(x, y) \quad (3.34)$$

$$\text{powermod}_2(x, y) = \text{harmod}(x, y) \quad (3.35)$$

$$\text{powereno}_2(x, y) = \text{hareno}(x, y) \quad (3.36)$$

If we define a flux limiter function from a limiter as

$$\phi^p(\theta) = \text{powermod}_p(1, \theta), \quad (3.37)$$

we have that ϕ^p satisfies $\phi^p(\theta) = 0$ if $\theta \leq 0$.

The following lemma follows easily from the definition of the powermod_p limiters:

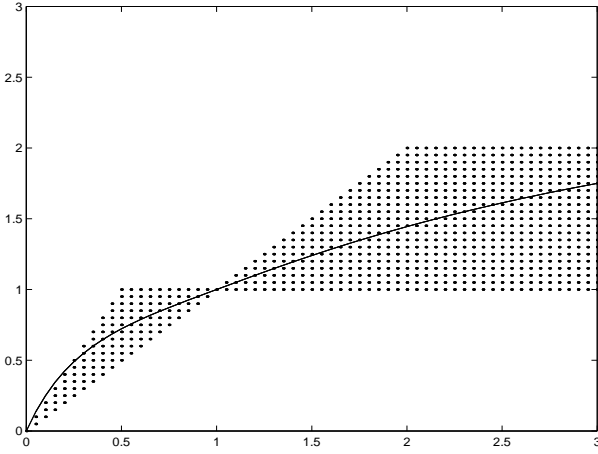


Figure 3.1: Second order TVD region and $\phi^3(\theta)$

Proposition 2

$$0 \leq \frac{\phi^p(\theta)}{\theta} \leq p, \text{ and } 0 \leq \phi^p(\theta) \leq p, \text{ for all } \theta.$$

Thus, for $p = 1, 2$ the ϕ^p function defines a TVD scheme under the CFL restriction $|\lambda c| \leq 1$. On the other hand, for $p > 2$, it is not true that the flux limiter Lax-Wendroff scheme described above is TVD, under the same CFL restriction, (see Figure 3.1). In fact, for $p = 3$, we have the restriction $\frac{1}{3} < |\lambda c| < \frac{2}{3}$, which is not useful. Therefore, for $p > 2$ the powermod _{p} and powereno _{p} limiters should not be used for the schemes described above. This behavior can be observed in Figure 3.1, where we represent $\phi^3(\theta)$ over the second order TVD region, (see [19] for details on TVD regions).

However, for methods of order of accuracy larger than two, (and then, excluding Lax-Wendroff), first and second order differences need to be limited like in ENO methods. When limiting second order differences, small scales may be destroyed by using a very strong limiter like the one used for ENO methods. The

well known “smearing effect” of ENO methods of order larger than two is, in part, due to the above reason.

In this research work we focus our study on the power limiters for $p = 3$, based on the power₃ mean. When power₃ limiter is used as a limiter of first or second order differences, the resulting method behaves essentially non-oscillatory near discontinuities, (see Proposition 3 next section), and it allows simple expressions of the local truncation errors when, in particular, is used as a limiter of second order differences.

Formally, power₃ mean can be written in the more convenient form:

$$\text{power}_3(x, y) = \min(x, y) \frac{x^2 + y^2 + 2(\max(x, y))^2}{(x + y)^2} \quad (3.38)$$

CHAPTER 4

Piecewise Smooth Reconstructing Functions

4.1 Introduction

Our general goal consists in obtaining high order accurate numerical approximations to piecewise smooth real functions of a real variable with a finite number of jump discontinuities to approximate the solution of hyperbolic systems of conservation laws. A simple and useful procedure is to define the scale of computation by means of a partition of the domain interval of the function and use an elementary basic one, (easy to compute, e.g. polynomial, rational,...), for each of the subintervals, such that it locally approximates the original function. The local degree of smoothness of the original function determines the finest scale for which we need to reconstruct the function and the choice of the degree of accuracy. The choice of the size of the partition and the degree of accuracy for a specific problem is a hard task.

Our discussion here will focus on a fixed uniform grid and a fixed degree of local accuracy, trying to minimize the spurious information generated when dealing simultaneously with coarse and fine scales. In order to reach this goal several authors have been developed various procedures to avoid the transfer of

spurious information from fine to coarse scales and viceversa. Gibbs phenomena or Runge oscillatory pattern are usually found when approximating a piecewise smooth function and these are well known examples of this kind of unfortunate behavior. The approximation problem mentioned above becomes more difficult when the function to be approximated evolves with time ruled by a time dependent PDE. In this case, the relation between fine and coarse scales may change in a nonlinear way. Therefore, the approximating procedure should be adaptive to take into account all those circumstances. This problem has been addressed in computational fluid dynamics in order to get accurate numerical simulations of compressible flows, (see [1, 2, 11, 12, 13, 20, 21, 26, 30, 31, 33]).

A first order approximation to a piecewise smooth function in a fixed grid can be defined as a piecewise constant function, with jump discontinuities located at the cell interfaces. Van Leer considered second order approximations defined as piecewise linear functions, introducing for the first time the minmod limiter function applied on neighboring slopes to avoid the Gibbs phenomena near discontinuities when computing approximate solutions to hyperbolic conservation laws [19]. Total Variation Diminishing (TVD) schemes were introduced in [11] to get high order accurate non oscillatory approximations of the solution of hyperbolic conservation laws, but the main drawback of these schemes was the degeneration to first order of accuracy at local extrema, [27]. Essentially non oscillatory, (ENO), methods were introduced to get high order accurate reconstruction procedures of order larger than two, avoiding Gibbs phenomena and spurious oscillations up to local truncation errors, ([12]). ENO procedures uses the smoothest polynomial interpolation by means of choosing the differences of

smallest size following a tree-like algorithm. The selection procedure of the ENO methods is a limiter function acting on the successive differences of the data. One of the important issues of the high order accurate reconstruction procedures is the size of the stencil, i.e., the number of data points needed to perform the approximation. If the stencil is small the behavior of the procedure is robust when used in evolution problems where discontinuities are either moving or interacting, but the degree of accuracy is limited. By using a limiter function we may design reconstruction procedures with an optimal size of the stencil and good resolution of discontinuities.

In order to settle our notation and computational framework, we consider numerical approximations to the scalar initial value problem

$$u_t + f(u)_x = 0, \quad (4.1)$$

$$u(x, t) = u_0(x), \quad (4.2)$$

where u_0 is a periodic or compactly supported piecewise smooth function.

We will consider the computational grid introduced in Chapter 2.

We want to find numerical approximations of a piecewise smooth function $g(x)$ from its cell averages, given for the cells of the defined uniform grid of stepsize $h > 0$, $x_j = jh$,

$$v_j = \frac{1}{h} \int_{x_{j-\frac{1}{2}}}^{x_{j+\frac{1}{2}}} g(x, t_n) dx \quad (4.3)$$

The specific uniform grid considered is the scale of computation chosen for our approximation. The idea is to capture subscales of the original chosen scale

by means of a piecewise smooth function, R , such that the restriction to each computational cell $[x_{j-\frac{1}{2}}, x_{j+\frac{1}{2}}]$, is a suitable elementary function, R_j , such that

$$v_j = \frac{1}{h} \int_{x_{j-\frac{1}{2}}}^{x_{j+\frac{1}{2}}} R_j(x, t_n) dx \quad (4.4)$$

and it approximates g up to a degree of accuracy.

We are going to analyze the behavior of R in terms of h , when h tends to zero. This behavior might be undesirable around jump discontinuities of g since the function R may develop either Gibbs phenomena or Runge oscillatory pattern. On the other side, the order of accuracy may degenerate through smooth regions of g due to the presence of the above singularities. The mentioned computational problems are always present when using the described framework to approximate the solution of hyperbolic conservation laws, since those evolution equations may develop discontinuities (shocks) in finite time, (see [12, 21, 36]).

We focus on third order accurate piecewise smooth functions, R , such that each R_j is determined from condition (8.37) and two more conditions, usually obtained from differences of v_j . We denote by

$$d_{j+\frac{1}{2}} = v_{j+1} - v_j \quad (4.5)$$

If we know the first derivatives of g at the cell interfaces, i.e. $g'(x_{j+\frac{1}{2}})$, we can use the following two interpolating conditions to ensure third order accuracy in

smooth regions

$$R'_j(x_j - \frac{h}{2}) = g'(x_{j-\frac{1}{2}}) \quad (4.6)$$

$$R'_j(x_j + \frac{h}{2}) = g'(x_{j+\frac{1}{2}}) \quad (4.7)$$

We use the first order divided differences $\frac{d_{j-\frac{1}{2}}}{h}$ and $\frac{d_{j+\frac{1}{2}}}{h}$ instead of $g'(x_{j-\frac{1}{2}})$ and $g'(x_{j+\frac{1}{2}})$ respectively if the last values are not available. If we consider a local parabola of the form

$$p_j(x) = a_j + b_j(x - x_j) + \frac{c_j}{2}(x - x_j)^2 \quad (4.8)$$

there is a unique parabola such that conditions (8.37), (8.39) and (8.40) are satisfied, that is a_j , b_j and c_j are uniquely defined.

Following [21], if we consider hyperbolas of the form

$$r_j = e_j + \frac{\lambda_j}{(x - x_j) + f_j} \quad (4.9)$$

we can compute a unique hyperbola satisfying (8.37), (8.39) and (8.40), (λ_j , e_j and f_j are uniquely defined), assuming that $g'(x_{j-\frac{1}{2}}) \cdot g'(x_{j+\frac{1}{2}}) > 0$, since hyperbolas are monotone functions.

We want to study how oscillatory the approximation R of the function $g(x)$ is in terms of h . In order to get a coarse comparison between the parabolic and the hyperbolic reconstructions we may assume for the sake of simplicity the following notation. We consider the cell for $j = 0$, $[x_{-\frac{1}{2}}, x_{\frac{1}{2}}]$, and we use $d_l := \frac{d_{-\frac{1}{2}}}{h}$ and $d_r := \frac{d_{\frac{1}{2}}}{h}$.

If $d_l \cdot d_r > 0$, the total variation of the parabola p_0 (assuming p_0 is monotone) is

$$TV(p_0) = h \frac{|d_l| + |d_r|}{2} \quad (4.10)$$

and the total variation of the hyperbola r_0 is, (see [21]),

$$TV(r_0) = h \sqrt{|d_l| \cdot |d_r|} \quad (4.11)$$

From the arithmetic-geometric inequality we conclude that the parabolic reconstruction prescribes more total variation than the hyperbolic one. Let us remark that formulas (8.43) and (8.44) are the product of h times an average of two positive numbers. If g is smooth on a region containing our computational cell $[-\frac{h}{2}, \frac{h}{2}]$, then d_l and d_r are bounded and therefore, $TV(p_0) = O(h)$ and $TV(r_0) = O(h)$. Thus, p_0 and r_0 are smooth enough to be non-oscillatory and those quantities tend to zero with h .

On the other hand, if g has a jump discontinuity at $x_0 = 0$, either d_l or d_r is $O(\frac{1}{h})$, and

$$TV(p_0) = O(1) \quad (4.12)$$

and

$$TV(r_0) = O\left(\sqrt{h}\right) \quad (4.13)$$

Thus, in the presence of discontinuities, hyperbolas are much less oscillatory than parabolas.

One way to make less oscillatory a piecewise smooth approximation is by using slope limiters to preprocess first order derivatives in a way that the order

of accuracy does not degenerate.

We can assert that hyperbolas have a natural mechanism to limit the gradient by means of an average. In fact, the first derivative of r_0 at $x = 0$ is, from [21],

$$r'_0(x_0) = \text{sign}(d_l) \left(\frac{2\sqrt{|d_l|}\sqrt{|d_r|}}{\sqrt{|d_l|} + \sqrt{|d_r|}} \right)^2 \quad (4.14)$$

which is much smaller in size than the one of the parabola,

$$p'_0(x_0) = \text{sign}(d_l) \frac{|d_l| + |d_r|}{2} \quad (4.15)$$

assuming $d_l \cdot d_r > 0$, (see Hardy, Littlewood and Polya, [10]).

Thus, our main goal for piecewise smooth reconstructions is to control the total variation growth. The local total variation bounded condition was introduced in [21] for this purpose.

Definition 3 *A piecewise smooth reconstruction R is local total variation bounded (LTVB) if there is a constant $M > 0$, independent of h , such that, for all j ,*

$$TV(R_j) \leq Mh \quad (4.16)$$

We are going to construct and analyze piecewise smooth reconstructions using either hyperbolas or parabolas satisfying the LTVB condition.

4.2 Hyperbolic reconstructions

Marquina proposed in [21] piecewise hyperbolic reconstructions of type (8.42).

The local non oscillatory hyperbolic reconstructions were proposed in [21] to get third order spatial accuracy using a three point stencil in order to improve the resolution of rarefaction corners in fluid flow calculations. The harmonic mean of the lateral derivatives was used in [21] to achieve the non oscillatory property of the reconstructing function, avoiding the enlargement of the stencil.

Piecewise Hyperbolic Methods, (PHM), have been used in a variety of problems. The piecewise hyperbolic reconstruction is a third-order accurate reconstruction that works robustly with shock capturing schemes ([4], [7], [21], [22], [39]), relaxation schemes ([1], [30], [31]), and moving mesh methods ([18]). This good behavior is mainly due to:

1. Reduced stencil
2. Hyperbolas are less oscillatory than parabolas (as we have seen in the introduction of this Chapter).
3. The use of a limiter based on the harmonic mean.

4.2.1 Power Piecewise Hyperbolic Method

Applying Marquina, ([21]), we can write any hyperbola $r_0(x)$ satisfying the conservation property, (8.37), and $r'_0(x_0) = d_0$, in terms of any d_0 and an adimensional parameter α , in the form,

$$r_0(x) = v_0 + d_0 h \frac{1}{\alpha^2} \left[\log\left(\frac{2-\alpha}{2+\alpha}\right) - \frac{\alpha h}{\alpha(x-x_0) - h} \right] \quad (4.17)$$

where

$$\alpha = \frac{1}{2} \frac{d_r - d_l}{d_r + d_l} \quad (4.18)$$

to guarantee the hyperbola interpolates the lateral derivatives.

From the above expressions, it follows that α is constrained to the interval $[-2, 2]$.

For a chosen d_0 , there are two possible values for α depending on which lateral derivative is interpolated.

From ([21]),

- (a) If $d_0 \cdot d_l > 0$ then $\alpha = 2(\sqrt{\frac{d_0}{d_l}} - 1)$ if and only if $d_l = r'(x_0 - \frac{h}{2})$.
- (b) If $d_0 \cdot d_r > 0$ then $\alpha = 2(1 - \sqrt{\frac{d_0}{d_r}})$ if and only if $d_r = r'(x_0 + \frac{h}{2})$.

To ensure that a hyperbolic reconstruction is LTVB, it is sufficient to restrict the range of values of α to an interval $[-M, M]$ such that $0 < M < 2$.

Marquina in [21] proposed an appropriate choice of d_0 to accomplish the above property. Indeed, the local hyperbolic harmonic reconstruction, LHHR, prescribes, in each computational cell, a hyperbola r_j that satisfies (8.37), interpolates the lateral derivative with the smallest absolute value, and assigns, as the central derivative (d_0), the harmonic mean of both lateral derivatives instead of (8.42). In this case, the range of values for α , independent of h , is confined to

$$-2(\sqrt{2} - 1) < \alpha < 2(\sqrt{2} - 1) \quad (4.19)$$

This inequality guarantees the LTVB condition for LHHR ([21]).

The main drawback of the LHHR is the loss of accuracy at local extrema and, as consequence, the loss of total variation at those points.

One way to increase locally the total variation of the reconstruction is to consider another choice of d_0 allowing a wider range of α values than the one prescribed by the d_0 of LHHR.

To improve the resulting effect of applying the harmonic mean on lateral derivatives in LHHR, we propose to relax this limiting effect by using power₃ limiter instead and, likewise, ensuring the existence of a positive number β satisfying $-2\beta \leq \alpha \leq 2\beta$ and $\sqrt{2} - 1 \leq \beta < 1$.

To this end we have to compare the power₃ mean with the harmonic one and the natural mean for the hyperbola (8.42).

We use the following notation to settle the next propositions. If $x > 0$ and $y > 0$ then $\mathcal{A}(x, y) = \frac{x+y}{2}$, $\mathcal{G}(x, y) = \sqrt{xy}$, $\mathcal{H}(x, y) = \frac{2xy}{x+y}$ and $\mathcal{H}_4 = \left(\frac{2\sqrt{x}\sqrt{y}}{\sqrt{x}+\sqrt{y}}\right)^2$. Let us remark that \mathcal{H}_4 appears in the expression (8.42) as the natural derivative of the hyperbola at the center.

In order to be more concise we will skip the dependence on x and y . We denote $\mathcal{P}_j = \text{power}_j(x, y)$.

Let us compare these averages.

Proposition 3 *Let $x \geq 0$ and $y \geq 0$ no simultaneously zero. Let $r = \frac{\mathcal{G}}{\mathcal{A}}$ and $R = \left|\frac{x-y}{x+y}\right|$. Then,*

$$1. R^2 + r^2 = 1$$

$$2. \mathcal{H} = \mathcal{A}(1 - R^2)$$

$$3. \quad \mathcal{H}_4 = \mathcal{H} \left(1 + R^2 \frac{1}{(1+r)^2} \right)$$

$$4. \quad \mathcal{P}_3 = \mathcal{H} \left(1 + R^2 \frac{1}{1+R} \right)$$

$$5. \quad \mathcal{P}_4 = \mathcal{H}(1 + R^2)$$

$$6. \quad \mathcal{H} \leq \mathcal{P}_3 \leq \mathcal{P}_4$$

$$7. \quad \mathcal{H} \leq \mathcal{H}_4 \leq \mathcal{P}_4$$

Proof. Straightforward. \square

Proposition 4 *The averages \mathcal{P}_3 and \mathcal{H}_4 are not comparable. There exists a unique $r_1 \approx 0.38\dots$, such that $\mathcal{P}_3 = \mathcal{H}_4$ and*

$$1. \quad \text{If } 0 < r \leq r_1 \text{ then } \mathcal{P}_3 \leq \mathcal{H}_4$$

$$2. \quad \text{If } r_1 \leq r < 1 \text{ then } \mathcal{H}_4 \leq \mathcal{P}_3$$

Proof. It follows easily from Proposition 3. \square

From the above propositions we conclude that \mathcal{P}_3 prescribes more total variation in cell than \mathcal{H} when is applied to lateral derivatives. In the same way, \mathcal{P}_3 assigns more total variation than \mathcal{H}_4 in smooth regions ($r_1 \leq r$), in particular at local extrema, and prescribes less total variation at discontinuities ($r \leq r_1$). Next we show that there exists a hyperbolic reconstruction based on \mathcal{P}_3 that satisfies the LTVB condition.

In the LHHR, to define the hyperbolic reconstruction, it is necessary to know the value of the ratio between the harmonic mean of the lateral derivatives and the lateral derivative with the smallest absolute value.

We define the ratio for the \mathcal{P}_3 case as:

$$\mathcal{R}_3(x, y) = \frac{x^2 + y^2 + 2\left(\max(x, y)\right)^2}{(x + y)^2} \quad (4.20)$$

defined for $x \geq 0$ and $y \geq 0$, not simultaneously zero.

Following [33], we define $\text{powereno}(x, y) = \text{powereno}_3(x, y)$. We use this limiter for the design of the local hyperbolic power reconstruction.

The following algorithm defines a hyperbola in terms of d_0 and α according to (8.50).

LOCAL HYPERBOLIC POWER RECONSTRUCTION METHOD (LHPR)

Let define $tol = h^2$,

if ($|d_l| \leq tol$) and ($|d_r| \leq tol$) **then**

$d_0 = 0$ and $\alpha = 0$

else

$$d_0 = \text{powereno}(d_l, d_r) = \text{minsign}(dl, dr) \min(|dl|, |dr|) \frac{dl^2 + dr^2 + 2\left(\max(|dl|, |dr|)\right)^2}{(|dl| + |dr|)^2}$$

if $|d_l| \leq |d_r|$ **then**

$$\text{ratio} = \frac{d_l^2 + 3d_r^2}{(|d_l| + |d_r|)^2} \quad (= \mathcal{R}_3)$$

$$\alpha = 2(\sqrt{\text{ratio}} - 1)$$

else

$$\text{ratio} = \frac{3d_l^2 + d_r^2}{(|d_l| + |d_r|)^2} \quad (= \mathcal{R}_3)$$

$$\alpha = 2(1 - \sqrt{\text{ratio}})$$

end

end

The following lemmas show that this algorithm gives a well defined hyperbola.

Lemma 1 $\mathcal{R}_3 \leq 3$ for $x \geq 0$ and $y \geq 0$ not simultaneously zero.

Proof. Let us define $\lambda := \frac{\min(x,y)}{\max(x,y)}$. Then, $0 \leq \lambda \leq 1$ and $\mathcal{R}_3(\lambda) = \frac{3+\lambda^2}{(1+\lambda)^2}$.

Since \mathcal{R}_3 is a strictly decreasing function of λ in $[0, 1]$ and $\mathcal{R}_3(0) = 3$, we have that $\mathcal{R}_3 \leq 3$. \square

Lemma 2 The range of values of the adimensional parameter α for the LHP*R* method is

$$-2(\sqrt{3} - 1) < \alpha < 2(\sqrt{3} - 1) \quad (4.21)$$

Proof. It follows easily from Lemma 4. \square

Thus, we get the LTVB property for LHP*R*.

Theorem 3 The LHP*R* method is LTVB.

Proof. We can find a constant $M > 0$ such that for all j except for a finite number of isolated j 's for which $d_{j+\frac{1}{2}} = O(\frac{1}{h})$, $|d_{j+\frac{1}{2}}| \leq M$.

If $|d_{j-\frac{1}{2}}| \leq |d_{j+\frac{1}{2}}|$, $d_{l_j} = \frac{d_{j-\frac{1}{2}}}{h}$ and

$$d_{r_j} = \frac{d_{j-\frac{1}{2}}}{h} \left(\frac{2 + \alpha}{2 - \alpha} \right)^2 \quad (4.22)$$

From Lemma 5, we have that

$$TV(r_j) \leq (3 + 2\sqrt{3}) \cdot M \cdot h$$

□

4.3 Parabolic reconstructions

High order accurate numerical approximations to piecewise smooth functions with jump discontinuities are such that they achieve high accuracy on smooth regions and sharpen profiles of discontinuities, without spurious oscillations. Essentially non oscillatory, (ENO), polynomial reconstruction procedures were designed to accomplish this purpose, ([12]). ENO methods are high-order accurate on smooth regions and appear to be very robust on shocks. However, several drawbacks became relevant after some experimentation with ENO methods took place, from which we mention:

1. Loss of accuracy on smooth regions with specific input data, ([29]).
2. Smearing of certain discontinuities ([13]).
3. Smoothing up of corners, (discontinuities of the first derivative), ([21]).
4. Too wide stencil to get high order accuracy, ([13]).

In order to overcome those difficulties, (see [29]), several remedies were proposed. Shu proposed in [35] a more centered ENO selection to reduce the loss of accuracy. Weighted ENO methods by Liu, Osher and Chan ([20]), were designed to get

optimal accuracy for a specific stencil, degenerating to a classical ENO method at discontinuities.

4.3.1 PowerENO method

All the polynomial reconstruction methods analyzed in this paper have the same stencil as the classical ENO3 method and based on parabolas of the form:

$$p_j(x) = a_j + (x - x_j) \left[b_j + \frac{c_j}{2}(x - x_j) \right] \quad (4.23)$$

defined on I_j where a_j , b_j and c_j are determined from the grid data.

We use (8.38) and the following additional notations:

$$d_j = \frac{d_{j+\frac{1}{2}} + d_{j-\frac{1}{2}}}{2} \quad (4.24)$$

$$D_j = d_{j+\frac{1}{2}} - d_{j-\frac{1}{2}} \quad (4.25)$$

The classical ENO3 method is based on a selection procedure that chooses one parabola from the following three candidates, ([12, 36]):

$$p_{j-1}(x) = v_j - \frac{D_{j-1}}{24} + \frac{x - x_j}{h} \left[d_{j-\frac{1}{2}} + \frac{D_{j-1}}{2} + \frac{D_{j-1}}{2} \left(\frac{x - x_j}{h} \right) \right] \quad (4.26)$$

$$p_j(x) = v_j - \frac{D_j}{24} + \frac{x - x_j}{h} \left[d_j + \frac{D_j}{2} \left(\frac{x - x_j}{h} \right) \right] \quad (4.27)$$

$$p_{j+1}(x) = v_j - \frac{D_{j+1}}{24} + \frac{x - x_j}{h} \left[d_{j+\frac{1}{2}} - \frac{D_{j+1}}{2} + \frac{D_{j+1}}{2} \left(\frac{x - x_j}{h} \right) \right] \quad (4.28)$$

which correspond to the left, central and righthand side choice, respectively. The ENO3 selection procedure to get the ENO parabola for the computational cell $C_j = [x_{j-\frac{1}{2}}, x_{j+\frac{1}{2}}]$ reads as follows:

```

if  $|d_{j-\frac{1}{2}}| \leq |d_{j+\frac{1}{2}}|$  then
    if  $|D_{j-1}| \leq |D_j|$  then
         $p_{j-1}(x)$ 
    else
         $p_j(x)$ 
    end
else
    if  $|D_j| \leq |D_{j+1}|$  then
         $p_j(x)$ 
    else
         $p_{j+1}(x)$ 
    end
end

```

To explore new ways to design ENO methods such that we get better behavior near discontinuities, we make use of two new parabolas instead of the left and right choices used in ENO3. We construct these new parabolas using an intermediate value between two neighboring second order differences:

$$p_{j-\frac{1}{2}}^M(x) = v_j - \frac{M_{j-\frac{1}{2}}}{24} + \frac{x-x_j}{h} \left[d_{j-\frac{1}{2}} + \frac{M_{j-\frac{1}{2}}}{2} + \frac{M_{j-\frac{1}{2}}}{2} \left(\frac{x-x_j}{h} \right) \right] \quad (4.29)$$

$$p_{j+\frac{1}{2}}^M(x) = v_j - \frac{M_{j+\frac{1}{2}}}{24} + \frac{x-x_j}{h} \left[d_{j+\frac{1}{2}} - \frac{M_{j+\frac{1}{2}}}{2} + \frac{M_{j+\frac{1}{2}}}{2} \left(\frac{x-x_j}{h} \right) \right] \quad (4.30)$$

where $M_{j-\frac{1}{2}} := \text{mean}(D_{j-1}, D_j)$ and $M_{j+\frac{1}{2}} := \text{mean}(D_j, D_{j+1})$, where “mean” is an intermediate value that eventually may be a limiter, (see [23]).

Next, we introduce the third order accurate **Power ENO** method. We will use the powereno₃ or powermod₃ limiters, (the limiters based on the mean power₃, as introduced in Chapter 8.3), computed at two neighboring second order differences, at the place of the mean M , mentioned above. For the sake of simplicity we refer to those limiters as **powereno** and **powermod** avoiding the subindex.

We will use the following three parabolas:

$$p_{j-\frac{1}{2}}^P(x) = v_j - \frac{P_{j-\frac{1}{2}}}{24} + \frac{x-x_j}{h} \left[d_{j-\frac{1}{2}} + \frac{P_{j-\frac{1}{2}}}{2} + \frac{P_{j-\frac{1}{2}}}{2} \left(\frac{x-x_j}{h} \right) \right] \quad (4.31)$$

$$p_j(x) = v_j - \frac{D_j}{24} + \frac{x-x_j}{h} \left[d_j + \frac{D_j}{2} \left(\frac{x-x_j}{h} \right) \right] \quad (4.32)$$

$$p_{j+\frac{1}{2}}^P(x) = v_j - \frac{P_{j+\frac{1}{2}}}{24} + \frac{x-x_j}{h} \left[d_{j+\frac{1}{2}} - \frac{P_{j+\frac{1}{2}}}{2} + \frac{P_{j+\frac{1}{2}}}{2} \left(\frac{x-x_j}{h} \right) \right] \quad (4.33)$$

which correspond to the left, central and righthand side choice respectively, and $P_{j-\frac{1}{2}} = \text{powereno}(D_{j-1}, D_j)$ and $P_{j+\frac{1}{2}} = \text{powereno}(D_j, D_{j+1})$. Powermod limiter might be used instead, being less oscillatory.

Then, the Power ENO3 method is defined choosing one of the above parabolas following the selection procedure of the classical ENO3 method. If we use the powereno_1 limiter instead of powereno , we recover the ENO3 method.

In [21], it was shown that ENO3 method is local total variation bounded. Following analogous argument it is easy to show that:

Proposition 5 *The Power ENO3 method is local total variation bounded, i.e., $TV(r) = O(h)$, where r_j is the reconstruction for the cell C_j and h is the spatial step.*

4.3.2 Weighted PowerENO method

Liu et al. in [20] introduced the Weighted ENO schemes using a cell average framework. The spatial values are computed using a convex combination of the ENO3 cell averaged parabolas getting fourth order accuracy. Based on the pointwise ENO3 parabolas described in the previous section, Jiang and Shu developed in [13] the WENO5 method using a nonlinear convex combination of the above parabolas reaching fifth order accuracy, by means of a new measurement of the smoothness, written in terms of the so-called indicator of smoothness.

In order to show the prospective interest of our Power ENO method, we shall construct a new weighted ENO method as a convex combination of the three parabolas (8.62), (8.63) and (8.64) used for our Power ENO3 method. Then, in

order to compute the optimal linear weights for this method we need to know simple expressions of the truncation errors for the above mentioned parabolas. We can obtain simple expressions using the arithmetic mean, instead of our nonlinear limiter.

Proposition 6 *If we use the arithmetic mean A , i.e., $A(x, y) := \frac{x+y}{2}$, for the parabolas (8.60) and (8.61), then, we have the following truncation error expressions at the right interface, $x_{j+\frac{1}{2}}$:*

$$p_{j-\frac{1}{2}}^A(x_{j+\frac{1}{2}}) - u = -4 \left(\frac{h}{2}\right)^3 \frac{u'''}{6} + \frac{256}{5} \left(\frac{h}{2}\right)^4 \frac{u^{(iv)}}{24} + O(h^5) \quad (4.34)$$

$$p_{j+\frac{1}{2}}^A(x_{j+\frac{1}{2}}) - u = -\frac{64}{5} \left(\frac{h}{2}\right)^4 \frac{u^{(iv)}}{24} + O(h^6) \quad (4.35)$$

Proof. The Taylor expansion of $u(x)$ is

$$\begin{aligned} u(x) &= u(x_j) + u'(x_j)(x - x_j) + u''(x_j) \frac{(x - x_j)^2}{2} + u'''(x_j) \frac{(x - x_j)^3}{6} + \\ &\quad u^{(iv)}(x_j) \frac{(x - x_j)^4}{24} + O(h^5) \end{aligned}$$

then, by computing (8.36) we get the Taylor expansions of the cell averages:

$$v_j = u(x_j) + \frac{1}{6} \left(\frac{h}{2}\right)^2 u''(x_j) + \frac{1}{120} \left(\frac{h}{2}\right)^4 u^{(iv)}(x_j) + O(h^6) \quad (4.36)$$

We want to obtain the Taylor expansions, located at the right interface $x_{j+\frac{1}{2}}$, thus, for simplicity we denote by $u, u', u'', u''', u^{(iv)}, u^{(v)}$, the values of those functions evaluated at $x_{j+\frac{1}{2}}$.

$$u(x_j) = u - \frac{h}{2}u' + \left(\frac{h}{2}\right)^2 \frac{u''}{2} - \left(\frac{h}{2}\right)^3 \frac{u'''}{6} + \left(\frac{h}{2}\right)^4 \frac{u^{(iv)}}{24} + O(h^5)$$

$$\begin{aligned} u''(x_j) &= u'' - \frac{h}{2}u''' + \left(\frac{h}{2}\right)^2 \frac{u^{(iv)}}{2} + O(h^3) \\ u^{(iv)}(x_j) &= u^{(iv)} - \frac{h}{2}u^{(v)} + O(h^2) \end{aligned}$$

Therefore, the Taylor expansion of v_j at $x_{j+\frac{1}{2}}$ will be

$$v_j = u - \frac{h}{2}u' + \frac{4}{3}\left(\frac{h}{2}\right)^2 \frac{u''}{2} - 2\left(\frac{h}{2}\right)^3 \frac{u'''}{6} + \frac{16}{5}\left(\frac{h}{2}\right)^4 \frac{u^{(iv)}}{24} + O(h^5) \quad (4.37)$$

The corresponding expressions for $v_{j+1}, v_{j-1}, v_{j+2}$ and v_{j-2} , are obtained in a similar way and read as follows:

$$\begin{aligned} v_{j+1} &= u + \frac{h}{2}u' + \frac{4}{3}\left(\frac{h}{2}\right)^2 \frac{u''}{2} + 2\left(\frac{h}{2}\right)^3 \frac{u'''}{6} + \frac{16}{5}\left(\frac{h}{2}\right)^4 \frac{u^{(iv)}}{24} + O(h^5) \\ v_{j-1} &= u - 3\frac{h}{2}u' + \frac{28}{3}\left(\frac{h}{2}\right)^2 \frac{u''}{2} - 30\left(\frac{h}{2}\right)^3 \frac{u'''}{6} + \frac{496}{5}\left(\frac{h}{2}\right)^4 \frac{u^{(iv)}}{24} + O(h^5) \\ v_{j+2} &= u + 3\frac{h}{2}u' + \frac{28}{3}\left(\frac{h}{2}\right)^2 \frac{u''}{2} + 30\left(\frac{h}{2}\right)^3 \frac{u'''}{6} + \frac{496}{5}\left(\frac{h}{2}\right)^4 \frac{u^{(iv)}}{24} + O(h^5) \\ v_{j-2} &= u - 5\frac{h}{2}u' + \frac{76}{3}\left(\frac{h}{2}\right)^2 \frac{u''}{2} - 130\left(\frac{h}{2}\right)^3 \frac{u'''}{6} + \frac{3376}{5}\left(\frac{h}{2}\right)^4 \frac{u^{(iv)}}{24} + O(h^5) \end{aligned}$$

Thus, after a straightforward computation, we obtain

$$p_{j+\frac{1}{2}}^A(x_{j+\frac{1}{2}}) = u - \frac{64}{5}\left(\frac{h}{2}\right)^4 \frac{u^{(iv)}}{24} + O(h^6) \quad (4.38)$$

i.e., $p_{j+\frac{1}{2}}$ is fourth order accurate at $x_{j+\frac{1}{2}}$, and

$$p_{j-\frac{1}{2}}^A(x_{j+\frac{1}{2}}) = u - 4 \left(\frac{h}{2}\right)^3 \frac{u'''}{6} + \frac{256}{5} \left(\frac{h}{2}\right)^4 \frac{u^{(iv)}}{24} + O(h^5). \quad (4.39)$$

□

We need to use other limiters, at the place of the arithmetic mean, to get total variation stable reconstructions in a way that the truncation error expressions above are valid up to the highest possible order.

We apply our limiters on neighboring second order central differences. Thus, if x and y are neighboring second order central differences computed on a smooth region, we have that $x = O(h^2)$, $y = O(h^2)$ and $x - y = O(h^3)$ and, therefore,

Proposition 7

$$\frac{x+y}{2} - \text{power}_p(x, y) = O(h^{p+2})$$

Proof. It follows easily from

$$\begin{aligned} \frac{x+y}{2} - \text{power}_p(x, y) &= \frac{x+y}{2} \left[1 - 1 + \left| \frac{x-y}{x+y} \right|^p \right] \\ &= \frac{x+y}{2} \left| \frac{x-y}{x+y} \right|^p \\ &= O(h^{2+p}). \end{aligned} \quad (4.40)$$

□

Thus, the next theorem follows from Proposition 11.

Theorem 4 *The following statements are true:*

(1) The truncation error expressions of the arithmetic mean are valid up to third order terms for the *harmod* and *hareno* limiters, (the power_p limiters with $p = 2$).

(2) The truncation error expressions of the arithmetic mean are valid up to fourth order terms for the *powermod* and *powereno* limiters.

From Proposition 10 and Theorem 7 the following truncation error expressions at the right interface for the Power ENO parabolas are valid:

$$p_{j-\frac{1}{2}}^P(x_{j+\frac{1}{2}}) - u = -4 \left(\frac{h}{2}\right)^3 \frac{u'''}{6} + \frac{256}{5} \left(\frac{h}{2}\right)^4 \frac{u^{(iv)}}{24} + O(h^5)$$

$$p_j(x_{j+\frac{1}{2}}) - u = 4 \left(\frac{h}{2}\right)^3 \frac{u'''}{6} - \frac{64}{5} \left(\frac{h}{2}\right)^4 \frac{u^{(iv)}}{24} + O(h^5)$$

$$p_{j+\frac{1}{2}}^P(x_{j+\frac{1}{2}}) - u = -\frac{64}{5} \left(\frac{h}{2}\right)^4 \frac{u^{(iv)}}{24} + O(h^6)$$

Thus, from the above expressions we can reach fifth order accuracy at smooth regions, obtaining the optimal degree of accuracy using an analogous procedure to the one used in [13], (see also [20]).

Indeed, in this case the optimal linear weights C_k to get this accuracy are uniquely defined, at the right interface, as the convex combination:

$$w_0 \cdot p_{j-\frac{1}{2}}^P(x_{j+\frac{1}{2}}) + w_1 \cdot p_j(x_{j+\frac{1}{2}}) + w_2 \cdot p_{j+\frac{1}{2}}^P(x_{j+\frac{1}{2}}) \quad (4.41)$$

where

$$w_k = \frac{\alpha_k}{\alpha_0 + \alpha_1 + \alpha_2} \quad (4.42)$$

for $k = 0, 1, 2$, and

$$\alpha_k = \frac{C_k}{(\epsilon + IS_k)^2} \quad (4.43)$$

where $C_0 = 0.2$, $C_1 = 0.2$ and $C_2 = 0.6$ are the optimal weights, (we remind that the corresponding linear optimal weights for the WENO5 method are $C_0 = 0.1$, $C_1 = 0.6$ and $C_2 = 0.3$, see [13]).

Following Jiang and Shu, (see [13]), we define the indicator of smoothness of each of the involved parabolas as the weighted sum of the L^2 norms of all the derivatives of the parabola, computed on the computational cell. The weights of this sum are the spatial stepsize to the power corresponding to the order of the computed derivative. These weights are used to avoid the dependence of these indicators on the spatial grid. If $p_k(x)$ is the parabola, then

$$IS_k = \sum_{l=1}^2 \int_{x_{j-1/2}}^{x_{j+1/2}} h^{2l-1} (p_k^{(l)}(x))^2 dx$$

where $p_k^{(l)}(x)$ is the l th-derivative of the parabola $p_k(x)$.

Using this choice we can get the following property:

$$IS_k = D(1 + O(h^2))$$

where D is some nonzero quantity independent of the parabola p_k , in all the smooth regions. If the last property is ensured, then the optimal fifth order accuracy is achieved. In our case we obtain the following expressions for the indicator of smoothness:

$$IS_0 = \frac{13}{12} \left(P_{j-\frac{1}{2}} \right)^2 + \frac{1}{4} \left(2v_j - 2v_{j-1} + P_{j-\frac{1}{2}} \right)^2 \quad (4.44)$$

$$IS_1 = \frac{13}{12} (v_{j-1} - 2v_j + v_{j+1})^2 + \frac{1}{4} (v_{j-1} - v_{j+1})^2 \quad (4.45)$$

$$IS_2 = \frac{13}{12} \left(P_{j+\frac{1}{2}} \right)^2 + \frac{1}{4} \left(2v_{j+1} - 2v_j - P_{j+\frac{1}{2}} \right)^2 \quad (4.46)$$

where P is the powereno or powermod limiter, computed for the two neighboring second order differences.

Thus, the resulting method is a fifth order accurate weighted Power ENO method, we will call Weighted Power ENO.

We can compare with the indicators obtained for the Jiang-Shu WENO5 method, (see [13]):

$$IS_{0_{weno5}} = \frac{13}{12} (v_{j-2} - 2v_{j-1} + v_j)^2 + \frac{1}{4} (v_{j-2} - 4v_{j-1} + 3v_j)^2$$

$$IS_{1_{weno5}} = \frac{13}{12} (v_{j-1} - 2v_j + v_{j+1})^2 + \frac{1}{4} (v_{j-1} - v_{j+1})^2$$

$$IS_{2_{weno5}} = \frac{13}{12} (v_j - 2v_{j+1} + v_{j+2})^2 + \frac{1}{4} (3v_j - 4v_{j+1} + v_{j+2})^2$$

We remark that the central one is exactly the same.

The Taylor expansions of (8.71), (8.72) and (8.73) in smooth regions are

$$IS_0 = \frac{13}{12} (u''h^2)^2 + \frac{1}{4} \left(2u'h - u''h^2 + \frac{1}{6}u'''h^3 \right)^2 + O(h^6)$$

$$IS_1 = \frac{13}{12} (u''h^2)^2 + \frac{1}{4} \left(2u'h + \frac{1}{3}u'''h^3 \right)^2 + O(h^6)$$

$$IS_2 = \frac{13}{12} (u''h^2)^2 + \frac{1}{4} \left(2u'h - u''h^2 + \frac{1}{6}u'''h^3 \right)^2 + O(h^6)$$

and, therefore, we have the same advantages of the Jiang-Shu WENO5 method.

We compare the behavior of the smoothness measurement for our Weighted Power ENO5 and the Jiang-Shu WENO5 in smooth regions and near critical points (jump discontinuities, discontinuities in derivative,...). First, we compute the weights w_0 , w_1 and w_2 for the following function u_1 , (proposed by Jiang and Shu in [13]), at all right interfaces $x_{j+\frac{1}{2}}$, $x_j = jh$ with $h = \frac{1}{40}$

$$u_1(x, 0) = \begin{cases} \sin 2\pi x & 0 \leq x \leq 0.5 \\ 1 - \sin 2\pi x & 0.5 < x \leq 1 \end{cases}$$

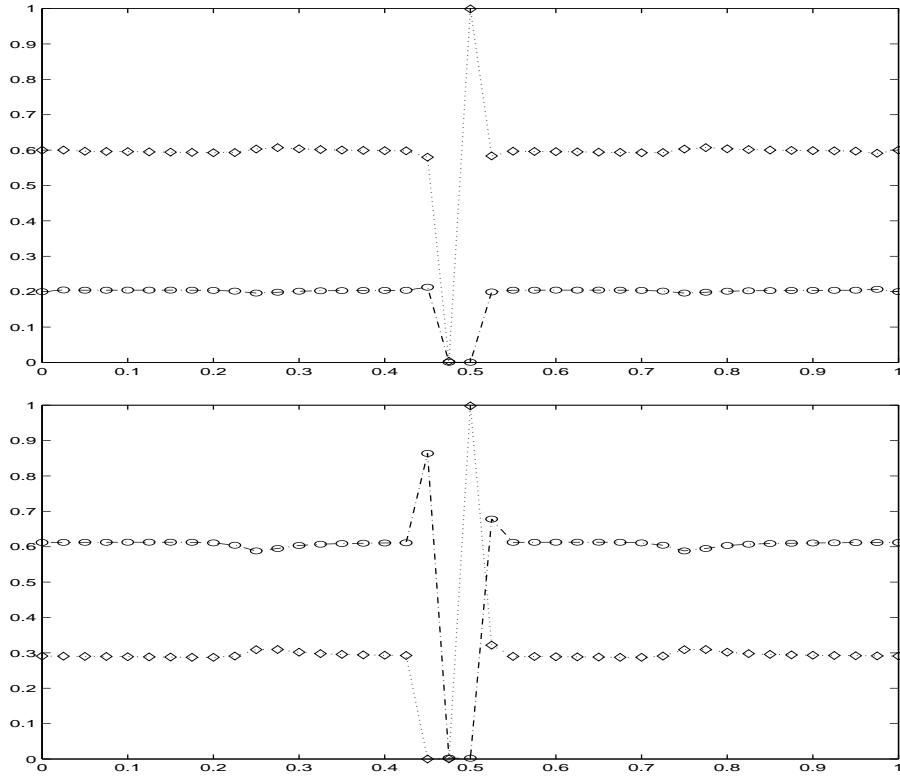


Figure 4.1: A comparison of smoothness measurements for a jump discontinuity:
Weighted Power ENO5 (top), WENO5 (bottom)

We display the weights w_1 and w_2 in Figure 4.1 for both methods. We observe that for the smooth region both measurements behave similarly, that is, they achieve the optimal weights for 5th order accuracy. Both methods degenerate to the corresponding digital ENO method (ENO3 or Power-ENO3) at the points of discontinuity. However, at the points next to the discontinuity, our method get optimal weights of accuracy, and the WENO5 weights degenerates to third order accuracy.

Secondly, we compute the weights w_0 , w_1 and w_2 for the function u_2 , defined

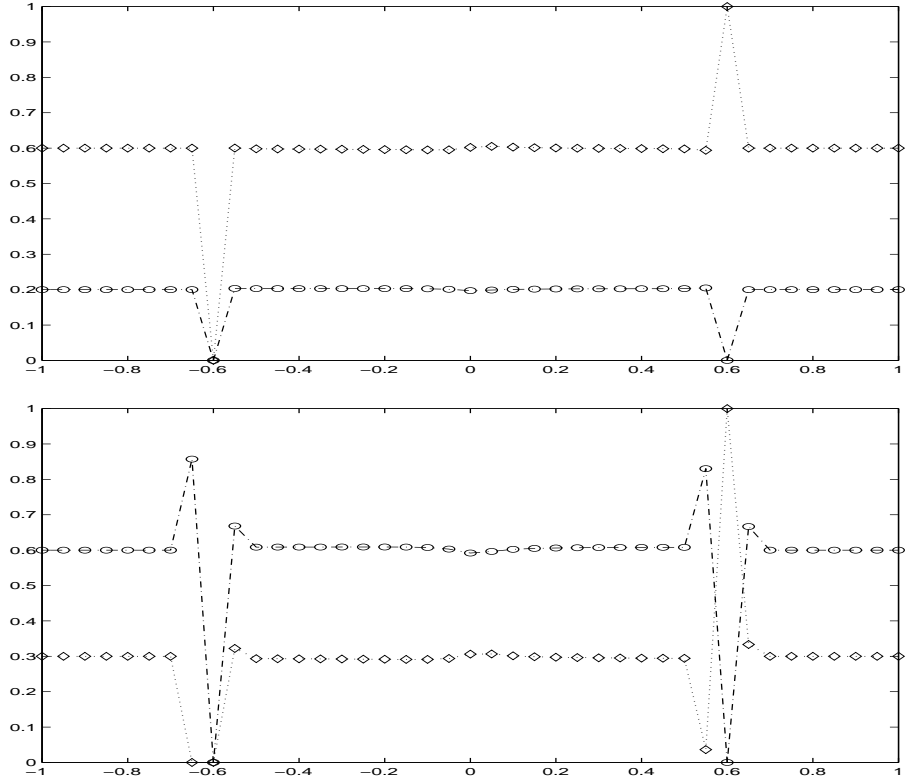


Figure 4.2: A comparison of smoothness measurements for two discontinuities in derivative: Weighted Power ENO5 (top), WENO5 (bottom).

on $[-1, 1]$, with two discontinuities in the first derivative, at all right interfaces $x_{j+\frac{1}{2}}$, with $x_j = -1 + jh$ and $h = \frac{1}{40}$:

$$u_2(x, 0) = \begin{cases} \sin(\pi \frac{x+0.6}{1.2}) & -0.6 \leq x \leq 0.6 \\ 0 & \text{otherwise} \end{cases}$$

We display the weights w_1 and w_2 in Figure 4.2 for both methods. We observe that our method only degenerates to the digital Power-ENO3 at one point to resolve each critical point, while WENO5 degenerates to third order at two points

next to each critical point.

We conclude this section with the algorithm for the Weighted PowerENO method.

4.3.2.1 Algorithm for the Weighted PowerENO method

Let v_{j-2} , v_{j-1} , v_j , v_{j+1} and v_{j+2} be the necessary data (stencil) to compute the lateral approximations at $x_{j-\frac{1}{2}}$ and $x_{j+\frac{1}{2}}$.

Let us compute $d_{j-\frac{1}{2}}$ and $d_{j+\frac{1}{2}}$ as in (8.38), d_j as in (8.55), and D_{j-1} , D_j and D_{j+1} as in (8.56).

Using these values we can compute $P_{j-\frac{1}{2}} = \text{powereno}(D_{j-1}, D_j)$ and $P_{j+\frac{1}{2}} = \text{powereno}(D_j, D_{j+1})$ as explained in Chapter 8.3 and then, compute IS_0 , IS_1 and IS_2 using the expressions (8.71), (8.72) and (8.73).

- For the approximation at $x_{j+\frac{1}{2}}$, compute:

$$a_0 = \frac{0.2}{\sqrt{\epsilon + IS_0}}, \quad a_1 = \frac{0.2}{\sqrt{\epsilon + IS_1}}, \quad a_2 = \frac{0.6}{\sqrt{\epsilon + IS_2}}$$

$$w_0 = \frac{a_0}{a_0 + a_1 + a_2}, \quad w_1 = \frac{a_1}{a_0 + a_1 + a_2}, \quad w_2 = \frac{a_2}{a_0 + a_1 + a_2}$$

Considering simple expressions for the parabolas (8.62), (8.63) and (8.64) at the right interface $x_{j+\frac{1}{2}}$,

$$p_{j-\frac{1}{2}}(x_{j+\frac{1}{2}}) = v_j + \frac{1}{2}d_{j-\frac{1}{2}} + \frac{1}{3}P_{j-\frac{1}{2}}$$

$$p_j(x_{j+\frac{1}{2}}) = v_j + \frac{1}{2}d_j + \frac{1}{12}D_j$$

$$p_{j+\frac{1}{2}}(x_{j+\frac{1}{2}}) = v_j + \frac{1}{2}d_{j+\frac{1}{2}} - \frac{1}{6}P_{j+\frac{1}{2}}$$

we get the approximation by means of the convex combination:

$$w_0 \cdot p_{j-\frac{1}{2}}(x_{j+\frac{1}{2}}) + w_1 \cdot p_j(x_{j+\frac{1}{2}}) + w_2 \cdot p_{j+\frac{1}{2}}(x_{j+\frac{1}{2}})$$

- For the approximation at $x_{j-\frac{1}{2}}$, compute:

$$\begin{aligned} a_0 &= \frac{0.6}{\sqrt{\epsilon + IS_0}}, & a_1 &= \frac{0.2}{\sqrt{\epsilon + IS_1}}, & a_2 &= \frac{0.2}{\sqrt{\epsilon + IS_2}} \\ w_0 &= \frac{a_0}{a_0 + a_1 + a_2}, & w_1 &= \frac{a_1}{a_0 + a_1 + a_2}, & w_2 &= \frac{a_2}{a_0 + a_1 + a_2} \end{aligned}$$

Considering simple expressions for the parabolas (8.62), (8.63) and (8.64)

at the left interface $x_{j-\frac{1}{2}}$,

$$p_{j-\frac{1}{2}}(x_{j-\frac{1}{2}}) = v_j - \frac{1}{2}d_{j-\frac{1}{2}} - \frac{1}{6}P_{j-\frac{1}{2}}$$

$$p_j(x_{j-\frac{1}{2}}) = v_j - \frac{1}{2}d_j + \frac{1}{12}D_j$$

$$p_{j+\frac{1}{2}}(x_{j+\frac{1}{2}}) = v_j - \frac{1}{2}d_{j+\frac{1}{2}} + \frac{1}{6}P_{j+\frac{1}{2}}$$

we get the approximation by means of the convex combination:

$$w_0 \cdot p_{j-\frac{1}{2}}(x_{j-\frac{1}{2}}) + w_1 \cdot p_j(x_{j-\frac{1}{2}}) + w_2 \cdot p_{j+\frac{1}{2}}(x_{j-\frac{1}{2}})$$

CHAPTER 5

Numerical Experiments

5.1 Introduction

In this Chapter we test numerically the behavior of the reconstruction procedures studied in the previous Chapter. We perform numerical experiments for the linear advection and Euler equations of gas dynamics in one and two dimensions.

5.2 Numerical Implementation

To ensure that shocks and other waves are captured by the scheme, we have seen that we must write the equation in a discrete conservation form. We have derived the discrete conservation form by integrating the conservation law and assuming that we evolve cell averages values in time rather than nodal point values. The difficulty with this formulation is that it requires transforming between cell averages of u (evolved in time by the scheme) and cell interface values of u (which must be reconstructed) to evaluate the needed fluxes. This procedure is simple in one dimension but becomes complicated in higher dimensional problems when to achieve high order spatial accuracy is wanted. Shu and Osher [36], proposed a fully conservative finite difference scheme on uniform grids that evolves point

values forward in time. They defined a numerical flux function $g(x)$ by imposing that the flux divergence be a finite difference of numerical fluxes:

$$f(u(x))_x = \frac{g(x + \frac{h}{2}) - g(x - \frac{h}{2})}{h} \quad (5.1)$$

Thus, a finite difference discretization can be based on

$$u_t + \frac{g(x + \frac{h}{2}) - g(x - \frac{h}{2})}{h} = 0 \quad (5.2)$$

to evolve point values of u in time using numerical fluxes g at the cell interfaces.

In order to get high order accuracy in space we use the so-called “flux formulation” by Shu and Osher [36], based on the following simple lemma:

Lemma 3 *If a function $g(x)$ satisfies*

$$f(u(x)) = \frac{1}{h} \int_{x - \frac{h}{2}}^{x + \frac{h}{2}} g(\psi) d\psi \quad (5.3)$$

then

$$f(u(x))_x = \frac{g(x + \frac{h}{2}) - g(x - \frac{h}{2})}{h} \quad (5.4)$$

The procedure to implement a high order accurate shock capturing scheme reads as follows:

We start with a first order monotone scheme based on a monotone numerical flux. Then we compute the numerical fluxes and variables at both sides of the cell interfaces using a reconstruction procedure to approximate the numerical fluxes (and variables), solving the equation (5.3) up to some degree of accuracy. We use

those high order accurate values to compute the monotone flux function to obtain the numerical flux at the cell interfaces. Thus we use the discrete conservation form to evolve in time.

In order to be consistent with the spatial accuracy, the time discretization of the schemes under study will be implemented by the third order TVD Runge-Kutta type method developed by Shu and Osher in [36]. This evolution in time is computed by the recurrent formula:

$$u_j^{(i)} = \sum_{k=0}^{i-1} \left[\alpha_{ik} \cdot u_j^{(k)} + \beta_{ik} \cdot (-\lambda) \cdot (\tilde{f}_{j+\frac{1}{2}}^{(k)} - \tilde{f}_{j-\frac{1}{2}}^{(k)}) \right], \quad i = 1, 2, 3 \quad (5.5)$$

where

$$u_j^{(0)} = u_j^n, \quad u_j^{(3)} = u_j^{n+1} \quad (5.6)$$

with coefficients of Table 5.1. The resulting scheme is a convex combination of three Euler explicit time-stepping schemes in conservation form.

Table 5.1: *Third order TVD Runge-Kutta scheme*

	α_{1k}	α_{2k}	α_{3k}	β_{1k}	β_{2k}	β_{3k}
k=0	1	$\frac{3}{4}$	$\frac{1}{3}$	1	0	0
k=1	0	$\frac{1}{4}$	0	0	$\frac{1}{4}$	0
k=2	0	0	$\frac{2}{3}$	0	0	$\frac{2}{3}$

This Euler explicit time-stepping procedure is total variation stable under a suitable CFL restriction $\lambda = \frac{\Delta t}{h} \leq \lambda_0$ where λ_0 is inversely proportional to $\max |f'(u)|$ as usual.

In multiple dimensions the one-dimensional “flux formulation” is applied using a dimension-by-dimension procedure. For a two dimensional scalar conservation law

$$u_t + f(u)_x + g(u)_y = 0 \quad (5.7)$$

we compute the term $f(u)_x$ using the one-dimensional procedure and freezing the other variable (y), and $g(u)_y$ is computed in an analogous way freezing the x variable. Once we have the numerical approximation of each of the spatial terms, we evolve the entire equation in time with a method-of-lines using the TVD Runge-Kutta method mentioned above.

All the above apply to scalar conservation laws.

A hyperbolic system of conservation laws is written in terms of conserved variables and fluxes where physical magnitudes are mixed. A transformation is needed to decouple a simple one dimensional system of n equations

$$\bar{u}_t + \bar{f}(\bar{u})_x = 0 \quad (5.8)$$

into a system of n independent scalar equations of the form

$$u_t + \lambda u_x = 0 \quad (5.9)$$

This is called a transformation to characteristic variables, being λ the characteristic speeds.

When (5.8) is nonlinear, this transformation can not be global and then we expect to compute local transformations by diagonalizing the Jacobian of the flux

computed at every point of the solution. Indeed, in a smooth region of the flow we can use

$$\bar{u}_t + J\bar{u}_x = 0 \quad (5.10)$$

instead of (5.8) being $J = \frac{\partial \bar{f}(\bar{u})}{\partial \bar{u}}$ the Jacobian matrix of the flux $\bar{f}(\bar{u})$.

In general, J is not a diagonal matrix but it can be transformed into a diagonal one by means of an invertible matrix when the system is hyperbolic. In this case J has n real eigenvalues $\lambda_p(\bar{u})$, $p = 1, \dots, n$, and n linearly independent right eigenvectors being the columns of a matrix R , $\mathbf{r}_p(\bar{u})$, $p = 1, \dots, n$. There are n independent left eigenvectors, $\mathbf{l}_p(\bar{u})$, $p = 1, \dots, n$ being the rows of the matrix L .

We have

$$\mathbf{l}_j(\bar{u}) \cdot \mathbf{r}_k(\bar{u}) = \delta_{ij} \quad (5.11)$$

If $D = \text{diag}\{\lambda_1(\bar{u}), \lambda_2(\bar{u}), \dots, \lambda_n(\bar{u})\}$ then, $LJR = D$.

We wish to discretize the hyperbolic system (5.8) in conservation form

$$\bar{u}_j^{n+1} = \bar{u}_j^n - \frac{\Delta t}{h} [\tilde{f}_{j+\frac{1}{2}} - \tilde{f}_{j-\frac{1}{2}}] \quad (5.12)$$

We want to find the numerical flux vector function $\tilde{f}_{j+\frac{1}{2}}$ in terms of the eigen-system information at the cell interface $x_{j+\frac{1}{2}}$ between two nodes.

The standard way to compute $\tilde{f}_{j+\frac{1}{2}}$ is to evaluate the eigensystem at the average

$$\tilde{u}_{j+\frac{1}{2}} = \frac{\bar{u}_j + \bar{u}_{j+1}}{2},$$

i.e., $L(\tilde{u}_{j+\frac{1}{2}})$ and $R(\tilde{u}_{j+\frac{1}{2}})$, ([36]).

Then, we compute the characteristic fluxes and variables and we apply the procedure used for scalar conservation laws to compute the characteristic numerical flux in every characteristic field p . Then, the numerical flux $\tilde{f}_{j+\frac{1}{2}}$ is calculated by adding the contributions of each characteristic numerical flux multiplied by the corresponding right eigenvector.

An advanced way to compute the numerical flux vector function is the one proposed by Marquina [4], (Marquina Flux Formula, MFF) that reads as follows:

Given the left and right states \bar{u}_l and \bar{u}_r respectively, we compute the “sided” local characteristic variables and fluxes by means of the corresponding “sided” left eigenvectors, $\mathbf{l}^p(\bar{u}_l)$ and $\mathbf{l}^p(\bar{u}_r)$ for $p = 1, \dots, n$ as

$$w_l^p = \mathbf{l}^p(\bar{u}_l) \cdot \bar{u}_l \quad \phi_l^p = \mathbf{l}^p(\bar{u}_l) \cdot f(\bar{u}_l) \quad (5.13)$$

$$w_r^p = \mathbf{l}^p(\bar{u}_r) \cdot \bar{u}_r \quad \phi_r^p = \mathbf{l}^p(\bar{u}_r) \cdot f(\bar{u}_r) \quad (5.14)$$

Let $\lambda_1(\bar{u}_l), \dots, \lambda_m(\bar{u}_l)$ and $\lambda_1(\bar{u}_r), \dots, \lambda_m(\bar{u}_r)$ be their corresponding eigenvalues.

We proceed as follows:

If $\lambda_k(\bar{u})$ does not change sign in $[\bar{u}_l, \bar{u}_r]$, **then**

If $\lambda_k(\bar{u}_l) > 0$ **then**

$$\phi_+^k = \phi_l^k$$

$$\phi_-^k = 0$$

else

```

 $\phi_+^k = 0$ 
 $\phi_-^k = \phi_r^k$ 
endif
else
 $\alpha_k = \max_{u \in \Gamma(\bar{u}_l, \bar{u}_r)} |\lambda_k(\bar{u})|$ 
 $\phi_+^k = 0.5(\phi_l^k + \alpha_k w_l^k)$ 
 $\phi_-^k = 0.5(\phi_r^k + \alpha_k w_r^k)$ 

```

end

$\Gamma(\bar{u}_l, \bar{u}_r)$ is a curve in phase space connecting \bar{u}_l and \bar{u}_r . This means that in every characteristic field we solve the Riemann problem by using Godunov scheme for non-transonic wavefields and local Lax-Friedrichs scheme for transonic ones. The positive parameter α_k is the local viscosity associated to the local characteristic field in a neighborhood of the interface.

For the Euler equations of gas dynamics, the fields are either genuinely non-linear or linearly degenerate. Hence we can test the possible sign changes of $\lambda_k(\bar{u})$ by checking the sign of $\lambda_k(\bar{u}_l) \cdot \lambda_k(\bar{u}_r)$ and, α_k can be determined in a very simple way as

$$\alpha_k = \max(|\lambda_k(\bar{u}_l)|, |\lambda_k(\bar{u}_r)|)$$

Thus, the Marquina Flux Formula reads as follows:

$$F^M(\bar{u}_l, \bar{u}_r) = \sum_{p=1}^m (\phi_+^p \mathbf{r}^p(\bar{u}_l) + \phi_-^p \mathbf{r}^p(\bar{u}_r)) \quad (5.15)$$

where $\mathbf{r}^p(\bar{u}_l)$ and $\mathbf{r}^p(\bar{u}_r)$ are the right eigenvectors of the Jacobian matrices $J_F(\bar{u}_l)$ and $J_F(\bar{u}_r)$ respectively.

The first order scheme is,

$$\bar{u}_j^{n+1} = \bar{u}_j^n - \frac{\Delta t}{h} \left(F^M(\bar{u}_j^n, \bar{u}_{j+1}^n) - F^M(\bar{u}_{j-1}^n, \bar{u}_j^n) \right) \quad (5.16)$$

where the numerical flux vector function F^M is consistent with the flux vector function of the system, i.e., $F^M(\bar{u}, \bar{u}) = \bar{f}(\bar{u})$.

This numerical flux resembles a flux-splitting formula with

$$F^M(\bar{u}, \bar{v}) = F^+(\bar{u}) + F^-(\bar{v}) \quad (5.17)$$

where

$$F^+(\bar{u}) = \sum \phi_+^p \mathbf{r}^p(\bar{u}), \quad F^-(\bar{u}) = \sum \phi_-^p \mathbf{r}^p(\bar{v}) \quad (5.18)$$

being the characteristic numerical fluxes $\phi_{\pm} = \phi_{\pm}(\bar{u}, \bar{v})$ depending (in a very nonlinear way) on the left and right states, ([4],[33]).

5.3 Euler equations

The basic equations for the two-dimensional compressible flow are the 2D Euler equations,

$$U_t + F(U)_x + G(U)_y = 0, \quad (5.19)$$

where,

$$U = \begin{bmatrix} \rho \\ \rho u \\ \rho v \\ E \end{bmatrix} \quad F(U) = \begin{bmatrix} \rho u \\ \rho u^2 + P \\ \rho u v \\ (E + P)u \end{bmatrix} \quad G(U) = \begin{bmatrix} \rho v \\ \rho u v \\ \rho v^2 + P \\ (E + P)v \end{bmatrix}$$

being ρ the density, u and v the velocities in the $x-$ and $y-$ directions respectively, P the pressure and

$$E = \frac{1}{2}\rho(u^2 + v^2) + \rho\epsilon \quad (5.20)$$

the total energy where ϵ is the specific internal energy per unit volume.

The one-dimensional Euler equations are obtained by setting $v = 0$.

We compute the pressure by means of the ideal gas equation of state

$$P = (\gamma - 1)\rho\epsilon$$

where γ is the adiabatic exponent. We use $\gamma = 1.4$ in our experiments.

The analytical expression of the Jacobian matrix of the flux F , J_F , is

$$J_F = \begin{bmatrix} 0 & 1 & 0 & 0 \\ c_s^2 - u^2 + (\gamma - 1)(H + q^2) & -u(\gamma - 3) & -v(\gamma - 1) & \gamma - 1 \\ -uv & v & u & 0 \\ u(c_s^2 - H + (\gamma - 1)(H + q^2)) & H - u^2(\gamma - 1) & -uv(\gamma - 1) & u\gamma \end{bmatrix}$$

where $c_s = \sqrt{\gamma \frac{P}{\rho}}$ is the sound speed,

$$H = \frac{E + P}{\rho} = \frac{c_s^2}{\gamma - 1} + \frac{1}{2}(u^2 + v^2)$$

is the enthalpy and $q^2 = u^2 + v^2$.

The eigenvalues of this Jacobian are:

$$\lambda_1 = u - c_s, \quad \lambda_2 = u, \quad \lambda_3 = u, \quad \lambda_4 = u + c_s \quad (5.21)$$

and the complete set of right-eigenvectors

$$R^F = \begin{bmatrix} r_1 & r_2 & r_3 & r_4 \end{bmatrix} = \begin{bmatrix} 1 & 1 & 0 & 1 \\ u - c_s & u & 0 & u + c_s \\ v & v & 1 & v \\ H - uc_s & \frac{u^2 + v^2}{2} & v & H + uc_s \end{bmatrix}$$

with the corresponding left-eigenvectors

$$L^F = \begin{bmatrix} l_1 \\ l_2 \\ l_3 \\ l_4 \end{bmatrix} = \begin{bmatrix} b_2 + \frac{u}{2c_s} & -b_1u - \frac{1}{2c_s} & -b_1v & b_1 \\ 1 - 2b_2 & 2ub_1 & 2vb_1 & -2b_1 \\ -v & 0 & 1 & 0 \\ b_2 - \frac{u}{2c_s} & -b_1u + \frac{1}{2c_s} & -b_1v & b_1 \end{bmatrix}$$

where

$$b_1 = \frac{\gamma - 1}{2c_s^2}, \quad b_2 = b_1 \left(\frac{u^2 + v^2}{2} \right)$$

The eigenvectors of the Jacobian in the y -direction, (J_G), are obtained by changing the roles of u and v and the second and third components of each left and right eigenvector.

5.4 PowerPHM method. Experiments

5.4.1 Linear advection

For the linear advection test, PowerPHM has been based on the Godunov's first order scheme for scalar conservation laws. We use the label PowerPHM-GOD to refer to this scheme.

We solve the linear equation $u_t + u_x = 0$, $-1 \leq x \leq 1$ with $u(x, 0) = u_0(x)$ periodic.

$$u_0(x) = \begin{cases} 1 & -0.7 \leq x \leq -0.2 \\ \sin\left(\pi \frac{x+0.2}{0.6}\right) & 0.2 \leq x \leq 0.8 \\ 0 & \text{otherwise} \end{cases}$$

We compute the approximate solution for PHM and PowerPHM using a grid of 200 points with CFL factor of 0.8 and total time of 5 periods.

We observe, in Fig. 5.1, a substantial improvement in resolving local extrema, jump discontinuities and discontinuities in first derivative of the signal for the PowerPHM scheme compared with the PHM.

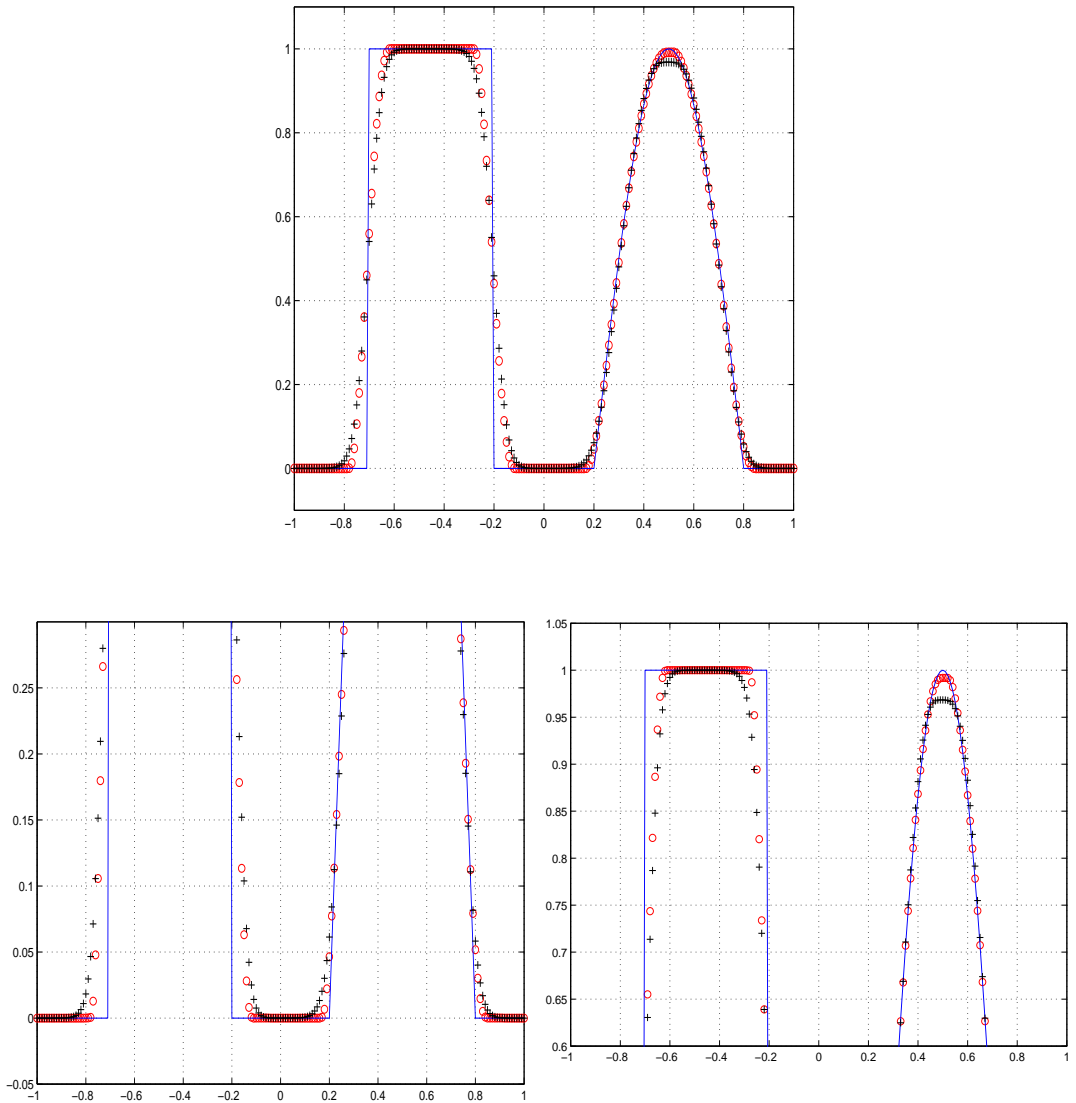


Figure 5.1: Numerical solution of linear advection at $t=10$, $CFL=0.8$ and 200 points for PHM-GOD scheme “+” and PowerPHM-GOD schemes “o”.

5.4.2 Euler equations: One dimensional experiments

The PHM and PowerPHM schemes we have implemented for systems of conservation laws are based on the first order Marquina's Flux Formula (MFF),[4], applying the third order reconstruction procedure to the local characteristic fluxes and variables, and using the third order accurate TVD Runge-Kutta method for the evolution in time as explained in section 5.2.

We use the labels PHM-MFF or PowerPHM-MFF to refer to these schemes.

5.4.2.1 Lax's Tube

We consider the following Riemann problem due to Lax ([15]):

$$(\rho_0, u_0, P_0) = \begin{cases} (0.445, 0.698, 3.528) & -5 \leq x < 0 \\ (0.5, 0, 0.571) & 0 \leq x \leq 5 \end{cases}$$

We have displayed in Figure 5.2 and Figure 5.3 the density profile of Lax's tube at time $t = 1.3$ and its zoomed regions respectively. We obtain correct position and speed of discontinuities. We can observe a reduction of the smearing of the contact wave for our PowerPHM method in comparison with PHM. The interesting feature of our PowerPHM method is the sharpening of jump discontinuities with the same order of spatial accuracy as the classical PHM.

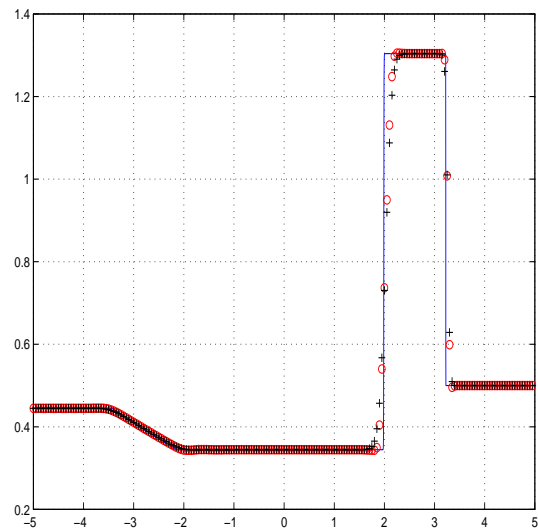


Figure 5.2: Numerical solution of the density profile for the Lax's problem at $t=1.3$, $CFL=0.8$, 200 points for the PHM-MFF scheme “+” and PowerPHM-MFF scheme “o”.

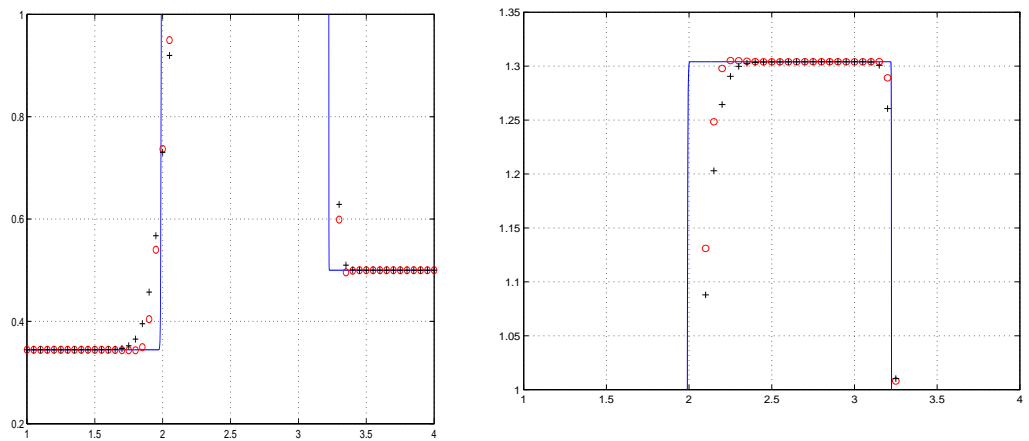


Figure 5.3: Zoomed regions of the density profile of Lax's problem

5.4.2.2 Shock entropy wave interaction

We consider the one-dimensional wave interaction introduced in [36] for testing stability and accuracy of high order methods. The initial data are

$$(\rho_0, u_0, P_0) = \begin{cases} (3.85714, 2.62936, 10.33333) & -5 \leq x < -4 \\ (1 + 0.2 \sin(5x), 0, 1) & -4 \leq x \leq 5 \end{cases}$$

We use a uniform grid with 200 points and we evolve until time 1.8 using PHM-MFF and PowerPHM-MFF. We display in Fig. 5.4 a zoomed area of the perturbed region behind the shock wave where we observe an improved resolution of local extrema for our PowerPHM scheme compared with PHM.

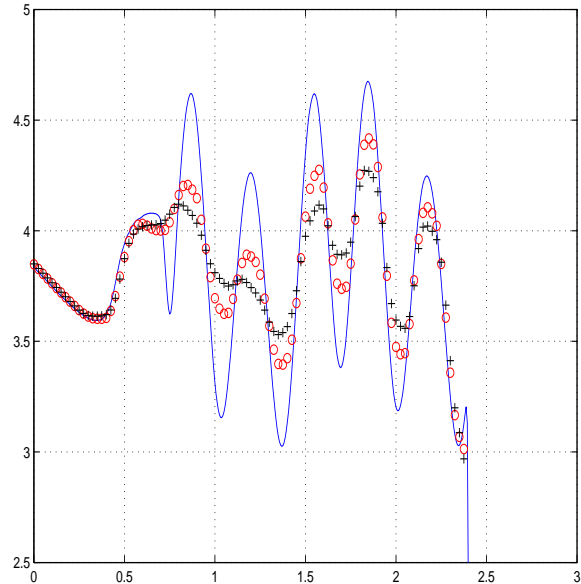


Figure 5.4: Zoomed region of the numerical solution of the density profile for the shock-entropy wave interaction with PHM-MFF “+” and PowerPHM-MFF “o”, using a grid of 200 points with $CFL=0.8$ until time 1.8 .

5.4.3 Euler equations: Two-dimensional Riemann problem

We consider the Riemann problem corresponding to Configuration 3 defined in [32] in the domain $[0, 1] \times [0, 1]$ localizing the contact point at $(0.75, 0.75)$ instead of the center of the square.

The initial data read as:

First quadrant, $([0.75, 1] \times [0.75, 1])$, $(\rho, u, v, P) = (1.5, 0, 0, 1.5)$.

Second quadrant, $([0, 0.75] \times [0.75, 1])$, $(\rho, u, v, P) = (0.5323, 1.206, 0, 0.3)$.

Third quadrant, $([0, 0.75] \times [0, 0.75])$, $(\rho, u, v, P) = (0.138, 1.206, 1.206, 0.029)$.

Fourth quadrant, $([0.75, 1] \times [0, 0.75])$, $(\rho, u, v, P) = (0.5323, 0, 1.206, 0.3)$.

We evolve in time until 0.8 with a CFL factor of 0.8 and a grid of 400x400 points. In Figure 5.5 we display the approximations of the density contour profile obtained with the PHM-MFF and PowerPHM-MFF schemes. We can observe a substantial improvement at the contact where the instability is manifest for the PowerPHM-MFF scheme. We also notice a better resolution of the structure appearing at the top right region for the PowerPHM-MFF scheme.

5.5 Power ENO and Weighted Power ENO methods. Experiments

5.5.1 Study of convergence

Next, we focus our attention on testing the accuracy of our Weighted Power ENO5 method on the linear advection initial value problem:

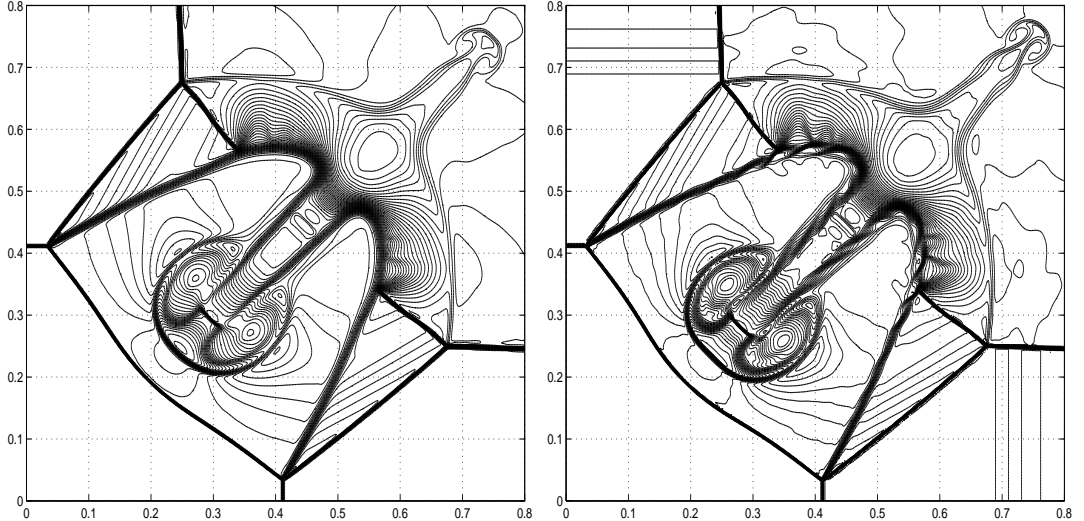


Figure 5.5: Zoomed region of the density contour lines of the numerical solution of the two-dimensional Riemann problem using 400×400 points, $CFL=0.8$, at time 0.8 for the PHM-MFF scheme (left) and PowerPHM-MFF (right).

$$u_t + u_x = 0 \quad (5.22)$$

$$u(x, 0) = \frac{1}{2} \left(\frac{1}{2} + \sin(2\pi x) \right) \quad (5.23)$$

We have implemented the third order TVD Runge-Kutta method for the integration in time using a time step $\Delta t \approx (\Delta x)^{\frac{5}{3}}$ so that we reach 5th order accuracy in time.

The use of nonsmooth limiters as, in our case, the powereno limiter, makes the numerical convergence noisier. The nonsmooth behavior of powereno limiter follows easily from (3.38) written in terms of the max and min functions. From

Table 5.2: *Absolute Errors for Weighted Power ENO5 and WENO5 methods*

N	L_1 -error		L_∞ -error	
	WPower ENO5	WENO5	WPower-ENO5	WENO5
80	$1.75 \cdot 10^{-5}$	$7.17 \cdot 10^{-7}$	$1.53 \cdot 10^{-4}$	$1.37 \cdot 10^{-6}$
160	$9.40 \cdot 10^{-7}$	$2.24 \cdot 10^{-8}$	$9.58 \cdot 10^{-6}$	$4.18 \cdot 10^{-8}$
320	$3.09 \cdot 10^{-8}$	$7.08 \cdot 10^{-10}$	$6.27 \cdot 10^{-7}$	$1.23 \cdot 10^{-9}$
640	$1.40 \cdot 10^{-9}$	$2.29 \cdot 10^{-11}$	$6.86 \cdot 10^{-8}$	$4.02 \cdot 10^{-11}$
1280	$5.01 \cdot 10^{-11}$	$7.03 \cdot 10^{-13}$	$2.67 \cdot 10^{-9}$	$1.06 \cdot 10^{-12}$

the Taylor expansions discussed above it follows that when the second order differences do not change sign, the powereno is smooth enough to reach optimal accuracy, but at the smooth inflection points the lack of regularity of the limiter makes our scheme less accurate.

We display in Tables 5.2 and 5.3 the L_1 and L_∞ absolute errors and numerical orders respectively, computed for both methods. We observe for the Weighted Power ENO method that there is a loss of accuracy, (still present when refining the grid), as it can be seen at the table of absolute errors. This is due to numerical degeneration occurring near inflection points.

In order to check numerically this claim we display in Table 5.4 the corresponding L_1 and L_∞ errors removing a small neighborhood of the inflection points for different grids. We obtain in this case similar L_1 and L_∞ errors to the corresponding values for the Jiang-Shu WENO5 method.

Table 5.3: Numerical Orders for Weighted Power ENO5 and WENO5 methods

N	L_1 -order		L_∞ -order	
	WPower-ENO5	WENO5	WPower-ENO5	WENO5
160	—	—	—	—
320	4.22	4.99	3.86	5.04
640	4.97	4.99	4.46	5.08
1280	4.80	5.01	4.68	5.04

Table 5.4: Absolute Errors for Weighted Power ENO5 and WENO5, excluding inflection points

N	L_1 -error		L_∞ -error	
	WPower-ENO5	WENO5	WPower-ENO5	WENO5
80	$4.17 \cdot 10^{-6}$	$8.76 \cdot 10^{-7}$	$1.62 \cdot 10^{-5}$	$1.35 \cdot 10^{-6}$
160	$9.85 \cdot 10^{-8}$	$2.72 \cdot 10^{-8}$	$6.88 \cdot 10^{-7}$	$4.18 \cdot 10^{-8}$
320	$2.00 \cdot 10^{-10}$	$8.27 \cdot 10^{-10}$	$9.84 \cdot 10^{-10}$	$1.23 \cdot 10^{-9}$
640	$6.89 \cdot 10^{-12}$	$2.46 \cdot 10^{-11}$	$4.81 \cdot 10^{-11}$	$4.01 \cdot 10^{-11}$

5.5.2 Linear advection

We solve the linear equation

$$u_t + u_x = 0, \quad a \leq x \leq b$$

with $u(x, 0) = u_0(x)$ periodic in $[a, b]$, for the cases:

- **Example 1** In $[a, b] = [0, 1]$ let us consider the initial data,

$$u_0(x) = \begin{cases} 1 & 0.35 \leq x \leq 0.65 \\ 0 & \text{otherwise} \end{cases}$$

- **Example 2** In $[a, b] = [-1, 1]$, let us consider the initial data,

$$u_0(x) = \begin{cases} \sin\left(\pi \frac{x+0.3}{0.6}\right) & -0.3 \leq x \leq 0.3 \\ 0 & \text{otherwise} \end{cases}$$

We compute the approximate solution and compare the results for the third order PowerENO method versus ENO method and for the Weighted PowerENO method versus WENO method.

The calculations have been performed using the Godunov's scheme and the Shu-Osher third order Runge-Kutta integration in time, (see [36]), with a grid of 100 points, $\Delta t/h = 0.5$, and total time of two periods.

In Figure 5.6 we display the numerical approximation of Example 1 using the ENO3 and PowerENO3 methods represented with '+' and 'o' signs, respectively. We observe an improved behavior near discontinuities for our PowerENO3

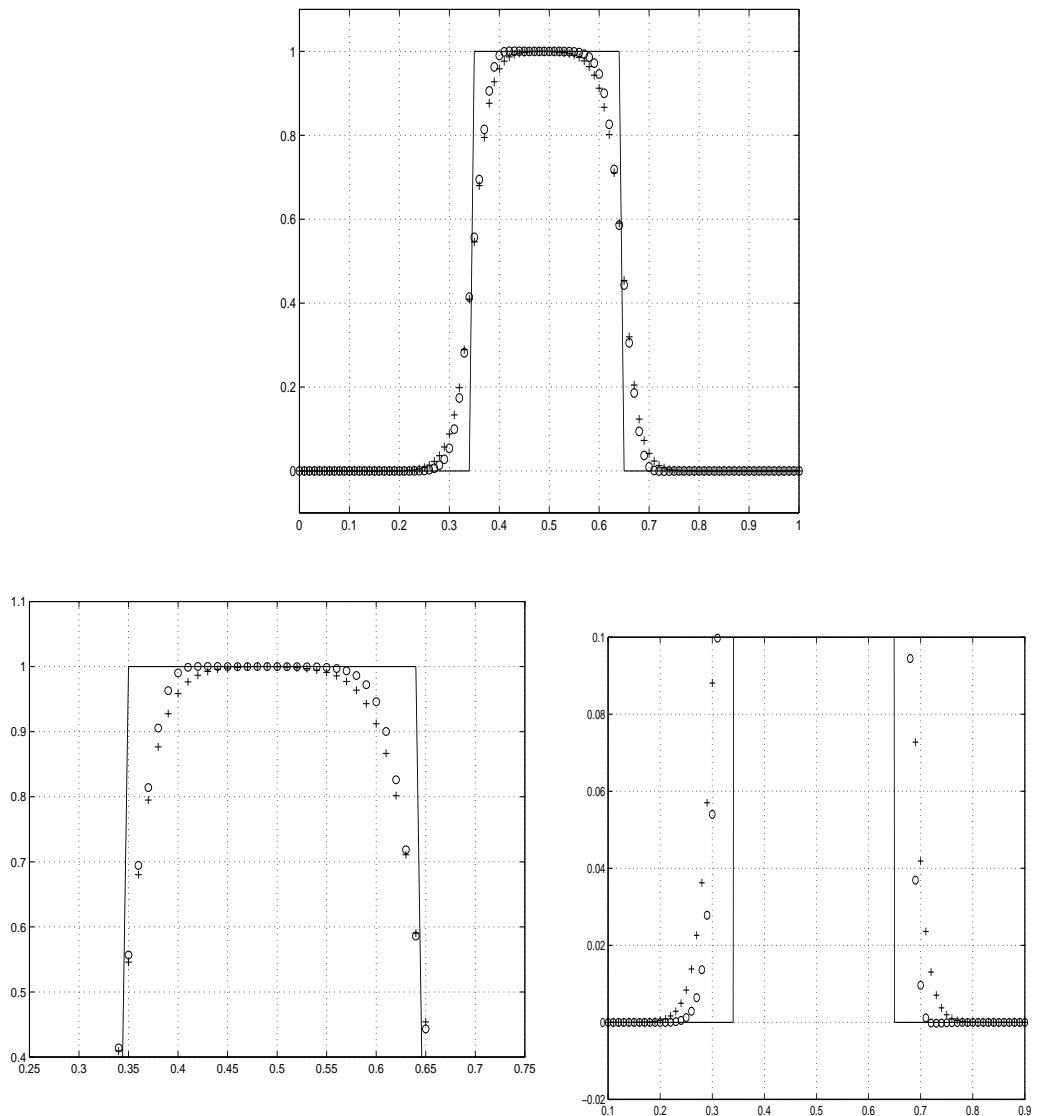


Figure 5.6: Comparison of the numerical solution of linear advection of Example 1 for ENO3 "+" and PowerENO3 "o"

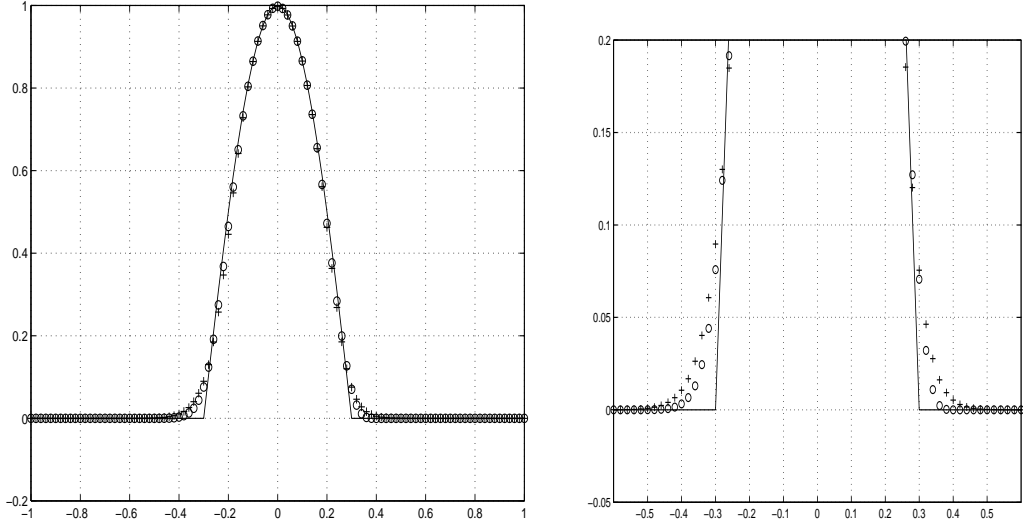


Figure 5.7: Comparison of the numerical solution of linear advection of Example 2 for ENO3 "+" and PowerENO3 "o"

method. The same calculations were done for Example 2, and we observe in Figure 5.7 better resolution of corners for our PowerENO3 method.

The above experiments show that the influence of the end points of the stencil is weaker for our PowerENO3 method thanks to the effect of the limiter.

In Figure 5.8 we display the numerical approximation of Example 1 using WENO5 and WPowerENO5 methods represented with '+' and 'o' signs, respectively. We observe the better behavior of our WPowerENO5 near discontinuities. The same calculation was done for the Example 2 using both fifth order accurate reconstruction procedures as displayed in Figure 5.9. In this case, the better behavior is justified for two reasons, namely: the narrower band of degeneration of accuracy for our method, (see Figures 4.1 and 4.2), and the better behavior

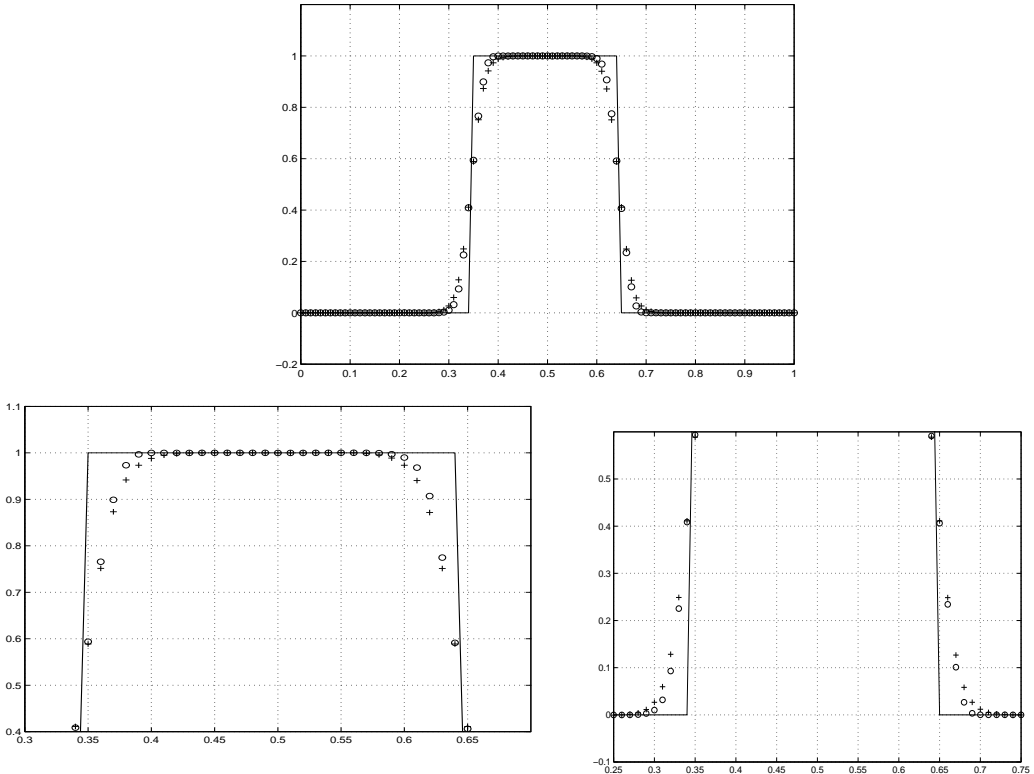


Figure 5.8: Comparison of the numerical solution of linear advection. Example 1 for WENO5 "+" , WPowerENO5 "o"

near discontinuities inherited from the same feature observed for our PowerENO3 method.

Next, we perform numerical tests with Euler equations of gas dynamics.

5.5.3 Euler equations: One dimensional experiments

We start with two well-known Riemann problems:

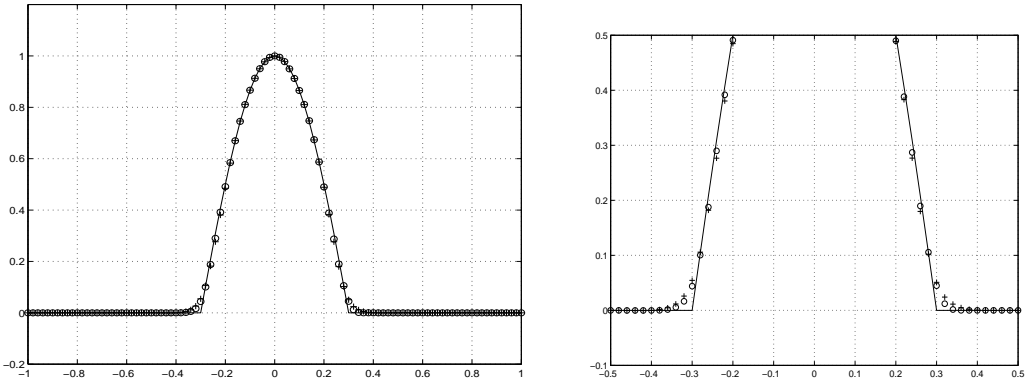


Figure 5.9: *Comparison of the numerical solution of linear advection of Example 2 for WENO5 "+" , WPowerENO5 "o"*

5.5.3.1 Riemann problem: Sod's Tube

This problem introduced in [38] is a Riemann problem whose solution consists of a left rarefaction wave, a contact discontinuity and a right shock wave. The initial data for this problem are,

$$u_0(x) = \begin{cases} (\rho_L, v_L, P_L) = (1, 1, 1) & -5 \leq x < 0 \\ (\rho_R, v_R, P_R) = (0.125, 0, 0.1) & 0 \leq x \leq 5 \end{cases}$$

5.5.3.2 Riemann problem: Lax's Tube

This problem introduced in [15] is a classical blast wave consisting in two initial states, the right one is a gas at rest and the left one is a high pressured gas moving to the right. The same structure as in Sod's tube appears but the gas between the contact and the shock wave is more compressed reaching a density higher than the one at the left of the contact wave. Thus this test is more severe than the Sod's tube. The initial data for this problem are,

$$u_0(x) = \begin{cases} (\rho_L, v_L, P_L) = (0.445, 0.698, 3.528) & -5 \leq x < 0 \\ (\rho_R, v_R, P_R) = (0.5, 0, 0.571) & 0 \leq x \leq 5 \end{cases}$$

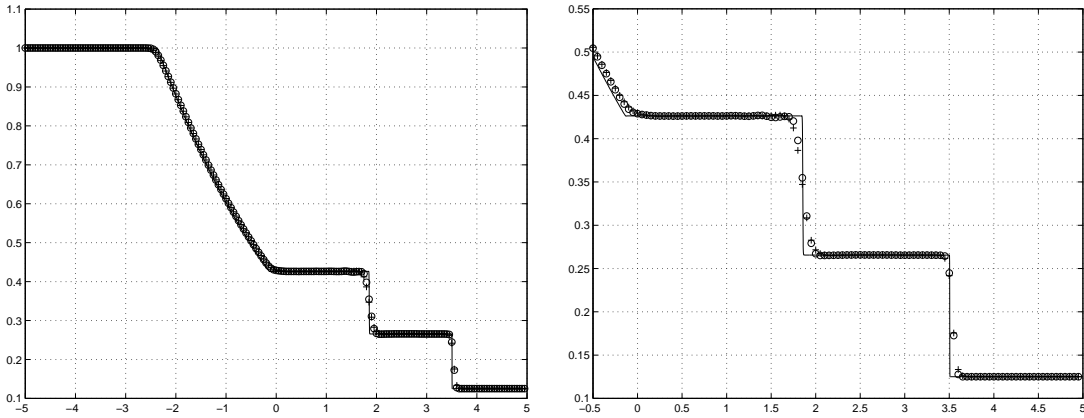


Figure 5.10: Numerical solution of the density profile for the Sod's Tube for WENO5-MFF "+" and WPowerENO5-MFF "o"

The computations for both cases were done using 200 equal spaced grid points with a constant ratio $\Delta t/h = 0.2$ until time 2 for the Sod's Tube and $\Delta t/h = 0.1$ until time 1.3 for the Lax's Tube. The solid lines represent the exact solution evaluated in 5000 points, see ([37]) .

In Figures 5.10 and 5.11 we display the numerical results of the density profile. The better behavior near discontinuities for our WPowerENO5 method is more conspicuous for the Lax's Tube experiment, (see zoomed regions at the bottom of Figure 5.11).

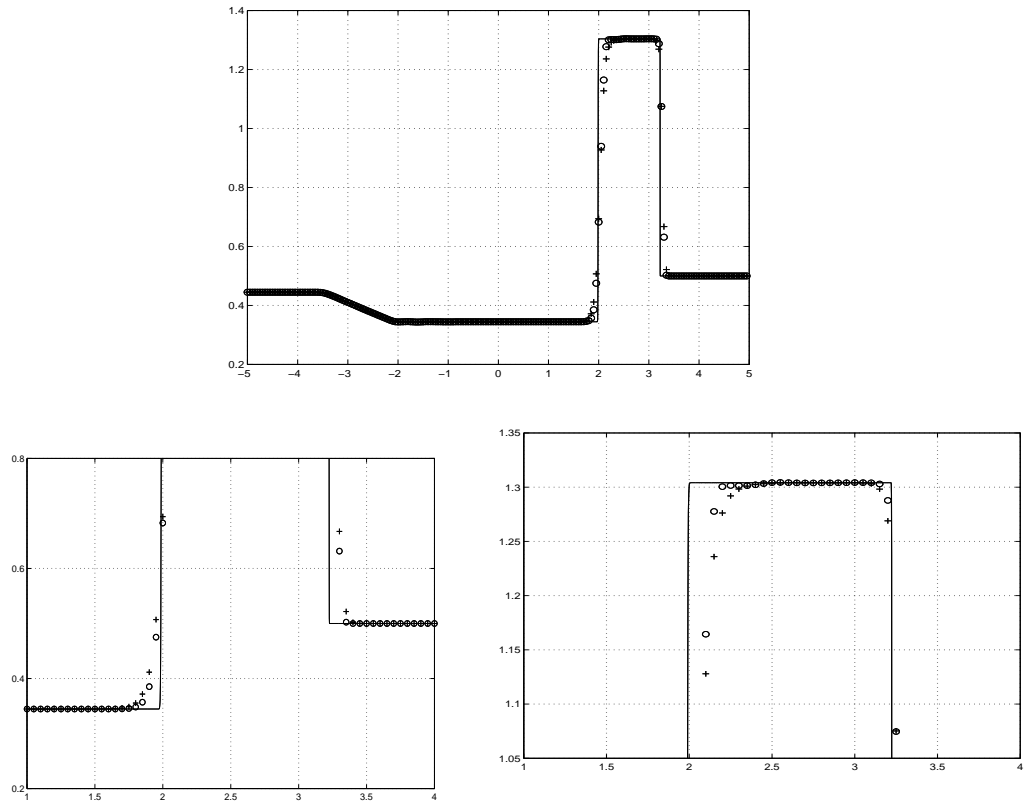


Figure 5.11: Numerical solution of the density profile for the Lax's Tube for WENO5-MFF "+" , WPowerENO5-MFF "o". Bottom, zoomed regions

5.5.3.3 Shock Entropy Wave Interaction

We consider a model that involves a moving Mach 3 shock interacting with sine waves in density. This model was used as a benchmark in Shu-Osher, ([36]).

The initial data for this problem are,

$$u_0(x) = \begin{cases} (\rho_L, v_L, P_L) = (3.85714, 2.62936, 10.33333) & -5 \leq x < -4 \\ (\rho_R, v_R, P_R) = (1 + 0.2 \sin(5x), 0, 1) & -4 \leq x \leq 5 \end{cases}$$

The numerical results of the density profile are displayed in Figure 5.12. Solid line correspond to the numerical solution by WENO5 with 1600 points, that can be seen as the “exact” solution. We compute the numerical approximation for 400 points at time=1.8 and $\Delta t/h = 0.1$ for WENO5 and WPowerENO5, represented by '+' and 'o' signs, respectively. We observe in Figure 5.12 that fine structure in the density profile makes our WPowerENO5 method to perform better than the WENO5 one. This feature is a consequence of the fact that the WPowerENO5 method is more compressive, (it produces more total variation in cell), than WENO5 method. On the other hand, we observe again a reduced smearing near shocks, (see zoomed regions at the bottom of Figure 5.12).

5.5.3.4 Two Interacting Blast Waves

This is a very severe test originally proposed as a benchmark by Woodward and Colella ([41]). The initial data consists of two strong blast waves propagating in opposite directions and hitting each other. The density profile contains rarefaction waves, contact waves and shocks interacting. The difficult features to resolve in this case are the local maxima and the reduction of the smearing at the contacts.

Reflective boundary conditions are applied at $x = 0$ and $x = 1$. We consider the initial data:

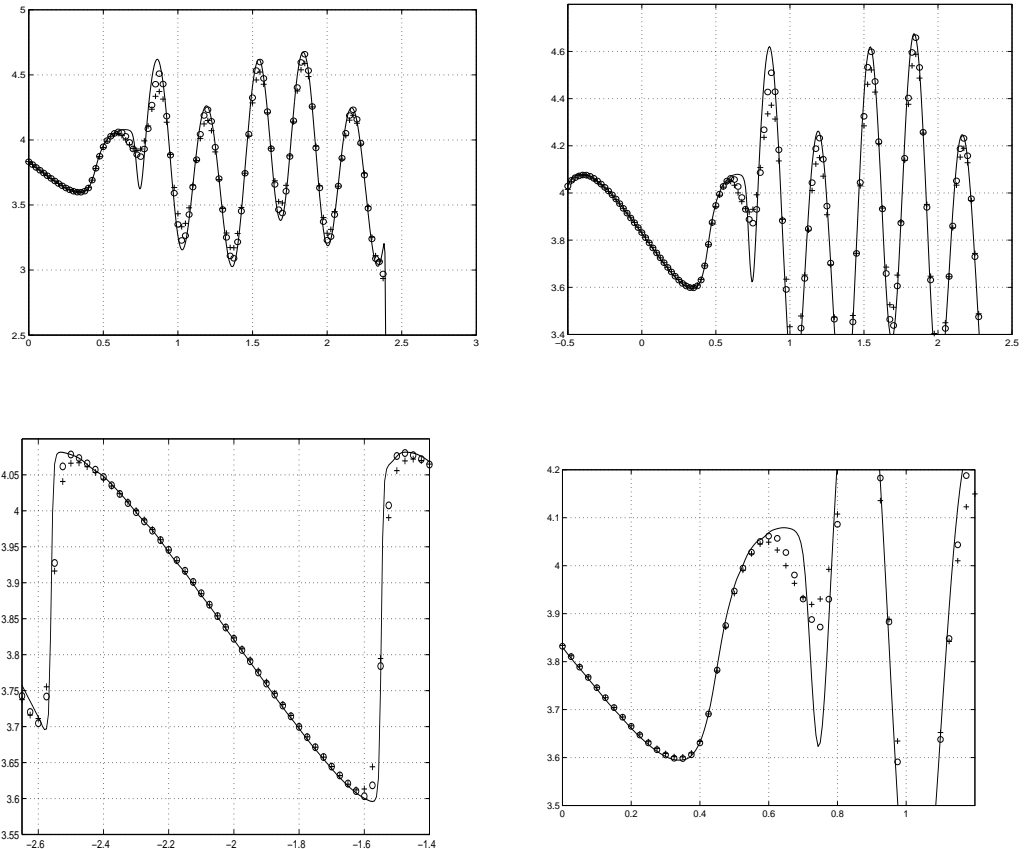


Figure 5.12: Numerical solution of the density profile of the Shock entropy wave interaction for WENO5 "+" and WPowerENO5 "o". Zoomed regions.

$$u_0(x) = \begin{cases} (\rho_L, v_L, P_L) = (1, 0, 10^3) & 0 \leq x < 0.1 \\ (\rho_M, v_M, P_M) = (1, 0, 10^{-2}) & 0.1 \leq x < 0.9 \\ (\rho_R, v_R, P_R) = (1, 0, 10^2) & 0.9 \leq x \leq 1 \end{cases}$$

We display in Figure 5.13 the density component computed with 400 and 800 grid points (top and bottom, respectively). We evolved until time 0.038 with $\Delta t/h = 0.01$ for WENO5, (left), and WPowerENO5, (right).

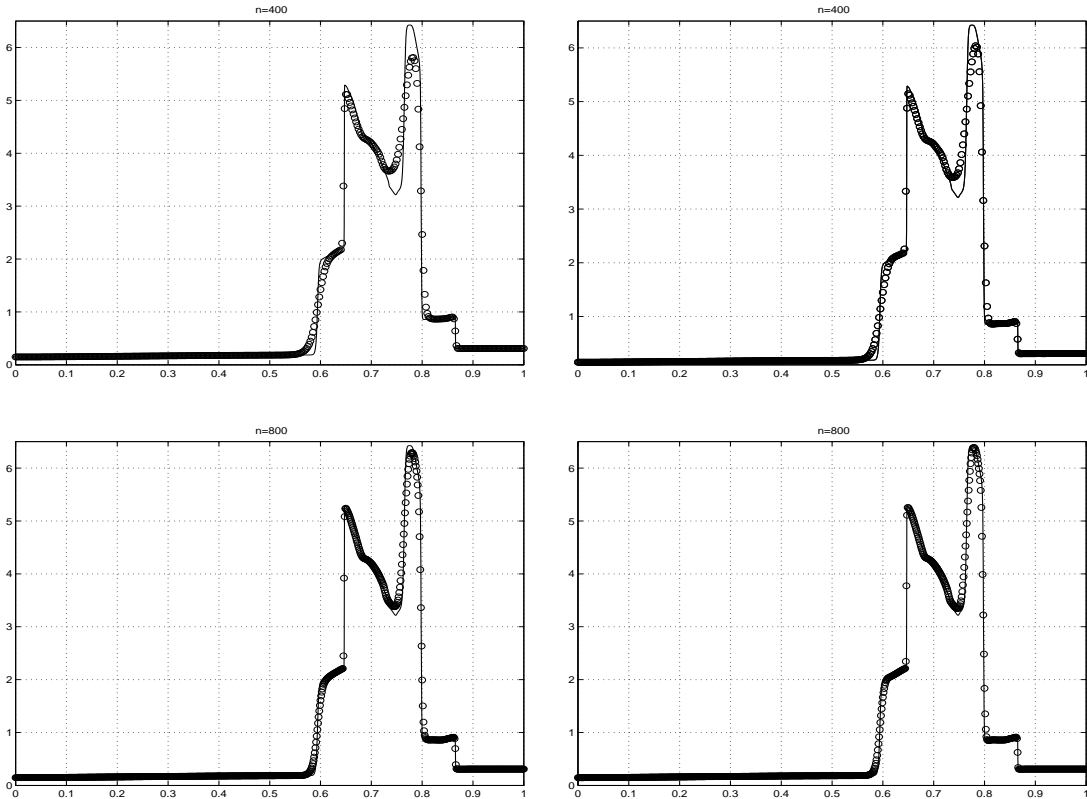


Figure 5.13: Numerical solution of the density profile of the Two interacting blast waves for: WENO5 left pictures with 400 and 800 points and WPowerENO5 right pictures with 400 and 800 points

We observe that the local extrema are better resolved for our WPowerENO5 method. We did computations with different number of grid points and we observe good convergence rate to the “exact” solution, (computed by WENO5 with 2000 points).

Finally, we will present three numerical experiments for the two-dimensional Euler equations for gas dynamics.

5.5.4 Euler equations: Two-dimensional Riemann Problems

A two-dimensional Riemann problem consists in an initial data defined as constants states on each of the four quadrants.

5.5.4.1 Four contacts problem

We consider the four contacts Riemann problem defined in [32] consisting in two colliding shock waves generated at the origin that propagate outwards following the way left by the contacts. The flow becomes Kelvin-Helmholtz unstable through the contacts.

The initial data for this problem are,

First quadrant, $([0.5, 1] \times [0.5, 1])$, $(\rho, u, v, P) = (1, 0.75, -0.5, 1)$.

Second quadrant, $([0, 0.5] \times [0.5, 1])$, $(\rho, u, v, P) = (2, 0.75, 0.5, 1)$.

Third quadrant, $([0, 0.5] \times [0, 0.5])$, $(\rho, u, v, P) = (1, -0.75, 0.5, 1)$.

Fourth quadrant, $([0.5, 1] \times [0, 0.5])$, $(\rho, u, v, P) = (3, -0.75, -0.5, 1)$.

We evolve the initial data until time 1.6 with a CFL factor of 0.8 for a grid of 400x400 points for WENO5 and WPowerENO5 methods. We observe a better resolved vortex at the top with sharp contact waves for our WPowerENO5 method at Figure 5.14.

Also, we displayed at Figure 5.15 a x -section, that traverses the vortex, showing the better resolution of the contact discontinuities of our WPowerENO5 method versus WENO5 method, (see the fine structure of the vortex region at

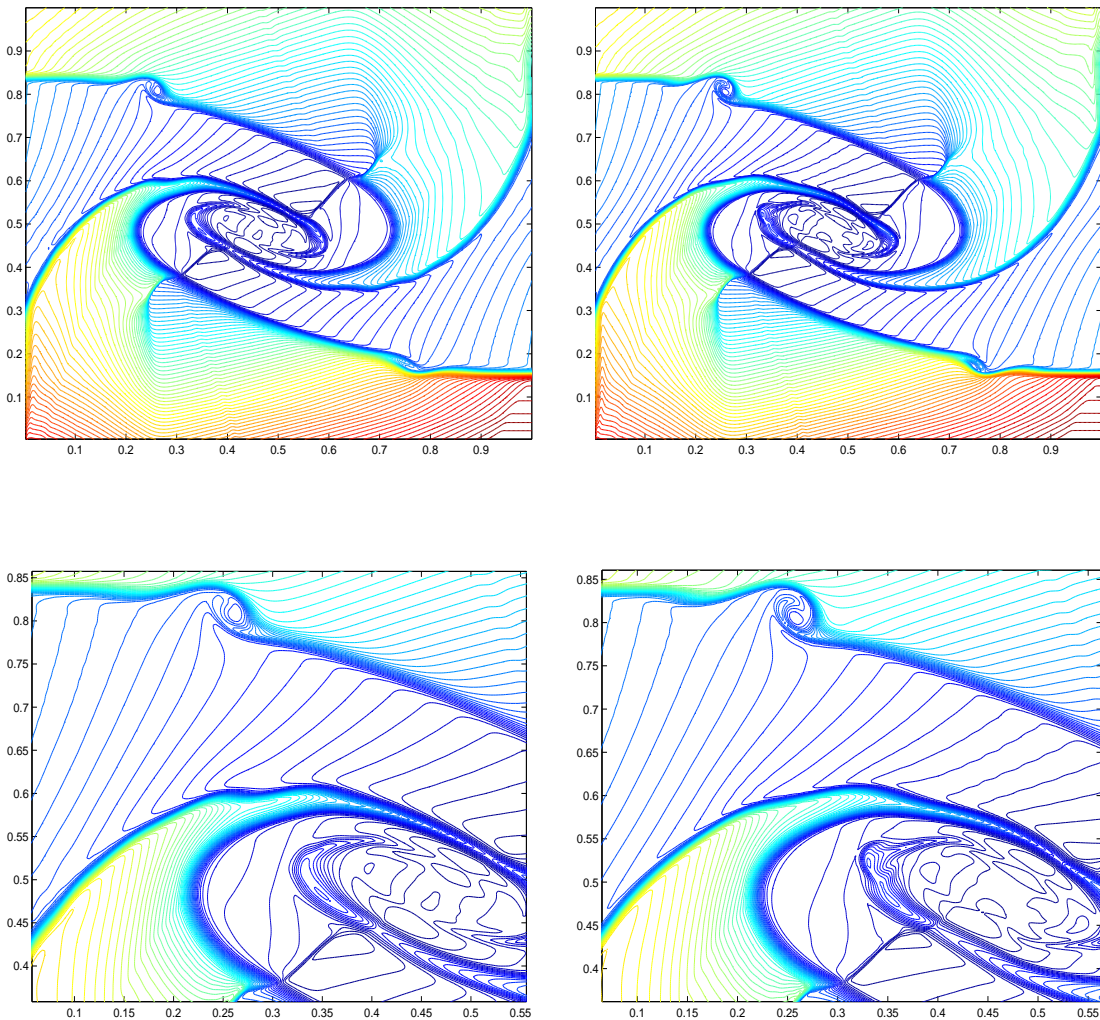


Figure 5.14: Top: Density profile of the Four contacts problem for WENO5 (left), WPowerENO5 (right). Bottom: Zoomed vortex regions.

the bottom of the figure).

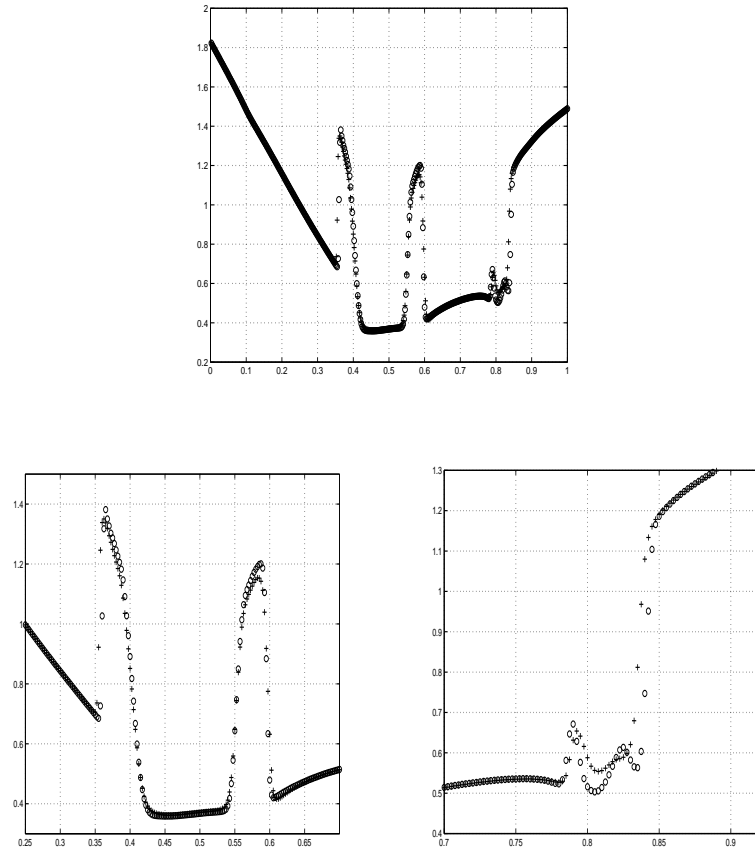


Figure 5.15: Top, section of density profile at $x = 0.2575$. Bottom, zoomed regions of the x-section. WENO5 "+" , WPowerENO5 "o"

5.5.4.2 Four shocks problem

We consider the Riemann problem corresponding to Configuration 3 defined in [32] in the domain $[0, 1] \times [0, 1]$ localizing the contact point at $(0.75, 0.75)$ instead of the center of the square.

The initial data read as:

First quadrant, $([0.75, 1] \times [0.75, 1])$, $(\rho, u, v, P) = (1.5, 0, 0, 1.5)$.

Second quadrant, $([0, 0.75] \times [0.75, 1])$, $(\rho, u, v, P) = (0.5323, 1.206, 0, 0.3)$.

Third quadrant, $([0, 0.75] \times [0, 0.75])$, $(\rho, u, v, P) = (0.138, 1.206, 1.206, 0.029)$.

Fourth quadrant, $([0.75, 1] \times [0, 0.75])$, $(\rho, u, v, P) = (0.5323, 0, 1.206, 0.3)$.

We evolve in time until 0.8 with a CFL factor of 0.8 and a grid of 400x400 points. In Figure 5.16 we display the approximations of the density contour profile obtained with the WENO-MFF and Weighted PowerENO-MFF schemes.

We observe in Figure 5.16 the better resolution of the unstable contact discontinuities and the jet structure appearing at the top right region for our WPow-erENO5 method versus WENO5 method.

5.5.5 Euler equations: Two dimensional Mach 3 Wind Tunnel with a Step

This test problem, introduced by Emery [6], has been carefully analyzed in [41] and [4]. The problem is initialized by a uniform Mach 3 flow in a tunnel containing a step. The tunnel is 1 length unit wide and 3 length units long. The step is 0.2 length units high and is located 0.6 units from the left-hand end of the tunnel.

Inflow boundary conditions are applied at the left-hand end and outflow boundary conditions are applied at the right-hand end of the computational domain. Reflective boundary conditions are applied along the walls of the tunnel.

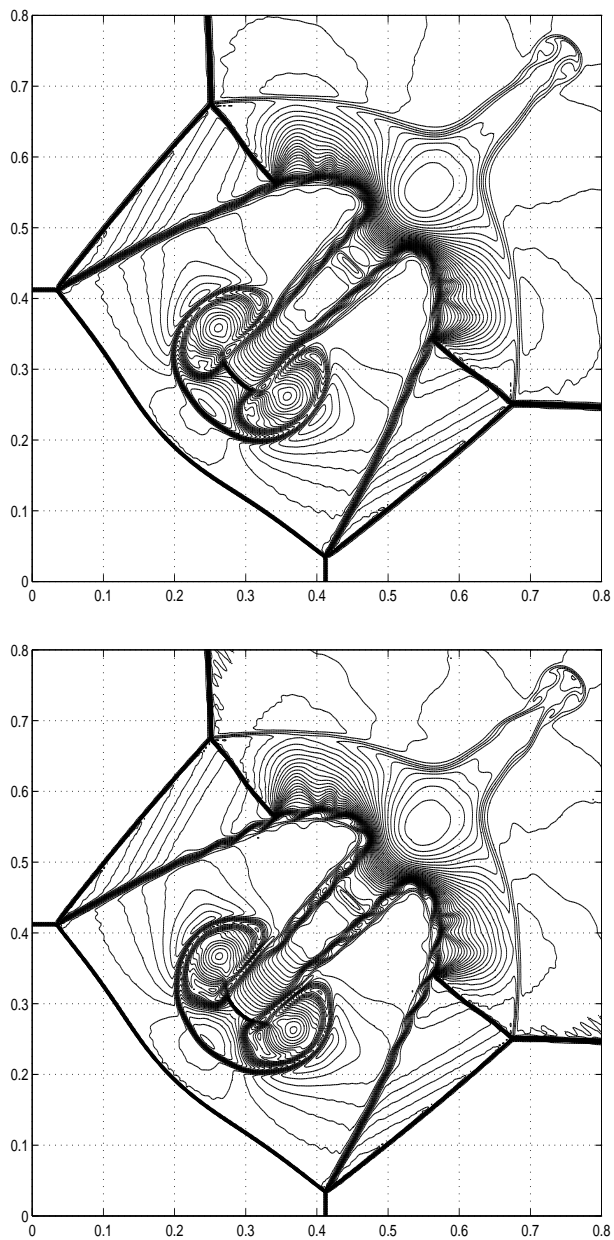


Figure 5.16: Zoomed region of the density profile for the Four shocks problem:
WENO5 (Top), WPowerENO5 (Bottom)

Since the corner of the step is a singular point of the boundary, we perform an entropy and an enthalpy correction near the corner of the step in order to avoid the unphysical behavior of the flow in this region. The correction follows the prescription described in [4], (see [7] for more details on the isobaric fix correction applied on reflective boundaries to reduce the overheating effect).

Initially the tunnel is filled with a gamma-law gas with $\gamma = 1.4$, which everywhere has density 1.4, pressure 1.0 and velocity 3.

This is a difficult test involving strong reflective shock waves.

We use this example to test the robustness of our method in presence of reflective boundary conditions.

We evolve the initial data until time 4 for a grid of 240x80 grid points with a CFL factor of 0.8 . We display the contour lines of the density profiles in Figure 5.17 and the adiabatic constant profiles in Figure 5.18. We observe good resolution and location of the strong reflective waves appearing in this test, and we have slightly better resolution at the contact line for our scheme.

In Figure 5.19 we display sections of the density component. The left picture is the x-section at $x = 0.8$, where we observe better resolution of the weak contact for our WPowerENO5 method.

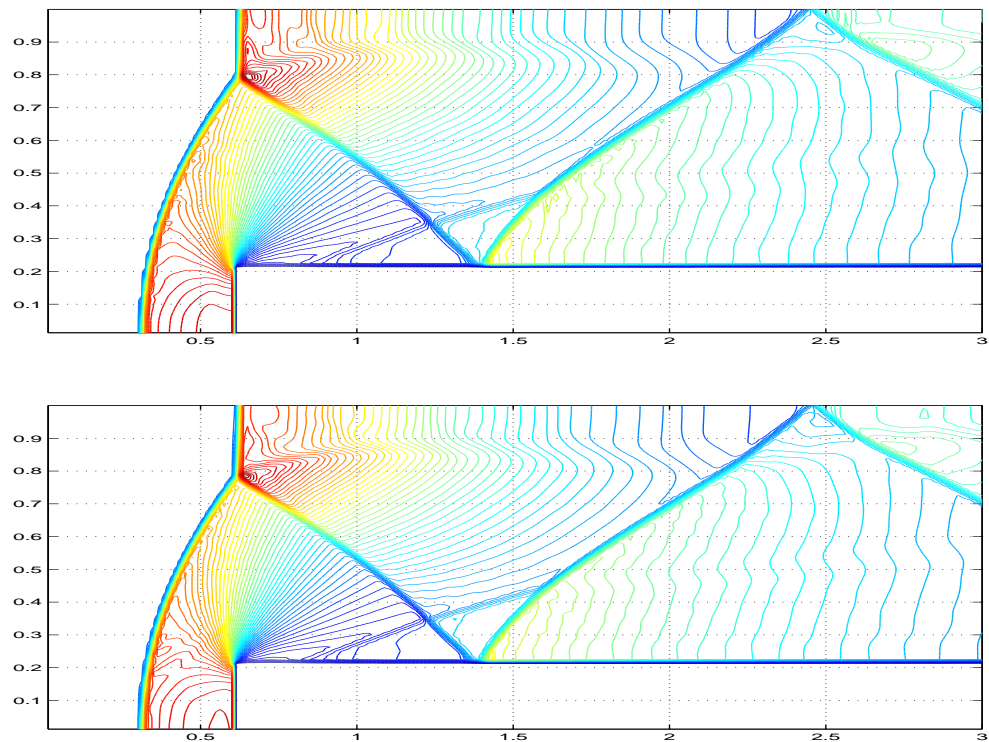


Figure 5.17: Density profile, WENO5 (top), WPowerENO5 (bottom)

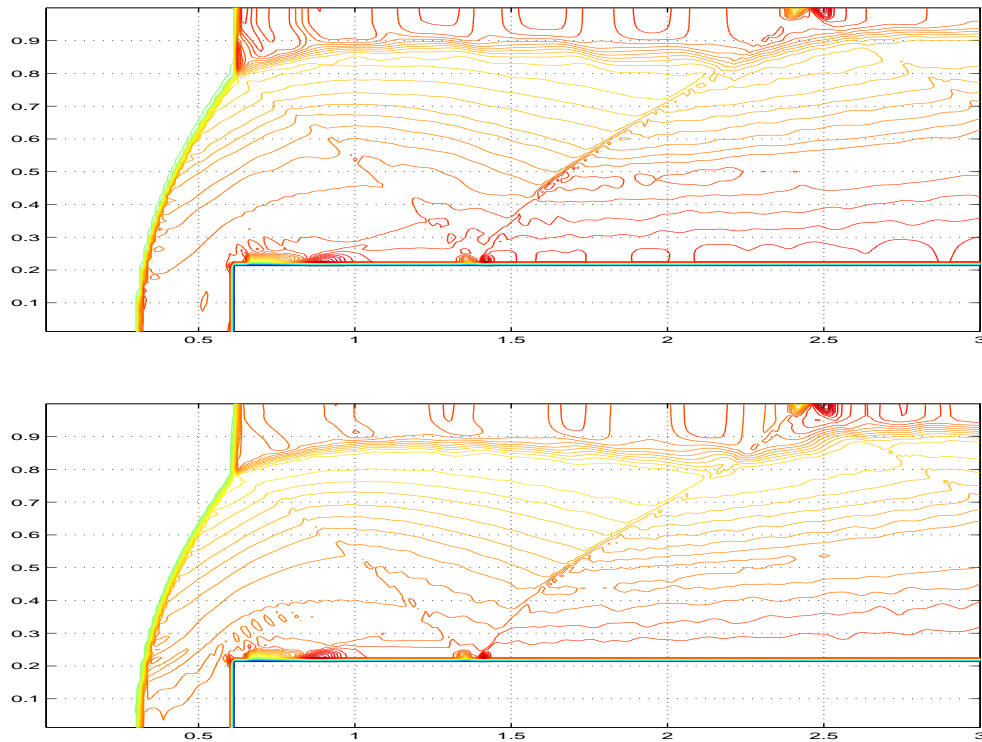


Figure 5.18: Adiabatic constant P/ρ^γ , WENO5 (top), WPowerENO5 (bottom)

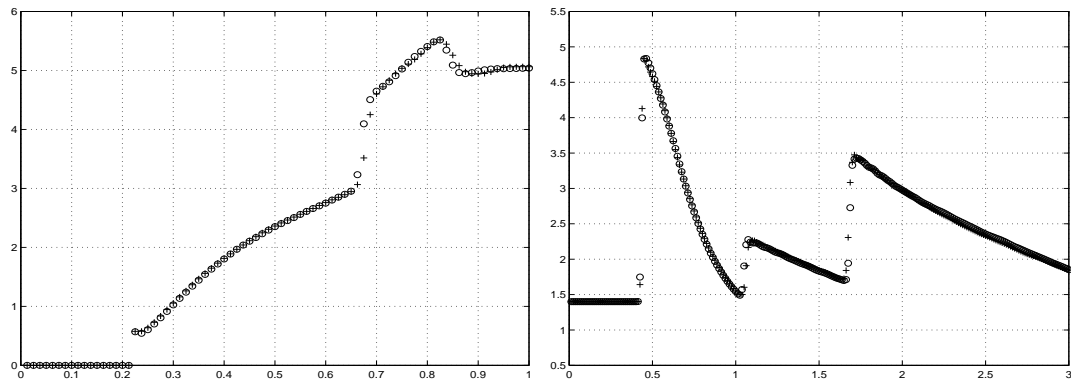


Figure 5.19: Sections of density profile at $x = 0.8$ (left) and $y = 0.5$ (right),
WENO5 '+' , WPowerENO5 'o'

CHAPTER 6

Applications: Numerical simulations of Rayleigh-Taylor and Richtmyer-Meshkov Instabilities

6.1 Introduction

When a shock wave encounters a fluid discontinuity between two different gases, small perturbations at the interface can grow into nonlinear structures having the form of “bubbles” and “spikes”.

The Richtmyer-Meshkov (RM) instability ([28] and [24]) is closely related to the Rayleigh-Taylor (RT) instability, ([25],[42], [34]), but they are qualitatively different. In the Rayleigh-Taylor instability a persistent acceleration (gravity field) causes the perturbation to grow exponentially in time, whereas in the RM instability the shock acceleration is impulsive and causes the amplitude to grow linearly in time at the beginning and grow logarithmically in the large. Moreover, a RT instability can occur only if light fluid is accelerated into heavy fluid, but a RM instability can work in either direction of the acceleration. It is known that vanishing viscosity solutions to problems involving RM instabilities might

not exist, but we can obtain high-order accurate approximations with a resulting numerical viscosity (Reynolds number) for which the compressible turbulent regime is completely developed.

In this Chapter we present two sets of numerical experiments addressing Rayleigh-Taylor and Richtmyer-Meshkov instabilities, respectively, by means of the proposed high order accurate capturing schemes in order to check the robustness, stability and the capability of the numerical schemes in resolving fine scales near unstable interfaces.

6.2 Rayleigh-Taylor instability

We model the Rayleigh-Taylor instability by means of the two-dimensional Euler equations (section 5.3) evolving an initial perturbed interface separating two states of a fluid, light and heavy, (see for example [42] and [34]).

The gravity field is introduced in the source terms: ρ is added to the right-hand side of the third equation and ρv is added to the fourth equation of Euler equations. When evolving in time the unstable regime at the interface is excited through the acceleration of gravity.

The initial data in the computational domain, $[0, 0.25] \times [0, 1]$,

$$(\rho, u, v, P) = \begin{cases} (2, 0, -0.25 \cdot c \cdot \cos(8\pi x), 2y + 1) & 0 \leq y < 0.5 \\ (1, 0, -0.25 \cdot c \cdot \cos(8\pi x), y + 1.5) & 0.5 \leq y < 1 \end{cases}$$

where $c = \sqrt{\frac{\gamma P}{\rho}}$ is the sound speed. In this experiment we consider $\gamma = \frac{5}{3}$ and

evolve until time $t = 1.95$.

Reflective boundary conditions are imposed for the left and right boundaries.

At the top boundary, ($y = 1$), the flow values are set as

$$(\rho, u, v, P) = (1, 0, 0, 2.5)$$

and at the bottom boundary, ($y = 0$), they are

$$(\rho, u, v, P) = (2, 0, 0, 1)$$

Both experiments have been implemented using a grid of 200×800 points and a CFL factor of 0.6.

In Figure 6.1 we observe much better resolution for the Weighted PowerENO method in the complicated solution structure than WENO method. In particular the Kelvin-Helmholtz vortex structure appearing in the evolution is better resolved for the Weighted PowerENO method.

6.3 Richtmyer-Meshkov instability

We model the Richtmyer-Meshkov instability by using the Euler equations for multicomponent gas dynamics. The unstable regime is induced by a shock wave hitting a perturbed interface between two gases with different adiabatic exponents.

We use the multicomponent compressible Euler equations as the analytical model where we have conservation of total mass, momentum and energy and we add the conservation of the first component, being the conservation of the second

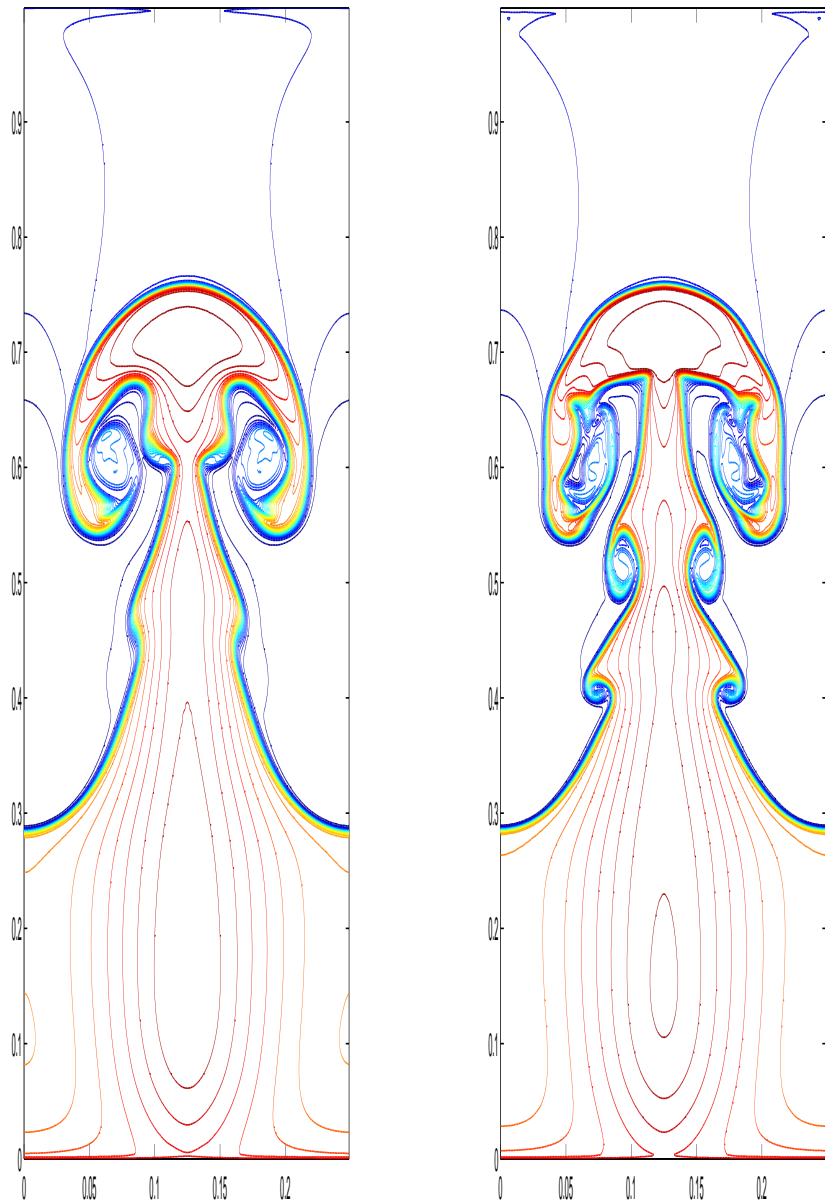


Figure 6.1: Comparison of the numerical solution of the Rayleigh-Taylor instability for MFF-WENO5 (left) and MFF-Weighted PowerENO (right).

one a consequence.

6.3.1 Model equations

We consider interfaces between two ideal gases. Let ρ be the density of the mixture, ϕ the mass fraction of the first component and $1 - \phi$ the mass fraction of the second component. We assume that both components are in thermodynamical equilibrium with specific heats at constant pressure C_{p_1} , C_{p_2} , specific heats at constant volume C_{v_1} , C_{v_2} and adiabatic exponents γ_1 , γ_2 respectively.

Using thermodynamic arguments [22], the adiabatic exponent of the mixture of gases is

$$\gamma(\phi) = \frac{C_p}{C_v} = \frac{C_{p_1}(1 - \phi) + C_{p_2}\phi}{C_{v_1}(1 - \phi) + C_{v_2}\phi} \quad (6.1)$$

according to Dalton's law.

The equation of state (EOS) for the mixture is an ideal gas equation of state of the form:

$$P(\rho, \epsilon, \phi) = (\gamma(\phi) - 1)\rho\epsilon \quad (6.2)$$

This means that at every point of the flow there is a thermodynamical equilibrium defined by the EOS.

The Euler equations for two component fluid flow are,

$$U_t + F(U)_x + G(U)_y = 0, \quad (6.3)$$

where,

$$U = \begin{bmatrix} \rho \\ \rho u \\ \rho v \\ E \\ \rho\phi \end{bmatrix} \quad F(U) = \begin{bmatrix} \rho u \\ \rho u^2 + P \\ \rho uv \\ (E + P)u \\ \rho\phi u \end{bmatrix} \quad G(U) = \begin{bmatrix} \rho v \\ \rho uv \\ \rho v^2 + P \\ (E + P)v \\ \rho\phi v \end{bmatrix}$$

being ϕ the mass fraction considering $\phi = 0$ for fluid 1 and $\phi = 1$ for fluid 2.

In order to implement the characteristic based shock capturing schemes, we need the characteristic speeds and the complete spectral decomposition of the Jacobians.

The system is hyperbolic using the well-defined speed of sound where the eigenvalues of the Jacobian of the flux F in the x -direction are,

$$\lambda_1 = u - c_s, \quad \lambda_2 = u, \quad \lambda_3 = u, \quad \lambda_4 = u, \quad \lambda_5 = u + c_s \quad (6.4)$$

and the eigenvalues of the Jacobian of the flux G in the y -direction are

$$\mu_1 = v - c_s, \quad \mu_2 = v, \quad \mu_3 = v, \quad \mu_4 = v, \quad \mu_5 = v + c_s \quad (6.5)$$

where,

$$c_s = \sqrt{\frac{\gamma(\phi)P}{\rho}}$$

is the sound speed.

The Jacobians have a complete set of eigenvectors. The right eigenvectors

$$R^F = \begin{bmatrix} r_1 & r_2 & r_3 & r_4 & r_5 \end{bmatrix}$$

$$= \begin{bmatrix} 1 & 1 & 0 & 0 & 1 \\ u - c_s & u & 0 & 0 & u + c_s \\ v & v & 1 & 0 & v \\ H - uc_s & \frac{u^2+v^2}{2} & v & -\frac{X}{\gamma-1} & H + uc_s \\ \phi & \phi & 0 & 1 & \phi \end{bmatrix}$$

and the left eigenvectors

$$L^F = \begin{bmatrix} l_1 \\ l_2 \\ l_3 \\ l_4 \\ l_5 \end{bmatrix} = \begin{bmatrix} b_2 + \frac{u}{2c_s} - \phi b_3 & -b_1 u - \frac{1}{2c_s} & -b_1 v & b_1 & b_3 \\ 1 - 2b_2 + 2\phi b_3 & 2ub_1 & 2vb_1 & -2b_1 & -2b_3 \\ -v & 0 & 1 & 0 & 0 \\ -\phi & 0 & 0 & 0 & 1 \\ b_2 - \frac{u}{2c_s} - \phi b_3 & -b_1 u + \frac{1}{2c_s} & -b_1 v & b_1 & b_3 \end{bmatrix}$$

where

$$H = \frac{E + P}{\rho} = \frac{c_s^2}{\gamma(\phi) - 1} + \frac{1}{2}(u^2 + v^2)$$

is the total enthalpy per unit volume and X , b_1 , b_2 and b_3 are defined as:

$$X = \gamma'(\phi)\epsilon,$$

$$b_1 = \frac{\gamma(\phi) - 1}{2c_s^2}, \quad b_2 = b_1 \left(\frac{u^2 + v^2}{2} \right), \quad b_3 = \frac{b_1 X}{\gamma - 1}$$

The eigenvectors of the Jacobian in the y -direction are obtained by changing the roles of u and v and the second and third components of each left and right eigenvector.

6.3.2 One dimensional model problems

We perform two experiments consisting in a simple shock wave in air with a shock Mach number 1.52 hitting a bubble of gas, Helium or R22, in mechanical and thermodynamical equilibrium with the surrounding air at rest.

The pressure P_b , density ρ_b and velocity v_b behind the shock wave are computed using the Rankine-Hugoniot conditions assuming the shock Mach number is 1.52.

6.3.2.1 Helium-Air

The initial data for the region ahead the shock, (air, $\phi = 0$), for the air at rest, ($\phi = 0$), and a Helium bubble ($\phi = 1$) are,

$$(\rho, u, P, \phi) = \begin{cases} (1, 0, 1, 0) & 0 \leq x \leq 0.16 \\ (0.189, 0, 1, 1) & 0.16 \leq x \leq 0.2 \\ (1, 0, 1, 0) & 0.2 \leq x \leq 0.22 \end{cases}$$

taking the corresponding values for the adiabatic exponents, $\gamma_{Air} = 1.4$ and $\gamma_{Helium} = 1.648$, and for the specific heats at constant pressure $C_{p_{Air}} = 0.72$ and $C_{p_{Helium}} = 2.44$.

6.3.2.2 R22-Air

The initial data for the region ahead the shock, (air, $\phi = 0$), for the air at rest, ($\phi = 0$), and a R22 bubble ($\phi = 1$) are,

$$(\rho, u, P, \phi) = \begin{cases} (1, 0, 1, 0) & 0 \leq x \leq 0.16 \\ (3.15, 0, 1, 1) & 0.16 \leq x \leq 0.2 \\ (1, 0, 1, 0) & 0.2 \leq x \leq 0.22 \end{cases}$$

taking the corresponding values for the adiabatic exponents, $\gamma_{Air} = 1.4$ and $\gamma_{R22} = 1.249$ and for the specific heats at constant pressure $C_{p_{Air}} = 0.72$ and $C_{p_{Helium}} = 0.365$

We use in both cases the Marquina Flux Formula together with the Weighted PowerENO5 scheme with a CFL factor of 0.8.

We evolve the Air-Helium initial data until time 0.7 and the Air-R22 data until time 0.13. We compute the approximate solution for two grid resolutions: 400 points and 3200 points. We display the numerical approximations of the density and pressure in Figures 6.2 and 6.3.

We observe at the zoomed regions of the pressure in both cases that the spikes in pressure at the bubble interfaces reduce for the finest grid. This shows that our method behaves stable and accurate for shock Mach numbers larger than the one used in [22].

6.3.3 Two-dimensional problems

We consider the interaction of a shock wave in air with shock Mach number 1.52 with a perturbed interface separating air at rest and Helium or R22.

The computational domain is $[0, 4] \times [0, 15]$ displayed in Figure 6.4. We consider the interface separating air from Helium or R22 defined by

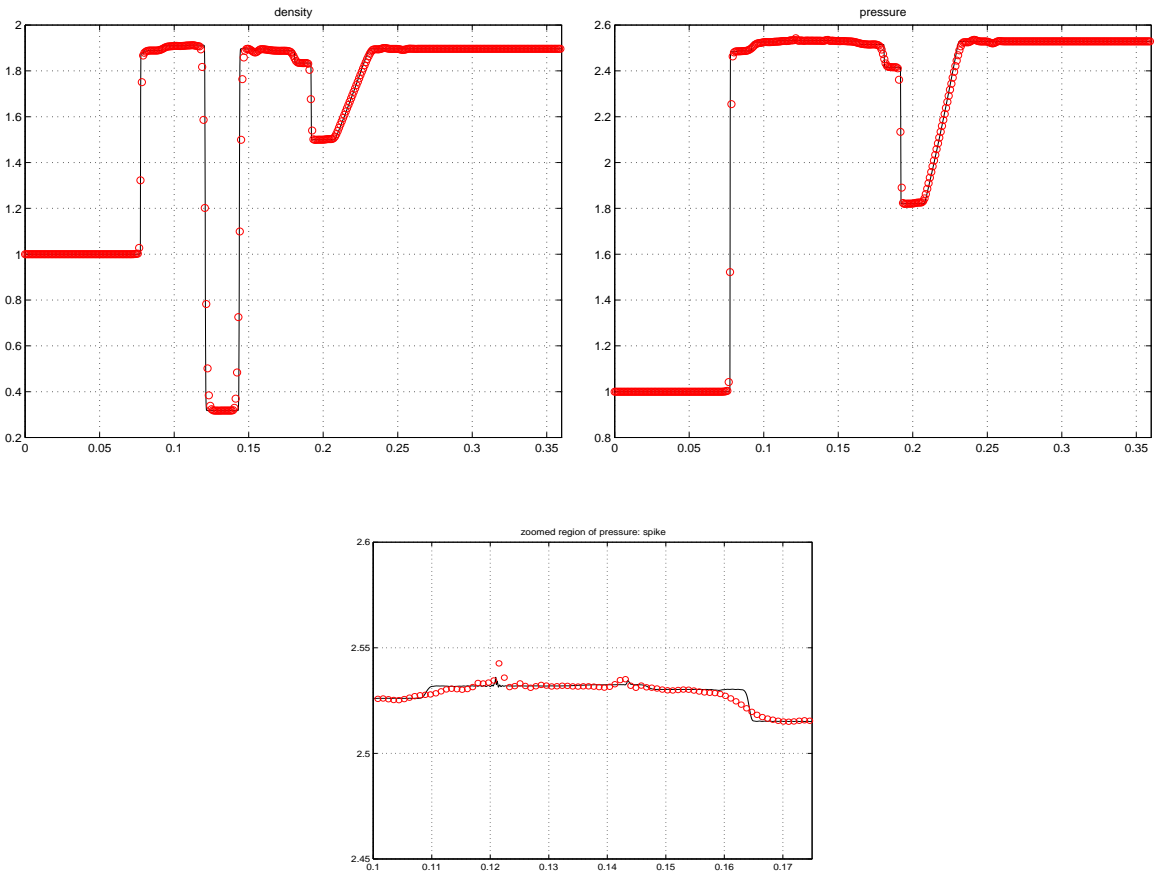


Figure 6.2: *Density and Pressure profiles of the Helium-Air case for Weighted PowerENO method. Bottom, zoom of the spike region of the pressure*

$$y = \text{curv}(x) = 12.8 + 0.6 \sin \left[\frac{\pi}{2}(x - 1) \right] \quad (6.6)$$

for $x \in [0, 4]$.

The initial data for the shocked air in $[0, 4] \times [13.95, 15]$ is computed using the Rankine-Hugoniot conditions for a shock Mach number of 1.52.

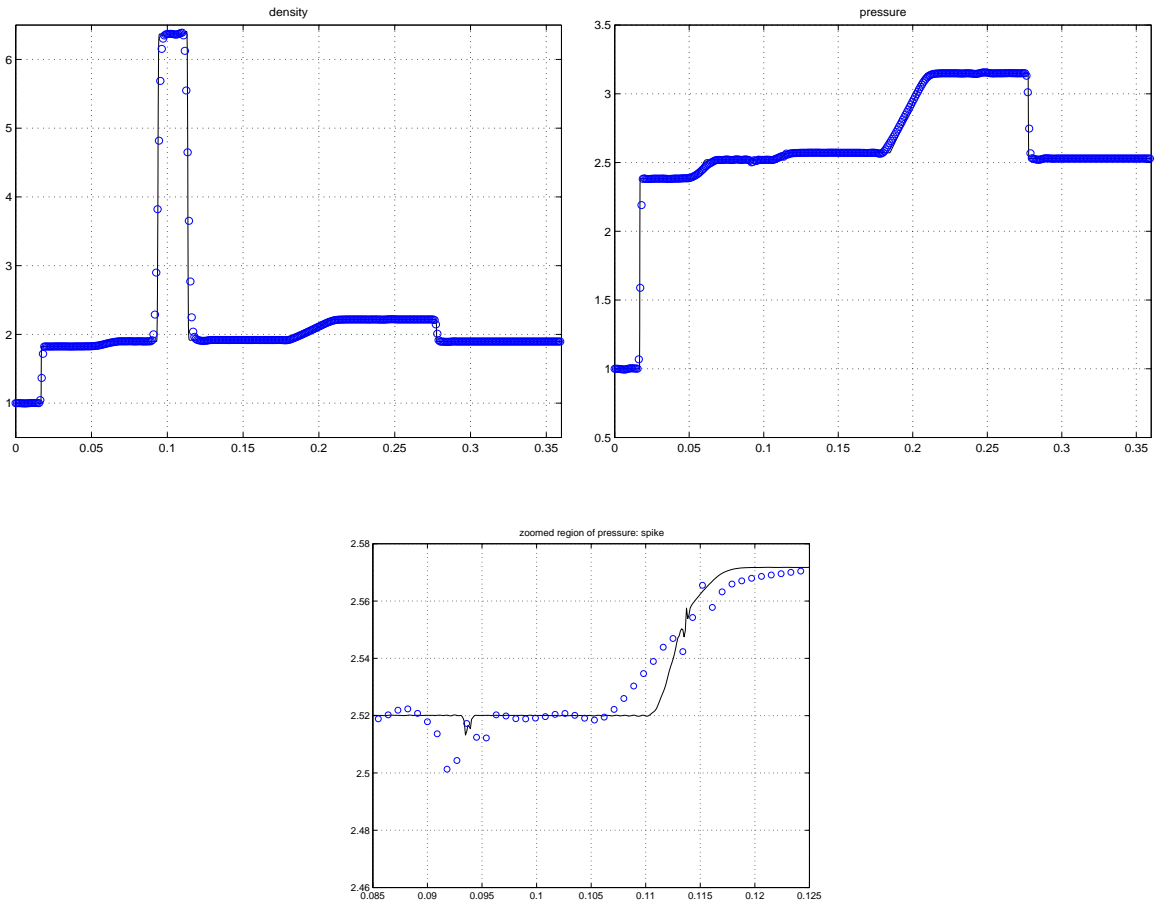


Figure 6.3: *Density and Pressure profiles of the R22-Air case for Weighted PowerENO method. Bottom, zoom of the spike region of the pressure*

The data for the air at rest region are, for $0 \leq x \leq 4$

$$(\rho, u, v, P, \phi) = (1, 0, 0, 1, 0) \quad \text{curv}(x) \leq y \leq 13.95 \quad (6.7)$$

The data for the Helium in mechanical and thermodynamical equilibrium with the air, for $0 \leq x \leq 4$, are

$$(\rho, u, v, P, \phi) = (0.1819, 0, 0, 1, 1) \quad 0 \leq y \leq \text{curv}(x) \quad (6.8)$$

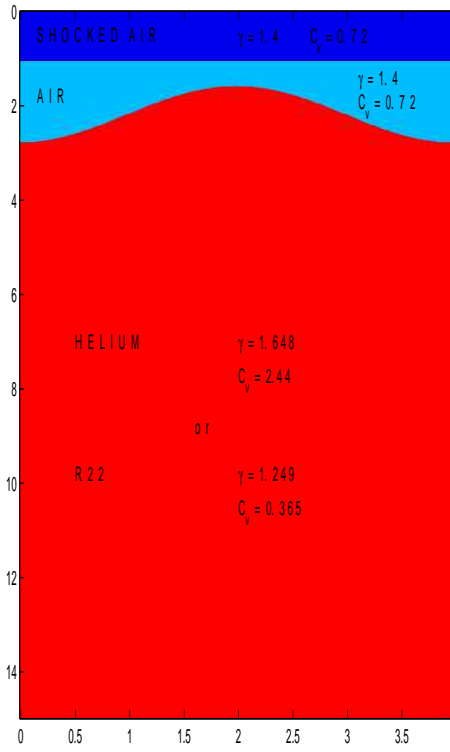


Figure 6.4: Two dimensional initial data for the Richtmyer-Meshkov instability

and for the R22,

$$(\rho, u, v, P, \phi) = (3.15, 0, 0, 1, 1) \quad 0 \leq y \leq \text{curv}(x) \quad (6.9)$$

$C_{p_{Air}} = 0.72$, $C_{p_{Helium}} = 0.365$ and $C_{p_{R22}} = 1.249$, $\gamma_{Air} = 1.4$, $\gamma_{Helium} = 1.648$ and $\gamma_{R22} = 1.249$. In our computation we use a grid of 200×750 and a CFL factor of 0.8. We evolve the Helium test until time 9 units and the R22 until time 17 units.

In Figure 6.5 we display eight snapshots of the density for the Air-Helium experiment using the MFF-Weighted PowerENO5 scheme for different intermediate times. We observe the process of the refracted (transmitted) shock wave

through the interface imparting differential vorticity along the interface. This velocity shear drives the penetration of the heavy fluid (air) into the light fluid (Helium). Analogous process is observed for the Air-R22 experiment computed with the MFF-Weighted PowerENO5 displayed in Figure 6.6 where the process works in the opposite direction since the heavy fluid is the R22 and the light fluid is the air.

In Figure 6.7 we display at time 9 the Air-Helium instability for the third order accurate MFF-PowerPHM scheme, and the fifth order accurate MFF-WENO5 and MFF-Weighted PowerENO5 schemes. We observe the better resolution of the vortex structure for the MFF-Weighted PowerENO5 scheme over the other two schemes.

Similar behavior is observed in Figure 6.8 for the Air-R22 instability at time 17.

We observe in the last two experiments that the resolution of the third order accurate PowerPHM is less accurate than the other two, which are fifth order accurate. This shows that to capture fine scales in unstable interfaces the spatial accuracy of the numerical scheme is also important.

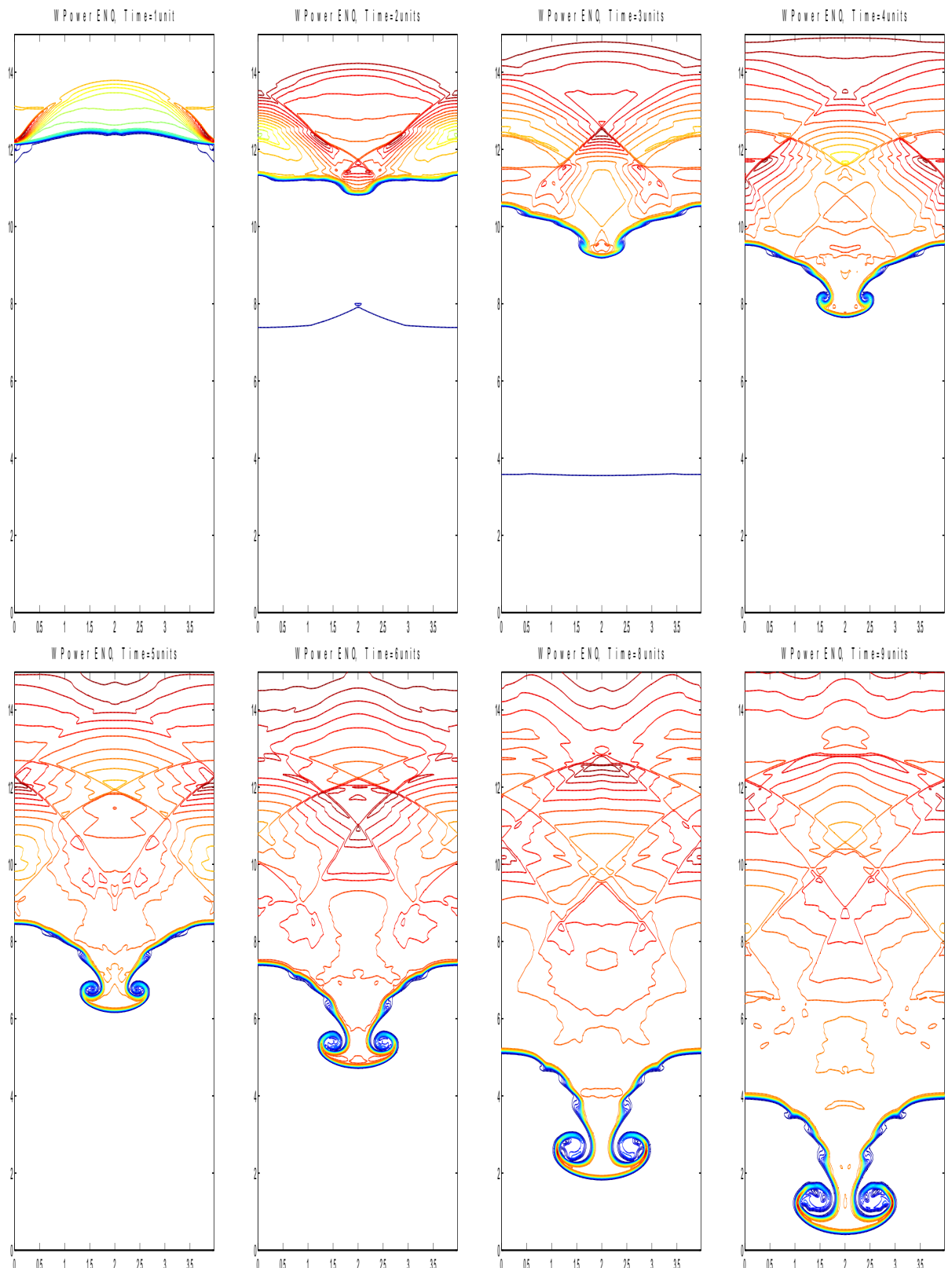


Figure 6.5: Snapshots of the Air-He Richtmyer-Meshkov instability evolution

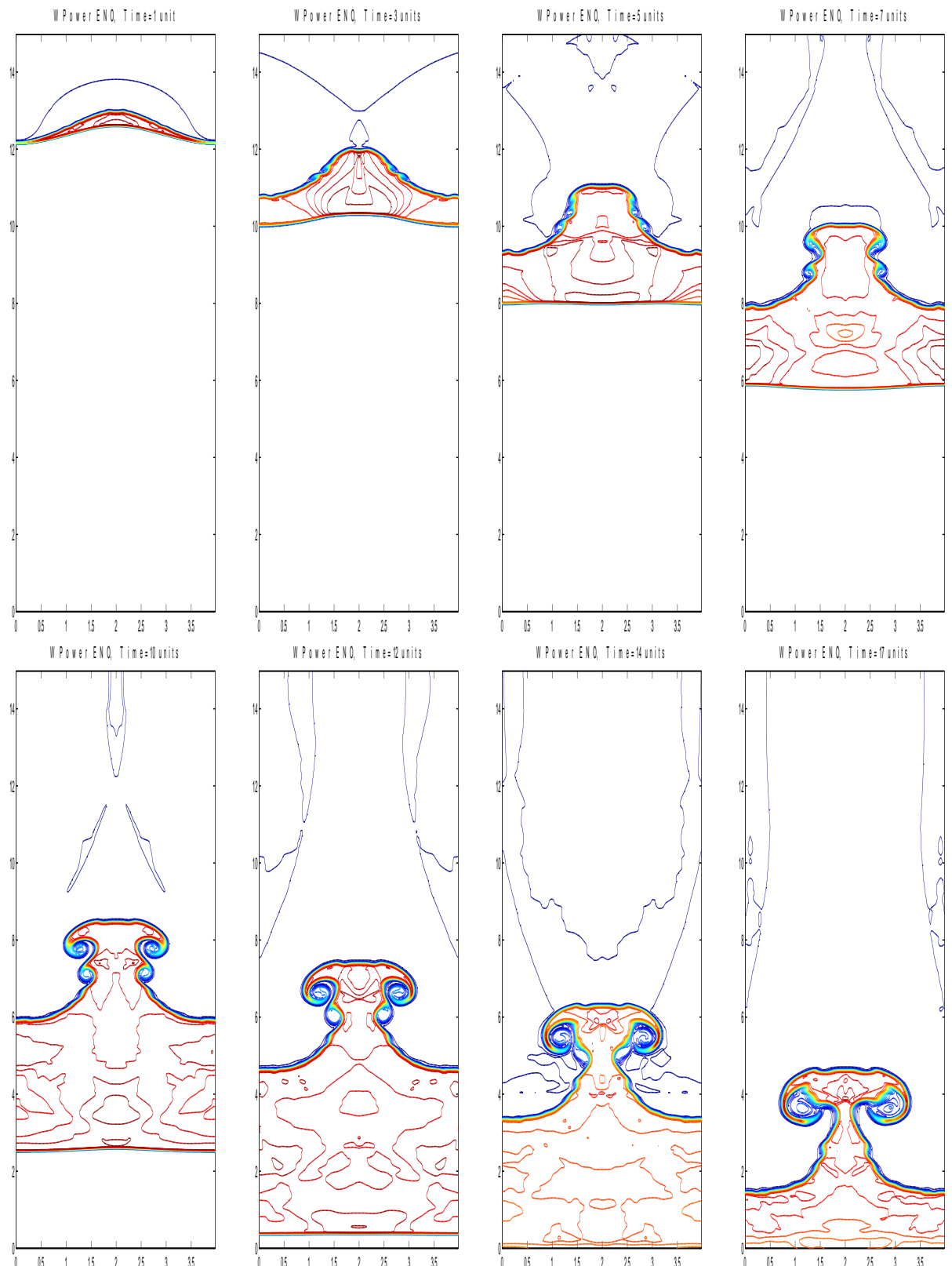


Figure 6.6: Snapshots of the Air-R22 Richtmyer-Meshkov instability evolution

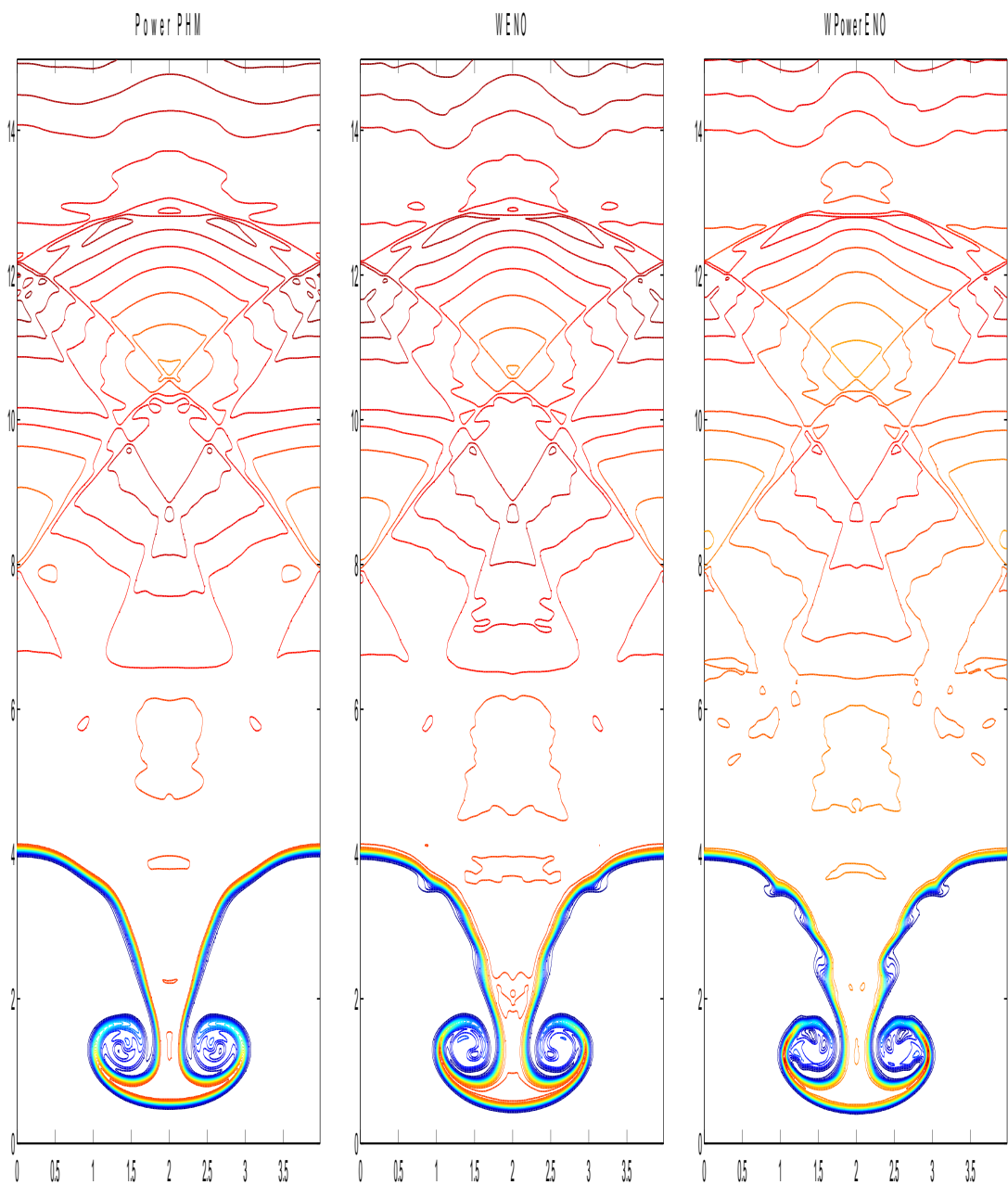


Figure 6.7: Comparison of the numerical solution of the Air-Helium RM instability for MFF-PowerPHM (left), MFF-WENO5 (center) and MFFWeighted PowerENO (right).

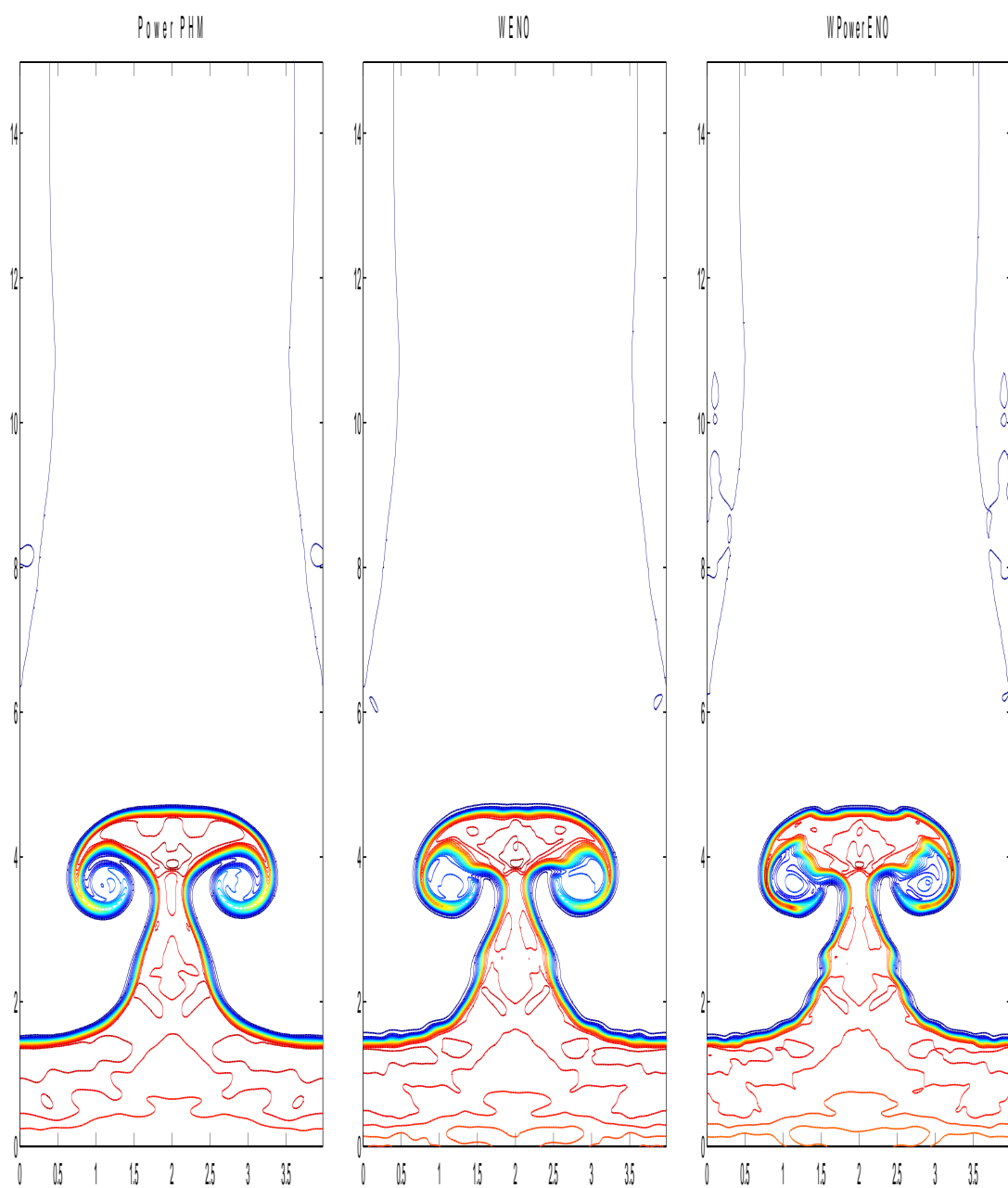


Figure 6.8: Comparison of the numerical solution of the Air-R22 RM instability for MFF-PowerPHM (left), MFF-WENO5 (center) and MFF-Weighted PowerENO (right).

CHAPTER 7

Summary and Conclusions

We have introduced new shock capturing schemes that reduce the numerical diffusion at discontinuities, sharpen the discontinuities in derivative and avoid spurious oscillations, improving the behavior of essentially non oscillatory schemes and piecewise hyperbolic methods. We have introduced and analyzed in this work a new class of limiter functions, the so called “power limiters”, which are an essential tool for the construction of these schemes. We have used the powereno limiter as a slope limiter for the design of a new piecewise hyperbolic method called the Power PHM method. We have also used the powereno limiter applied to consecutive second order finite differences to construct the Power ENO method. We have analyzed a new fifth order accurate Weighted Power ENO method as a nonlinear convex combination of the three Power ENO parabolas. We have checked the robustness, stability and accuracy of the proposed schemes in a set of model problems by means of several numerical tests. Finally, we have shown the ability of the presented schemes in resolving fine scales near unstable interfaces by computing Rayleigh-Taylor and Richtmyer-Meshkov instabilities.

As a general comment about the advantages of the proposed schemes we have the following remarks.

The third order accurate Power PHM scheme improves the behavior of PHM at local extrema and contact discontinuities, and it shares the advantages of the PHM. Since these are compact schemes (three point stencil), Power PHM is recommended over PHM when this condition is convenient for the computation (e.g., relaxation schemes).

Our fifth order accurate Weighted PowerENO scheme improves the behavior of WENO5 reducing the numerical viscosity at contact discontinuities and local extrema. It captures finer scales for a fixed computational grid. Our scheme is recommended when high order accuracy is a goal and when dealing with numerical schemes and simulations where a reduced (compact) stencil is not necessary.

Most of the research presented in this work is general and not restricted to the Euler equations of gas dynamics and, therefore, the theoretical results could be applied to many other problems. In fact, the new class of limiters and reconstruction procedures can be used also in conjunction with other techniques for the computation of the numerical flux, like staggered central schemes and Hamilton-Jacobi equations. This prospective research is expected to be developed in the near future.

REFERENCES

- [1] R. Artebrant and H. J. Schroll, *High-resolution Riemann-solver-free methods for conservation laws*, Hyperbolic Problems: Theory, Numerics, Applications, pp. 305–314, Springer, Berlin, 2003.
- [2] R. Artebrant and H. J. Schroll *Conservative logarithmic reconstructions and finite volume methods*, (to appear in SIAM J. Sci. Comput.) (2004)
- [3] R. Courant and K.O. Friedrichs, *Supersonic Flow and Shock Waves*, Springer-Verlag, New York, (1976).
- [4] R. Donat and A. Marquina, *Capturing shock reflections: an improved Flux Formula*, J. Comput. Phys., 125 (1996), pp. 42–58.
- [5] B. Engquist and S. Osher, *Stable and entropy satisfying approximations for transonic flow calculations*, Math. Comp., vol. 34, pp. 45–75, (1980).
- [6] A. F. Emery, J. Comput. Phys., 2, 306 (1968).
- [7] R.P. Fedkiw, A. Marquina and B. Merriman, *An isobaric fix for the overheating problem in multimaterial compressible flows*, J. Comput. Phys., 148 (1999), pp. 545–578.
- [8] S.K. Godunov, *A Finite Difference Method for the Numerical Computation of Discontinuous Solutions of the Equations of Fluid Dynamics*, Matematicheskii Sbornik, 47,p. 271 (1959).
- [9] Gottlieb, D. and Orszag, S. A., *Numerical Analysis of Spectral Methods: Theory and Applications*, SIAM, Philadelphia, (1977).
- [10] G. H. Hardy, J. E. Littlewood and G. Polya, *Inequalities*, Cambridge University Press, Cambridge (1973).
- [11] A. Harten, *High resolution schemes for hyperbolic conservation laws*, J. Comput. Phys., 49, (1983), pp. 357–393.
- [12] A. Harten, B. Engquist, S. Osher and S. Chakravarthy, *Uniformly high order accurate essentially non-oscillatory schemes III*, J. Comput. Phys., 71, No. 2, (1987), pp. 231–303.
- [13] G.S. Jiang and C. W. Shu, *Efficient Implementation of weighted ENO schemes*, J. Comput. Phys., 126, (1996), 202–228.

- [14] D. Kroener, *Numerical Schemes for Conservation Laws*, Wiley-Teubner, Chichester, (1997).
- [15] P.D. Lax, *Weak solutions of nonlinear hyperbolic equations and their numerical computation*, Commun. Pure Appl. Math., 7 (1954), pp. 159–193.
- [16] P.D. Lax, *The mathematical theory of shock waves. Regional Conference Series Lectures in Applied Mathematics*, 11, SIAM, Philadelphia, (1973).
- [17] P. D. Lax and B. Wendroff, *Systems of Conservation Laws*, Appl. Math., 13, (1960), 217-237.
- [18] S. Li and L. Petzold, *Moving mesh methods with upwinding schemes for time-dependent PDEs*, J. Comput. Phys., 131,(1997), pp. 368–377.
- [19] R.J. LeVeque *Numerical methods for conservation laws*, Birkhauser Verlag , Zuerich, (1990).
- [20] X-D. Liu and S. Osher and T. Chan *Weighted essentially non-oscillatory schemes*, J. Comput. Phys., 115, (1994), 200–212.
- [21] A. Marquina, *Local piecewise hyperbolic reconstructions for nonlinear scalar conservation laws*, SIAM J. Sci. Comput., 15,(1994), pp. 892–915.
- [22] A. Marquina and P. Mulet, *A flux-split algorithm applied to conservative models for multicomponent compressible flows* , J. Comput. Phys., 185, (2003), pp. 120–138.
- [23] A. Marquina and S. Serna, *Afternotes on PHM: Harmonic ENO methods*, Proceedings of the Ninth International Conference on Hyperbolic Problems: Theory, Numerics, Applications, HYP2002, Caltech, Pasadena, (California), (2002) , Springer, (in press).
- [24] E.E. Meshkov, NASA Tech T F, vol 13 p.74 (1970)
- [25] W. Mulder, S.J. Osher, J. Sethian, *Computing interface motion in compressible gas dynamics* , J. Comput. Phys., 100, (1992), pp. 209–228.
- [26] S. J. Osher, *Riemann solvers, the entropy condition and difference approximations*. SIAM J. Numer. Anal., 21, (1984), pp. 339–374.
- [27] S. J. Osher and S. Chakravarty, *High resolution schemes and the entropy condition*, SIAM J. Numer. Anal., 21, (1984), pp. 955–984.
- [28] R. Richtmyer, *Taylor instability in shock acceleration of compressible fluids*, Commun. Pure Appl. Math., 23, (1960), pp. 297–319.

- [29] A. Rogertson and E. Meiburg, *A Numerical Study of the Convergence of ENO schemes*, J. Sci. Comp., 5,(1990), 151–167.
- [30] H. J. Schroll , *High resolution relaxed upwind schemes in gas dynamics* , J. Sci. Comput., 17 (2002) pp. 599–607.
- [31] H. J. Schroll , *Relaxed high resolution schemes for hyperbolic conservation laws* , J. Sci. Comput., 21, 2, (2004).
- [32] C.W. Schulz-Rinne, J.P. Collins, and H.M. Glaz, *Numerical Solution of the Riemann problem for two-dimensional gas dynamics* , SIAM J. Sci. Comput., 14, (1993), pp. 1394–1414.
- [33] S. Serna and A. Marquina, *Power ENO Methods: A fifth order accurate Weighted Power ENO method*, J. Comput. Phys., 194, (2004), pp. 632–658.
- [34] J. Shi, YT Zhang, CW Shu, *Resolution of high order WENO schemes for complicated flow structures*, J. Comput. Phys., 186, (2003), pp. 690–696.
- [35] C. W. Shu, *Numerical Experiments on the Accuracy of ENO and modified ENO schemes*, J. Sci. Comp., 5, (1990), 127–150.
- [36] C. W. Shu and S. J. Osher, *Efficient Implementation of Essentially Non-Oscillatory Shock Capturing Schemes II*, J. Comput. Phys., 83, (1989), 32–78.
- [37] J. Smoller, *Shock Waves and Reaction-Diffusion Equations*, Springer Verlag, New York, (1983)
- [38] G. Sod, *A Survey of Several Finite Difference Methods for Systems of Non-linear Hyperbolic Conservation Laws*, J. Comput. Phys., 27, (1978), 1–31.
- [39] Y. Stiriba, *A nonlinear flux split method for hyperbolic conservation laws* , J. Comput. Phys., 176, (2002), pp. 20–39.
- [40] B. Van Leer, *Towards the ultimate conservative difference scheme V. A second order sequel to Godunov’s method*, J. Comput. Phys., 32,(1979), p.101–136.
- [41] P. Woodward and P.Colella, *The Numerical Simulation of Two-Dimensional fluid flow with strong shocks*, J. Comput. Phys., 54, (1984), 115–173.
- [42] YN Young, H. Tufo, A. Dubey, R. Rosner, *On the miscible Rayleigh-Taylor instability: two and three dimensions*, J. Fluid. Mech., 447,(2001), p.377-408.

CHAPTER 8

Resumen de la Memoria en castellano

8.1 Introducción

Los sistemas de leyes de conservación hiperbólicos han sido utilizados como modelos de una gran variedad de fenómenos físicos que abarca desde la aerodinámica hasta los modelos hidrodinámicos para semiconductores pasando por fluidos astrofísicos y predicción meteorológica. Nuestro campo de interés se dirige hacia las aproximaciones numéricas de la solución de sistemas de leyes de conservación con alto orden de precisión en espacio. Las propiedades cualitativas de la solución de los sistemas de conservación hacen particularmente interesante su simulación numérica ya que desarrollan discontinuidades de salto a tiempo finito y estructuras finas cerca de las interfas es inestables. Una simulación numérica precisa de la evolución en tiempo de estos procesos es importante para explicar y predecir fenómenos naturales y para usarlas en aplicaciones industriales.

A lo largo de los últimos cuarenta años ha tenido lugar un gran progreso en el desarrollo e investigación de esquemas de captura de ondas de choque de alto orden de precisión para la simulación numérica de fluidos complejos partiendo del trabajo original de Godunov. La introducción en los ochenta de los esquemas

esencialmente no oscilatorios, (ENO), basados en la interpolación polinómica como principal ingrediente para los esquemas de captura de ondas de choque de alta precisión ha sido el punto de inflexión a partir del cual se considera la investigación de nuevas funciones de reconstrucción suaves a trozos un campo de investigación de interés científico creciente en dinámica de fluidos computacional.

El principal objetivo de los métodos de alto orden es reducir la difusión en las discontinuidades además de conseguir alta precisión a lo largo de regiones suaves del fluido.

Este trabajo de investigación se centra en el estudio de esquemas de captura de ondas de choque de alto orden basados en procedimientos de reconstrucción que reduzcan la difusión en las discontinuidades, eviten oscilaciones espúreas y resuelvan regiones suaves del fluido con alto orden de precisión en espacio. Exploramos funciones de reconstrucción no polinómicas y polinómicas a trozos no oscilatorias con una variación total localmente acotada cerca de las discontinuidades.

En este trabajo de investigación introducimos nuevos esquemas de captura de ondas de choque de alto orden de precisión que mejoran el comportamiento de los esquemas esencialmente no oscilatorios en las discontinuidades de salto. Construimos y analizamos estos procedimientos de reconstrucción para la aproximación de la solución de leyes de conservación hiperbólicas, basados en una nueva clase de funciones limitadoras que hemos introducido con este propósito. Presentamos ejemplos numéricos para mostrar el buen comportamiento de los esquemas propuestos y aplicamos nuestros esquemas para simular inestabilidades de Richtmyer-Meshkov y Rayleigh-Taylor.

El Capítulo 2 se dedica a una revisión general sobre métodos numéricos para leyes de conservación hiperbólicas, centrándonos en lo esencial para los llamados esquemas de captura de ondas de choque. Hemos incluido una discusión sobre los principales aspectos que se refieren a las aproximaciones numéricas de alto orden de la solución de leyes de conservación hiperbólicas, esto es, difusión numérica y oscilaciones espúreas.

En el Capítulo 3 hacemos un análisis del papel de las funciones limitadoras en el diseño de métodos en diferencias finitas de alto orden de precisión e introducimos una nueva clase extendida de funciones limitadoras, los limitadores power, que incluyen algunos de los limitadores clásicos. Presentamos un estudio de los limitadores power en el contexto de los métodos basados en el esquema de Lax-Wendroff de Variación Total Decreciente y proponemos los limitadores powermod y powereno cumpliendo las propiedades necesarias para el diseño de procedimientos de reconstrucción no oscilatorios.

El Capítulo 4 se dedica al estudio de reconstrucciones suaves a trozos como herramienta esencial para el diseño de esquemas de captura de ondas de choque de alto orden de precisión. Hacemos un análisis de las reconstrucciones hiperbólicas a trozos utilizando los limitadores powermod y powereno en lugar del harmónico para limitar las diferencias divididas de primer orden y mostramos que el método resultante es de variación total localmente acotada. Exploramos el uso de los limitadores power en las reconstrucciones parabólicas a trozos limitando diferencias de segundo orden contiguas. Obtenemos una mejora del método de tercer orden de precisión ENO que llamamos método Power ENO. Al final de este Capítulo in-

troducimos un método de quinto orden de precisión, Weighted Power ENO, como una combinación convexa no lineal de las tres paráolas Power ENO, obteniendo un nuevo método que mejora el comportamiento del Weighted ENO, (WENO) clásico alrededor de las discontinuidades.

Después de este estudio analítico nos centramos en los resultados numéricos. En el Capítulo 5 presentamos una serie de test numéricos utilizando problemas modelo standard para verificar numéricamente la precisión, estabilidad y convergencia de los diferentes esquemas de alto orden de precisión presentados.

En el Capítulo 6 mostramos una aplicación de nuestros esquemas a la resolución de las inestabilidades de Rayleigh-Taylor y Richtmyer-Meshkov para demostrar la capacidad de los esquemas propuestos para capturar subescalas del fluido.

8.2 Métodos de Captura de Ondas de Choque para Leyes de Conservación Hiperbólicas

Un modelo continuo para un sistema físico se describe mediante leyes de conservación de la masa, momento y energía. Una ley de conservación para una variable física es una ecuación de balance que establece que la velocidad de cambio de la cantidad total contenida en una región G viene dada por su flujo (convectivo o difusivo) a través de la frontera ademas de otras fuentes internas posibles. La forma integral de esta ley de conservación es

$$\frac{d}{dt} \int_G u dV + \int_{\partial G} \bar{f}(u) \cdot \bar{n} dS = \int_G s(u) dV \quad (8.1)$$

donde u es la densidad de la cantidad conservada, $f(u)$ es el flujo y $s(u)$ la contribución de las fuentes internas.

Tomando G como un volumen infinitesimal y aplicando el teorema de la divergencia, obtenemos la forma diferencial de la ley de conservación

$$\frac{\partial u}{\partial t} + \nabla \cdot \bar{f}(u) = s(u) \quad (8.2)$$

que es la formulación para el modelado numérico del sistema físico continuo.

Podemos escribir un sistema de leyes de conservación como:

$$u_t^i + \nabla \cdot \bar{f}^i = 0, \quad i = 1, \dots, s \quad (8.3)$$

donde $\bar{u}(x, t) = (u^1, u^2, \dots, u^s)$ y su estado inicial viene dado por

$$u_t^i(x, 0) = u_0^i(x) \quad (8.4)$$

Un sistema de leyes de conservación se dice **hiperbólico** si el Jacobiano en cada dirección espacial es localmente diagonalizable con valores propios reales alrededor de la solución.

Muchas de las ideas fundamentales se desarrollaron para flujos compresibles (ecuaciones de Euler) para su aplicación en aerodinámica, astrofísica, ondas de detonación y flujos similares para los que las ondas de choque están presentes.

Estos flujos se modelan utilizando únicamente flujos convectivos, y están expresados como un sistema hiperbólico de leyes de conservación como se definieron anteriormente.

En la Memoria se hace una revisión de los esquemas de captura de ondas de choque partiendo de la forma conservativa. Se estudian los esquemas monótonos y se exponen los ejemplos más importantes: Lax-Friedrichs, Engquist-Osher y Godunov.

8.3 Una clase extendida de limitadores

El primer intento de obtener alto orden de precisión fue llevado a cabo por Lax and Wendroff en 1960 ([17]). El esquema de Lax-Wendroff se define como un esquema de captura de ondas de choque en forma conservativa como en (2.22) tal que

$$g_{j+\frac{1}{2}}^n = g_{LW}(u_j^n, u_{j+1}^n)$$

donde el flujo numérico está definido por

$$g_{LW}(u, v) = \frac{1}{2} \left[f(u) + f(v) \right] - \frac{\Delta t}{2h} f\left(\frac{u+v}{2}\right) [f(v) - f(u)] \quad (8.5)$$

y es consistente con el flujo de la ecuación. Este esquema está expresado en forma conservativa pero no es monótono. El esquema de Lax-Wendroff es un esquema de segundo orden en espacio y tiempo pero genera oscilaciones espúreas cerca de las discontinuidades.

Restringimos la discusión al problema modelo de la advección lineal

$$u_t + cu_x = 0 \quad (8.6)$$

El esquema de Lax-Wendroff para este problema se puede deducir del desarrollo de Taylor de la solución (8.6)

$$u(x, t_{n+1}) = u(x, t_n) + \Delta t u_t(x, t_n) + \frac{1}{2} (\Delta t)^2 u_{tt}(x, t_n) + \dots \quad (8.7)$$

De (8.6) tenemos que $u_t = -cu_x$ y diferenciando obtenemos

$$u_{tt} = -cu_{xt} = c^2 u_{xx} \quad (8.8)$$

teniendo en cuenta que $u_{xt} = u_{tx}$.

Sustituimos (8.8) en el desarrollo de Taylor y el resultado es

$$u(x, t_{n+1}) = u(x, t_n) - \Delta t c u_x(x, t_n) + \frac{1}{2} (\Delta t)^2 c^2 u_{xx}(x, t_n) + \dots \quad (8.9)$$

Si truncamos el último desarrollo manteniendo los tres primeros términos y sustituimos las derivadas espaciales por aproximaciones de las diferencias finitas centrales, obtenemos el esquema de Lax-Wendroff para la advección lineal.

$$u_j^{n+1} = u_j^n - \frac{\Delta t}{2h} c (u_{j+1}^n - u_{j-1}^n) + \frac{1}{2} (\Delta t)^2 c^2 \frac{u_{j+1}^n - 2u_j^n + u_{j-1}^n}{h^2} \quad (8.10)$$

En este caso la función flujo se expresa

$$g_{LW}(u, v) = \frac{1}{2} c(u + v) - \frac{1}{2} \Delta t h c^2 (v - u) \quad (8.11)$$

Así la viscosidad numérica del esquema de Lax-Wendroff es $\frac{1}{2}(\Delta t)^2 c^2$ para la advección lineal.

Van Leer en [40] diseñó un esquema de captura de ondas de choque de segundo orden sin oscilaciones espúreas cerca de las discontinuidades en términos de una función que limita las pendientes.

El modo más simple de medir cuan oscilatoria es una función o una aproximación numérica es analizando su variación total. Harten en [11] propuso calcular la variación total de u^n como

$$TV(u^n) := \sum_j |u_{j+1}^n - u_j^n| \quad (8.12)$$

La advección lineal propaga la señal u a la velocidad c sin cambiar la forma y el tamaño y, por lo tanto, la variación total (TV) de la solución debe ser constante en tiempo. Una aproximación numérica a esta ecuación podría no preservar la TV y, si la aproximación es oscilatoria, la TV de la solución puede crecer cuando evoluciona en tiempo.

Harten, en [11], introdujo el siguiente importante concepto:

Definition 4 *Un esquema numérico es Variación Total Decreciente (TVD) si*

$$TV(u^{n+1}) \leq TV(u^n) \quad (8.13)$$

para todo n .

Así, los esquemas TVD son no oscilatorios.

Harten propuso un criterio simple para determinar si un esquema numérico cumple la propiedad TVD ([11]):

Theorem 5 *Si un esquema numérico es de la forma*

$$u_j^{n+1} = u_j^n - C_{j-1}^n(u_j^n - u_{j-1}^n) + D_j^n(u_{j+1}^n - u_j^n) \quad (8.14)$$

donde los coeficientes C_{j-1}^n , D_j^n son valores arbitrarios (que pueden depender de u^n de un modo no lineal), entonces

$$TV(u^{n+1}) \leq TV(u^n) \quad (8.15)$$

bajo las condiciones

$$C_{j-1}^n \geq 0, \quad \forall j \quad (8.16)$$

$$D_j^n \geq 0, \quad \forall j \quad (8.17)$$

$$C_j^n + D_j^n \leq 1, \quad \forall j \quad (8.18)$$

Es fácil ver que un esquema de captura de ondas de choque monótono de primer orden es TVD, pero el recíproco no es cierto. Esto amplia la posibilidad de diseñar métodos TVD de segundo orden de precisión. Osher and Chakravarty diseñaron en [27] esquemas TVD de cualquier orden de precisión.

En el Capítulo 3 de la Memoria explicamos cómo construir un esquema limitador de flujo TVD basado en el esquema de Lax-Wendroff.

8.3.1 Power limiters

Los limitadores ENO, minmod (definido en la sección anterior), y harmónico se introdujeron para controlar el comportamiento de las reconstrucciones alrededor

de las discontinuidades para evitar el fenómeno de Gibbs y los “over/undershoots”.

Los limitadores están generalmente basados en una media entre dos números no negativos.

De hecho,

$$\text{minmod}(x, y) = \frac{(\text{sign}(x) + \text{sign}(y))}{2} \min(|x|, |y|) \quad (8.19)$$

$$\text{mineno}(x, y) = \text{minsign}(x, y) \min(|x|, |y|) \quad (8.20)$$

$$\text{harmod}(x, y) = \frac{(\text{sign}(x) + \text{sign}(y))}{2} \frac{2|x||y|}{|x| + |y|} \quad (8.21)$$

$$\text{hareno}(x, y) = \text{minsign}(x, y) \frac{2|x||y|}{|x| + |y|} \quad (8.22)$$

donde $\text{sign}(x)$ es la función signo, y

$$\text{minsign}(x, y) = \begin{cases} \text{sign}(x); & |x| \leq |y| \\ \text{sign}(y); & \text{en otro caso} \end{cases}$$

Estos limitadores están basados respectivamente en las medias mínimo y harmónica entre dos números no negativos.

Vamos a estudiar una extensa clase de medias, acotadas superiormente por la media aritmética, que contienen la media harmónica y el mínimo como casos particulares.

De hecho, si $x > 0$ e $y > 0$, entonces, para un número natural p , definimos la media power- p , ([33]), $\text{power}_p(x, y)$ como:

$$\text{power}_p(x, y) = \frac{(x + y)}{2} \left(1 - \left| \frac{x - y}{x + y} \right|^p \right) \quad (8.23)$$

La función $\text{power}_p(x, y)$ es homogénea de grado uno como función de dos variables.

Es fácil ver que

$$\text{power}_p(x, y) = \min(x, y) \left[1 + \left| \frac{y - x}{y + x} \right| + \cdots + \left| \frac{y - x}{y + x} \right|^{p-1} \right] \quad (8.24)$$

En particular, si $0 < x < y$ entonces

$$\text{power}_p(x, y) = x \left[1 + \left(\frac{y - x}{y + x} \right) + \cdots + \left(\frac{y - x}{y + x} \right)^{p-1} \right] \quad (8.25)$$

Esta es una serie geométrica truncada con ratio $r = \frac{y-x}{y+x} > 0$ y $r < 1$. La serie infinita converge a $\frac{x+y}{2}$. Entonces, las siguientes desigualdades se cumplen para cualquier $x > 0$ e $y > 0$:

$$\min(x, y) \leq \text{power}_p(x, y) \leq \text{power}_q(x, y) \leq \frac{x + y}{2}$$

para $0 < p < q$.

Además, para cualquier $x > 0$ e $y > 0$ tenemos

$$\text{power}_1(x, y) = \min(x, y) \quad (8.26)$$

$$\text{power}_2(x, y) = \frac{2xy}{x + y} \quad (8.27)$$

Las identidades anteriores son muy útiles para calcular la discrepancia entre la media aritmética y las medias Power_p y obtener expresiones simples de los errores de truncamiento como veremos en la siguiente sección.

La siguiente proposición describe una condición necesaria para que una media sea válida para diseñar un limitador útil en las reconstrucciones que son suaves a trozos y que su variación total en las celdas contiguas a una discontinuidad sea acotada. Esta propiedad no se satisface para la media aritmética ni para la media geométrica.

Proposition 8 *Si $x(h) > 0$ e $y(h) > 0$ son funciones del parámetro real $h > 0$, tal que $x(h) = O(1)$ e $y(h) = O(\frac{1}{h})$, entonces $\text{power}_p(x(h), y(h)) = O(1)$.*

Este resultado se deduce fácilmente a partir de la identidad (8.25).

Definimos los correspondientes limitadores:

$$\text{powermod}_p(x, y) = \frac{(\text{sign}(x) + \text{sign}(y))}{2} \text{power}_p(|x|, |y|) \quad (8.28)$$

$$\text{powereno}_p(x, y) = \text{minsign}(x, y) \text{power}_p(|x|, |y|) \quad (8.29)$$

Las identidades siguientes muestran que los limitadores minmod, ENO y harmónico son casos particulares del limitador Power_p:

$$\text{powermod}_1(x, y) = \text{minmod}(x, y) \quad (8.30)$$

$$\text{powereno}_1(x, y) = \text{mineno}(x, y) \quad (8.31)$$

$$\text{powermod}_2(x, y) = \text{harmod}(x, y) \quad (8.32)$$

$$\text{powereno}_2(x, y) = \text{hareno}(x, y) \quad (8.33)$$

En el Capítulo 3 de la Memoria realizamos un estudio detallado de las condiciones para las que un limitador power determina un esquema TVD limitador de flujo basado en el esquema de Lax-Wendroff.

8.4 Funciones de reconstrucción suaves a trozos

Nuestro objetivo general consiste en obtener aproximaciones numéricas de alto orden de precisión a funciones reales de una variable real suaves a trozos con un número finito de discontinuidades de salto para aproximar la solución de sistemas de leyes de conservación hiperbólicas. Un procedimiento simple y útil es definir la escala de computación en términos de una partición del intervalo del dominio de la función y usar una función básica elemental (fácil de calcular, e.g. polinómica, racional,...), para cada subintervalo de manera que localmente aproxime la función original. El grado de suavidad local de la función original determina la escala mas fina para la cual necesitamos reconstruir la función y la elección del grado de precisión. La elección del tamaño de la partición y del grado de precisión para un problema específico es una tarea difícil.

Nuestra discusión se centrará sobre una red uniforme fija y un grado fijo de precisión local intentando minimizar la información espúrea generada cuando se tratan simultáneamente escalas finas y groseras. Para alcanzar este objetivo diferentes autores han estado desarrollando varios procedimientos para evitar traspasar información espúrea de escalas finas a groseras y viceversa. El fenómeno de Gibbs o el efecto oscilatorio de Runge se encuentran generalmente cuando se aproxima una función suave a trozos y estos efectos son ejemplos bien conocidos

de esta clase de comportamiento desafortunado.

El problema de aproximación mencionado anteriormente se hace más difícil cuando la función que ha de ser aproximada evoluciona con el tiempo regulado mediante una ecuación en derivadas parciales dependiente del tiempo. En este caso la relación entre escalas finas y groseras puede cambiar de un modo no lineal. Por lo tanto, el procedimiento de aproximación debería ser adaptativo para tener en cuenta todas estas circunstancias. Este problema ha sido considerado en dinámica de fluidos computacional para obtener simulaciones numéricas con precisión de fluidos compresibles, (ver [1, 2, 11, 12, 13, 20, 21, 26, 30, 31, 33]).

Una aproximación de primer orden a una función suave a trozos sobre una malla fija puede ser definida como una función constante a trozos con discontinuidades de salto localizadas en las interfas. Van Leer consideró aproximaciones de segundo orden definidas como funciones lineales a trozos introduciendo por primera vez la función limitadora minmod aplicada sobre pendientes contiguas para evitar el fenómeno de Gibbs cerca de las discontinuidades cuando se calculan soluciones aproximadas a leyes de conservación hiperbólicas [19]. Los esquemas de Variacion Total Decreciente (TVD) se introdujeron en [11] para obtener aproximaciones no oscilatorias de la solución de las leyes de conservación hiperbólicas de alto orden de precisión, pero la principal desventaja de estos esquemas es la degeneración a primer orden de precisión en los extremos locales [27]. Los métodos Esencialmente No Oscilatorios (ENO), se introdujeron para obtener procedimientos de reconstrucción de alto orden de precisión de orden mayor que dos evitando el fenómeno de Gibbs y las oscilaciones espúreas de una amplitud

del orden del error local de truncamiento ([12]). Los procedimientos ENO utilizan el polinomio interpolador más suave elegido según la diferencia de menor tamaño siguiendo una algoritmo tipo árbol. El procedimiento de selección de los métodos ENO es una función limitadora actuando sobre las diferencias sucesivas de los datos. Uno de los aspectos importantes de los procedimientos de reconstrucción de alto orden de precisión es el tamaño del *stencil*, es decir, el número de datos puntuales necesarios para llevar a cabo la aproximación. Si el *stencil* es pequeño el comportamiento del procedimiento es robusto cuando se usa en problemas de evolución donde las discontinuidades están moviéndose o interactuando pero el grado de precisión es limitado. Mediante el uso de funciones limitadoras podemos diseñar procedimientos de reconstrucción con un tamaño del *stencil* óptimo y con buena resolución de las discontinuidades.

Para fijar nuestra notación y estructura computacional consideramos aproximaciones numéricas al problema escalar de valores iniciales

$$u_t + f(u)_x = 0, \quad (8.34)$$

$$u(x, t) = u_0(x), \quad (8.35)$$

donde u_0 es una función suave a trozos periódica o de soporte compacto.

Queremos obtener aproximaciones numéricas de una función suave a trozos $g(x)$ a partir de sus medias en celda, dadas para las celdas de la malla uniforme definida anteriormente de tamaño $h > 0$, $x_j = jh$,

$$v_j = \frac{1}{h} \int_{x_{j-\frac{1}{2}}}^{x_{j+\frac{1}{2}}} g(x, t_n) dx \quad (8.36)$$

La malla uniforme específica considerada es la escala de computación elegida para nuestra aproximación. La idea es capturar subescalas de la escala original elegida en términos de una función suave a trozos, R , tal que la restricción a cada celda computacional $[x_{j-\frac{1}{2}}, x_{j+\frac{1}{2}}]$, es una función elemental adecuada, R_j , tal que

$$v_j = \frac{1}{h} \int_{x_{j-\frac{1}{2}}}^{x_{j+\frac{1}{2}}} R_j(x, t_n) dx \quad (8.37)$$

y aproxima g hasta un grado de precisión.

Vamos a analizar el comportamiento de R en términos de h , cuando h tiende a cero. Este comportamiento puede ser indeseable alrededor de las discontinuidades de salto de g ya que la función R puede desarrollar tanto el fenómeno de Gibbs como el efecto oscilatorio de Runge. Por otro lado, el orden de precisión puede degenerar a través de regiones suaves de g debido a la presencia de las singularidades anteriores. Los problemas computacionales mencionados están siempre presentes cuando usamos la estructura descrita para aproximar la solución de leyes de conservación hiperbólicas, ya que esas ecuaciones de evolución pueden desarrollar discontinuidades (choques) en tiempo finito (see [12, 21, 36]).

Nos vamos a centrar en funciones suaves de tercer orden de precisión R , de manera que cada R_j está determinado a partir de la condición (8.37) y dos condiciones más, generalmente obtenidas de diferencias de v_j . Denotamos por

$$d_{j+\frac{1}{2}} = v_{j+1} - v_j \quad (8.38)$$

Si sabemos las primeras derivadas de g en las interfases, es decir, $g'(x_{j+\frac{1}{2}})$, podemos utilizar las dos condiciones siguientes de interpolación para asegurar el tercer orden de precisión en zonas suaves.

$$R'_j(x_j - \frac{h}{2}) = g'(x_{j-\frac{1}{2}}) \quad (8.39)$$

$$R'_j(x_j + \frac{h}{2}) = g'(x_{j+\frac{1}{2}}) \quad (8.40)$$

Utilizamos las diferencias divididas de primer orden $\frac{d_{j-\frac{1}{2}}}{h}$ y $\frac{d_{j+\frac{1}{2}}}{h}$ en lugar de $g'(x_{j-\frac{1}{2}})$ $g'(x_{j+\frac{1}{2}})$ respectivamente si los últimos valores no están disponibles. Si consideramos una parábola local de la forma

$$p_j(x) = a_j + b_j(x - x_j) + \frac{c_j}{2}(x - x_j)^2 \quad (8.41)$$

hay una única parábola tal que las condiciones (8.37), (8.39) y (8.40) se satisfacen, esto es a_j , b_j y c_j están unívocamente definidas.

A partir de [21], si consideramos hipérbolas de la forma

$$r_j = e_j + \frac{\lambda_j}{(x - x_j) + f_j} \quad (8.42)$$

podemos obtener una única hipérbola que satisface (8.37), (8.39) y (8.40), (λ_j , e_j y f_j están unívocamente definidas), suponiendo que $g'(x_{j-\frac{1}{2}}) \cdot g'(x_{j+\frac{1}{2}}) > 0$, ya que las hipérbolas son funciones monótonas.

Queremos estudiar cuan oscilatoria es la aproximación R de la función $g(x)$ en términos de h . Para tener una comparación grosera entre las reconstrucciones

parabólicas e hiperbólicas, podemos suponer, para simplificar, la siguiente notación. Consideramos la celda para $j = 0$, $[x_{-\frac{1}{2}}, x_{\frac{1}{2}}]$, y utilizamos $d_l := \frac{d_{-\frac{1}{2}}}{h}$ y $d_r := \frac{d_{\frac{1}{2}}}{h}$.

Si $d_l \cdot d_r > 0$, la variación total de la parábola p_0 (suponiendo que p_0 es monótona) es

$$TV(p_0) = h \frac{|d_l| + |d_r|}{2} \quad (8.43)$$

y la variación total de la hipérbola r_0 es, (see [21]),

$$TV(r_0) = h \sqrt{|d_l| \cdot |d_r|} \quad (8.44)$$

De la desigualdad aritmético-geométrica concluimos que la reconstrucción parabólica prescribe más variación total que la de la hipérbola. Observamos que las fórmulas (8.43) y (8.44) son el producto de h veces una media de dos números positivos. Si g es suave en una región que contiene nuestra celda computacional $[-\frac{h}{2}, \frac{h}{2}]$, entonces d_l y d_r están acotados y por lo tanto, $TV(p_0) = O(h)$ y $TV(r_0) = O(h)$. Así, p_0 y r_0 son suficientemente suaves para ser no oscilatorias y esas cantidades tienden a cero con h .

Por otro lado, si g tiene una discontinuidad de salto en $x_0 = 0$, o bien d_l , o bien d_r es $O(\frac{1}{h})$, y

$$TV(p_0) = O(1) \quad (8.45)$$

y

$$TV(r_0) = O\left(\sqrt{h}\right) \quad (8.46)$$

Así, en presencia de discontinuidades, las hipérbolas son mucho menos oscilatorias que las paráolas.

Una manera de hacer menos oscilatoria una aproximación suave a trozos es usando limitadores de pendiente para preprocesar derivadas de primer orden de manera que el orden de precisión no degenera.

Podemos decir que las hipérbolas tienen un mecanismo natural para limitar el gradiente en términos de una media. De hecho, la primera derivada de r_0 en $x = 0$ es, por [21],

$$r'_0(x_0) = \text{sign}(d_l) \left(\frac{2\sqrt{|d_l|}\sqrt{|d_r|}}{\sqrt{|d_l|} + \sqrt{|d_r|}} \right)^2 \quad (8.47)$$

lo que es mucho mas pequeño en tamaño que la de la parábola,

$$p'_0(x_0) = \text{sign}(d_l) \frac{|d_l| + |d_r|}{2} \quad (8.48)$$

teniendo en cuenta que $d_l \cdot d_r > 0$, (ver Hardy, Littlewood and Polya, [10]).

Así, nuestro principal objetivo para reconstrucciones suaves a trozos es controlar el crecimiento de la variación total. La condición de variación total localmente acotada fue introducida en [21] con este propósito.

Definition 5 Una reconstrucción suave a trozos R es de variación total localmente acotada (LTVB) si existe una constante $M > 0$, independiente de h , tal que, para todo j ,

$$TV(R_j) \leq Mh \quad (8.49)$$

Vamos a construir y analizar reconstrucciones suaves a trozos usando tanto hipérbolas como paráolas que satisfagan la condicion LTVB.

8.4.1 Reconstrucciones Hiperbólicas

Marquina propuso en [21] reconstrucciones hiperbólicas a trozos del tipo (8.42).

Las reconstrucciones hiperbólicas no oscilatorias fueron propuestas en [21] para obtener tercer orden de precisión espacial usando un *stencil* de tres puntos para mejorar la resolución de esquinas de rarefacción en cálculo de fluidos compresibles. La media harmónica de las derivadas laterales fue utilizada en [21] para alcanzar la propiedad de no oscilatoriedad de la función de reconstrucción evitando la ampliación del *stencil*.

Los métodos hiperbólicos a trozos (PHM), han sido utilizados en una gran variedad de problemas. La reconstrucción hiperbólica a trozos es una reconstrucción de tercer orden de precisión que es robusta con los esquemas de captura de ondas de choque ([4], [7], [21], [22], [39]), esquemas de relajación ([1], [30], [31]), y métodos de mallas móviles ([18]). Este buen comportamiento se debe principalmente a:

1. *Stencil* reducido.
2. Las hipérbolas son menos oscilatorias que las paráolas (como se ha visto en la introducción a esta sección).
3. El uso de un limitador basado en la media harmónica.

8.4.1.1 Método Power Piecewise Hyperbolic

Podemos expresar una hipérbola $r_0(x)$ en términos de un d_0 y α , (para $-2 < \alpha < 2$), cumpliendo (8.37) y $r'_0(x_0) = d_0$, en la forma,

$$r_0(x) = v_0 + d_0 h \frac{1}{\alpha^2} \left[\log\left(\frac{2-\alpha}{2+\alpha}\right) - \frac{\alpha h}{\alpha(x-x_0)-h} \right] \quad (8.50)$$

Una elección apropiada de d_0 y α da una hipérbola que interpola una de las derivadas laterales.

Dos casos son relevantes para este objetivo, (Marquina, [21]):

- (a) Si $d_0 \cdot d_l > 0$ entonces $\alpha = 2(\sqrt{\frac{d_0}{d_l}} - 1)$ si y sólo si $d_l = r'(x_0 - \frac{h}{2})$.
- (b) Si $d_0 \cdot d_r > 0$ entonces $\alpha = 2(1 - \sqrt{\frac{d_0}{d_r}})$ si y sólo si $d_r = r'(x_0 + \frac{h}{2})$.

La reconstrucción hiperbólica harmónica local, LHHR, se introdujo en [21] como una reconstrucción hiperbólica que satisface la condición LTVB debido a la falta de esta propiedad para hipérbolas naturales.

La reconstrucción LHHR propone, en cada celda computacional, una hipérbola r_j que satisface (8.37), interpola la derivada lateral con el menor valor absoluto, y asigna, como derivada central (d_0), la media harmónica de ambas derivadas laterales en lugar de (8.42). En este caso, el rango de valores de α , independiente de h , se restringe a

$$-2(\sqrt{2} - 1) < \alpha < 2(\sqrt{2} - 1) \quad (8.51)$$

Esta desigualdad es esencial para probar que la reconstrucción LHHR es LTVB ([21]).

La principal desventaja de la reconstrucción LHHR es la pérdida de precisión en los extremos locales y, como consecuencia, la pérdida de variación total en esos puntos.

Nuestro objetivo es mejorar el efecto que resulta de aplicar la media harmónica sobre derivadas laterales en LHHR utilizando la media power₃ en su lugar e igualmente asegurar la existencia de un número positivo β que satisfaga $-2\beta \leq \alpha \leq 2\beta$ y $\sqrt{2} - 1 \leq \beta < 1$.

Con este propósito tenemos que comparar la media power₃ con la harmónica y la media natural de la hipérbola (8.42).

En el Capítulo 4 de la Memoria hacemos un análisis comparativo de estas tres medias para entender mejor el comportamiento de los limitadores power en las reconstrucciones hiperbólicas.

Para definir una reconstrucción hiperbólica LHHR, es necesario conocer el valor del cociente entre la media harmónica de las derivadas laterales y la derivada lateral con el menor valor absoluto.

Definimos el cociente para \mathcal{P}_3 como:

$$\mathcal{R}_3(x, y) = \frac{x^2 + y^2 + 2(\max(x, y))^2}{(x + y)^2} \quad (8.52)$$

definido para $x \geq 0$ e $y \geq 0$, no simultáneamente cero.

A partir de [33], definimos powereno₃(x, y) = powereno₃(x, y). Utilizamos este limitador para el diseño de la reconstrucción local power-hiperbólica.

El algoritmo siguiente define una hipérbola en términos de d_0 y α de acuerdo

con (8.50).

METODO DE RECONSTRUCCION LOCAL POWER-HIPERBOLICO (LHPR)

Definimos $tol = h^2$,

if ($|d_l| \leq tol$) and ($|d_r| \leq tol$) **then**

$d_0 = 0$ and $\alpha = 0$

else

$$d_0 = \text{powereno}(d_l, d_r) = \text{minsign}(dl, dr) \min(|dl|, |dr|) \frac{dl^2 + dr^2 + 2(\max(|dl|, |dr|))^2}{(|dl| + |dr|)^2}$$

if $|d_l| \leq |d_r|$ **then**

$$\text{ratio} = \frac{d_l^2 + 3d_r^2}{(|d_l| + |d_r|)^2} (= \mathcal{R}_3)$$

$$\alpha = 2(\sqrt{\text{ratio}} - 1)$$

else

$$\text{ratio} = \frac{3d_l^2 + d_r^2}{(|d_l| + |d_r|)^2} (= \mathcal{R}_3)$$

$$\alpha = 2(1 - \sqrt{\text{ratio}})$$

end

end

Los lemas siguientes muestran que este algoritmo proporciona una hipérbola bien definida y sus demostraciones pueden encontrarse en el Capítulo 4 de la Memoria.

Lemma 4 $\mathcal{R}_3 \leq 3$ para $x \geq 0$ e $y \geq 0$ no simultáneamente cero.

Lemma 5 El rango de valores del parámetro adimensional α para el método LHPR es

$$-2(\sqrt{3} - 1) < \alpha < 2(\sqrt{3} - 1) \quad (8.53)$$

Así tenemos la propiedad LTVB para LHPR.

Theorem 6 *El método LHPR es LTVB.*

8.4.2 Reconstrucciones parabólicas

Las aproximaciones numéricas de alto orden de precisión a funciones suaves a trozos con discontinuidades de salto son de tal manera que alcanzan alto orden de precisión en regiones suaves y perfiles nítidos de discontinuidades sin oscilaciones espúreas. Los procedimientos polinómicos de reconstrucción esencialmente no oscilatorios (ENO) fueron diseñados para cumplir este propósito ([12]). Los métodos ENO son de alto orden en regiones suaves y se comportan de manera robusta en los choques. Sin embargo, después de que diferentes experimentos han sido llevados a cabo con los métodos ENO, algunas desventajas de estos métodos se han hecho relevantes, como las que mencionamos a continuación:

1. Pérdida de precisión en regiones suaves para datos específicos, ([29]).
2. Difusión de ciertas discontinuidades ([13]).
3. Suavización de las esquinas, (discontinuidades de la primera derivada), ([21]).
4. *Stencil* demasiado amplio para obtener alto orden de precisión, ([13]).

Para superar estas dificultades, (ver [29]), se han propuesto diferentes remedios. Shu propuso en [35] una selección ENO más centrada para reducir la pérdida de precisión . Los métodos Weighted ENO de Liu, Osher y Chan ([20]), se diseñaron para obtener precisión óptima para un *stencil* específico degenerando a un método ENO clásico en las discontinuidades.

8.4.2.1 El método PowerENO

Todos los métodos de reconstrucción polinómicos analizados en este trabajo tienen el mismo *stencil* que el método ENO clásico y están basados en paráolas de la forma:

$$p_j(x) = a_j + (x - x_j) \left[b_j + \frac{c_j}{2}(x - x_j) \right] \quad (8.54)$$

definido en I_j donde a_j , b_j y c_j están determinados a partir de los datos de la malla.

Utilizamos 8.38 y la notación adicional siguiente:

$$d_j = \frac{d_{j+\frac{1}{2}} + d_{j-\frac{1}{2}}}{2} \quad (8.55)$$

$$D_j = d_{j+\frac{1}{2}} - d_{j-\frac{1}{2}} \quad (8.56)$$

El método clásico ENO3 está basado en un procedimiento de selección que elige una parábola entre tres candidatas, ([12, 36]):

$$p_{j-1}(x) = v_j - \frac{D_{j-1}}{24} + \frac{x - x_j}{h} \left[d_{j-\frac{1}{2}} + \frac{D_{j-1}}{2} + \frac{D_{j-1}}{2} \left(\frac{x - x_j}{h} \right) \right] \quad (8.57)$$

$$p_j(x) = v_j - \frac{D_j}{24} + \frac{x - x_j}{h} \left[d_j + \frac{D_j}{2} \left(\frac{x - x_j}{h} \right) \right] \quad (8.58)$$

$$p_{j+1}(x) = v_j - \frac{D_{j+1}}{24} + \frac{x - x_j}{h} \left[d_{j+\frac{1}{2}} - \frac{D_{j+1}}{2} + \frac{D_{j+1}}{2} \left(\frac{x - x_j}{h} \right) \right] \quad (8.59)$$

lo que corresponde a la elección izquierda, central y derecha respectivamente.

El procedimiento de selección del ENO3 para obtener la parábola ENO en la celda computacional $C_j = [x_{j-\frac{1}{2}}, x_{j+\frac{1}{2}}]$ es el siguiente:

si $|d_{j-\frac{1}{2}}| \leq |d_{j+\frac{1}{2}}|$ **entonces**

si $|D_{j-1}| \leq |D_j|$ **entonces**

$p_{j-1}(x)$

si no

$p_j(x)$

fin

si no

si $|D_j| \leq |D_{j+1}|$ **entonces**

$p_j(x)$

si no

$p_{j+1}(x)$

fin

fin

Para explorar nuevos métodos y diseñar métodos ENO tal que obtengamos mejor comportamiento cerca de las discontinuidades, hacemos entrar en juego en nuestro estudio dos nuevas paráolas en lugar de las elecciones izquierda y derecha utilizadas en ENO3. Construimos estas nuevas paráolas utilizando un valor intermedio entre dos diferencias de segundo orden contiguas:

$$p_{j-\frac{1}{2}}^M(x) = v_j - \frac{M_{j-\frac{1}{2}}}{24} + \frac{x - x_j}{h} \left[d_{j-\frac{1}{2}} + \frac{M_{j-\frac{1}{2}}}{2} + \frac{M_{j-\frac{1}{2}}}{2} \left(\frac{x - x_j}{h} \right) \right] \quad (8.60)$$

$$p_{j+\frac{1}{2}}^M(x) = v_j - \frac{M_{j+\frac{1}{2}}}{24} + \frac{x - x_j}{h} \left[d_{j+\frac{1}{2}} - \frac{M_{j+\frac{1}{2}}}{2} + \frac{M_{j+\frac{1}{2}}}{2} \left(\frac{x - x_j}{h} \right) \right] \quad (8.61)$$

donde $M_{j-\frac{1}{2}} := \text{media}(D_{j-1}, D_j)$ and $M_{j+\frac{1}{2}} := \text{media}(D_j, D_{j+1})$, donde “media” es un valor intermedio que eventualmente puede ser un limitador (ver [23]).

A continuación introducimos el método de tercer orden de precisión **Power ENO**.

Utilizaremos los limitadores powereno₃ o powermod₃ (limitadores basados en la media power₃, introducida en el Capítulo 8.3), calculadas entre dos diferencias de segundo orden contiguas en el lugar de la media M , mencionada anteriormente. Para simplificar nos referiremos a estos limitadores como **powereno** y **powermod** evitando el subíndice.

Utilizaremos las siguientes tres paráolas:

$$p_{j-\frac{1}{2}}^P(x) = v_j - \frac{P_{j-\frac{1}{2}}}{24} + \frac{x - x_j}{h} \left[d_{j-\frac{1}{2}} + \frac{P_{j-\frac{1}{2}}}{2} + \frac{P_{j-\frac{1}{2}}}{2} \left(\frac{x - x_j}{h} \right) \right] \quad (8.62)$$

$$p_j(x) = v_j - \frac{D_j}{24} + \frac{x - x_j}{h} \left[d_j + \frac{D_j}{2} \left(\frac{x - x_j}{h} \right) \right] \quad (8.63)$$

$$p_{j+\frac{1}{2}}^P(x) = v_j - \frac{P_{j+\frac{1}{2}}}{24} + \frac{x - x_j}{h} \left[d_{j+\frac{1}{2}} - \frac{P_{j+\frac{1}{2}}}{2} + \frac{P_{j+\frac{1}{2}}}{2} \left(\frac{x - x_j}{h} \right) \right] \quad (8.64)$$

lo que corresponde a las elecciones izquierda, central y derecha respectivamente y $P_{j-\frac{1}{2}} = \text{powereno}(D_{j-1}, D_j)$ y $P_{j+\frac{1}{2}} = \text{powereno}(D_j, D_{j+1})$. El método Power ENO3 se define eligiendo una de las parábolas anteriores siguiendo el mismo procedimiento de selección del método ENO3. Si utilizaramos el limitador powereno_1 en lugar del powereno, recuperaríamos el método ENO3.

En [21], se muestra que el método ENO3 es de variación total localmente acotada.

Siguiendo un argumento análogo se puede ver que:

Proposition 9 *El método Power ENO3 es de variación total localmente acotada. Es decir, $TV(r) = O(h)$, donde r_j es la reconstrucción para la celda C_j y h es el paso espacial.*

8.4.2.2 Método Weighted PowerENO

Liu et al. en [20] introdujeron los esquemas Weighted ENO utilizando una estructura de media en celda. Los valores espaciales se calculan utilizando una

combinación convexa de las parábolas mediadas en celda del ENO3 obteniendo así cuarto orden de precisión. Basado en las parábolas puntuales ENO3 descritas en la sección anterior, Jiang y Shu desarrollaron en [13] el método WENO5 utilizando una combinación convexa no lineal de las parábolas anteriores alcanzando quinto orden de precisión mediante un nuevo tipo de medida de suavidad expresado en términos de los llamados indicadores de suavidad.

Para mostrar el interés prospectivo de nuestro método Power ENO vamos a construir un nuevo método Weighted ENO como una combinación convexa de las tres parábolas (8.62), (8.63) y (8.64) utilizadas para el método Power ENO3. Entonces, para calcular los pesos lineales óptimos para este método necesitamos conocer expresiones simples de los errores de truncamiento de las parábolas anteriores. Podemos obtener expresiones simples utilizando la media aritmética en lugar de nuestro limitador no lineal.

Proposition 10 *Si utilizamos la media aritmética A, es decir, $A(x, y) := \frac{x+y}{2}$, para las parábolas (8.60) and (8.61), entonces, tenemos las siguientes expresiones de los errores de truncamiento en la interfase de la derecha, $x_{j+\frac{1}{2}}$:*

$$p_{j-\frac{1}{2}}^A(x_{j+\frac{1}{2}}) - u = -4 \left(\frac{h}{2}\right)^3 \frac{u'''}{6} + \frac{256}{5} \left(\frac{h}{2}\right)^4 \frac{u^{(iv)}}{24} + O(h^5) \quad (8.65)$$

$$p_{j+\frac{1}{2}}^A(x_{j+\frac{1}{2}}) - u = -\frac{64}{5} \left(\frac{h}{2}\right)^4 \frac{u^{(iv)}}{24} + O(h^6) \quad (8.66)$$

La demostración detallada de esta Proposición la presentamos en el Capítulo 4 de la Memoria.

Necesitamos utilizar otros limitadores en lugar de la media aritmética para

obtener reconstrucciones de variación total estables de un modo en que las expresiones del error de truncamiento anteriores sean válidas hasta el mayor orden posible.

Aplicamos nuestros limitadores sobre diferencias centrales de segundo orden. Así, si x e y son diferencias centrales de segundo orden contiguas calculadas en una región suave, tenemos que $x = O(h^2)$, $y = O(h^2)$ y $x - y = O(h^3)$ y por lo tanto,

Proposition 11

$$\frac{x + y}{2} - \text{power}_p(x, y) = O(h^{p+2})$$

Proof. Se deduce fácilmente de

$$\begin{aligned} \frac{x + y}{2} - \text{power}_p(x, y) &= \frac{x + y}{2} \left[1 - 1 + \left| \frac{x - y}{x + y} \right|^p \right] \\ &= \frac{x + y}{2} \left| \frac{x - y}{x + y} \right|^p \\ &= O(h^{2+p}). \end{aligned} \tag{8.67}$$

□

El siguiente teorema se deduce de la Proposición 11.

Theorem 7 *Las siguientes afirmaciones son ciertas:*

- (1) *Las expresiones del error de truncamiento de la media aritmética son válidas hasta tercer orden para los limitadores harmod y hareno, (los limitadores power_p con p = 2).*
- (2) *Las expresiones del error de truncamiento de la media aritmética son*

válidos hasta los términos de cuarto orden para los limitadores powermod y powereno.

A partir de la Proposición 10 y del Teorema 7 las siguientes expresiones del error de truncamiento en la interfase derecha son válidas para las paráolas Power ENO:

$$p_{j-\frac{1}{2}}^P(x_{j+\frac{1}{2}}) - u = -4 \left(\frac{h}{2}\right)^3 \frac{u'''}{6} + \frac{256}{5} \left(\frac{h}{2}\right)^4 \frac{u^{(iv)}}{24} + O(h^5)$$

$$p_j(x_{j+\frac{1}{2}}) - u = 4 \left(\frac{h}{2}\right)^3 \frac{u'''}{6} - \frac{64}{5} \left(\frac{h}{2}\right)^4 \frac{u^{(iv)}}{24} + O(h^5)$$

$$p_{j+\frac{1}{2}}^P(x_{j+\frac{1}{2}}) - u = -\frac{64}{5} \left(\frac{h}{2}\right)^4 \frac{u^{(iv)}}{24} + O(h^6)$$

Así, para las expresiones anteriores podemos alcanzar quinto orden de precisión en regiones suaves obteniendo el grado de precisión óptimo utilizando un procedimiento análogo al seguido en [13], (ver también [20]).

De hecho, en este caso, los pesos lineales óptimos para obtener esta precisión están únicamente determinados en la interfase de la derecha como la combinación convexa:

$$w_0 \cdot p_{j-\frac{1}{2}}^P(x_{j+\frac{1}{2}}) + w_1 \cdot p_j(x_{j+\frac{1}{2}}) + w_2 \cdot p_{j+\frac{1}{2}}^P(x_{j+\frac{1}{2}}) \quad (8.68)$$

donde

$$w_k = \frac{\alpha_k}{\alpha_0 + \alpha_1 + \alpha_2} \quad (8.69)$$

para $k = 0, 1, 2$, y

$$\alpha_k = \frac{C_k}{(\epsilon + IS_k)^2} \quad (8.70)$$

donde $C_0 = 0.2$, $C_1 = 0.2$ y $C_2 = 0.6$ son los pesos óptimos , (recordar que los pesos lineales óptimos para el método WENO5 son $C_0 = 0.1$, $C_1 = 0.6$ y $C_2 = 0.3$, ver [13]).

A partir de Jiang and Shu, (ver [13]), definimos el indicador de suavidad de cada una de las parábolas involucradas como la suma ponderada de las normas L^2 de todas las derivadas de la parábola calculadas en la celda computacional. Los pesos de esta suma son los pasos espaciales a la potencia correspondiente al orden de la derivada calculada. Estos pesos se utilizan para evitar la dependencia de estos indicadores de la malla espacial.

Si $p_k(x)$ es la parábola entonces

$$IS_k = \sum_{l=1}^2 \int_{x_{j-1/2}}^{x_{j+1/2}} h^{2l-1} (p_k^{(l)}(x))^2 dx$$

donde $p_k^{(l)}(x)$ es la derivada l -ésima de la parábola $p_k(x)$.

Utilizando esta elección tenemos la siguiente propiedad:

$$IS_k = D(1 + O(h^2))$$

donde D es una cantidad distinta de cero independiente de la parábola p_k , en todas las regiones suaves. Si la última propiedad está asegurada entonces la precisión óptima de quinto orden se alcanza. En nuestro caso obtenemos la siguiente expresión para los indicadores de suavidad:

$$IS_0 = \frac{13}{12} \left(P_{j-\frac{1}{2}} \right)^2 + \frac{1}{4} \left(2v_j - 2v_{j-1} + P_{j-\frac{1}{2}} \right)^2 \quad (8.71)$$

$$IS_1 = \frac{13}{12} (v_{j-1} - 2v_j + v_{j+1})^2 + \frac{1}{4} (v_{j-1} - v_{j+1})^2 \quad (8.72)$$

$$IS_2 = \frac{13}{12} \left(P_{j+\frac{1}{2}} \right)^2 + \frac{1}{4} \left(2v_{j+1} - 2v_j - P_{j+\frac{1}{2}} \right)^2 \quad (8.73)$$

donde P es el limitador powereno o powermod, calculados para dos diferencias de segundo orden contiguas.

Con esto, el método que resulta es un método de quinto orden de precisión que pondera el Power ENO , que llamaremos método Weighted Power ENO .

Comparamos con los indicadores que se obtienen para el método WENO5 de Jiang-Shu (see [13]):

$$IS_{0_{weno5}} = \frac{13}{12} (v_{j-2} - 2v_{j-1} + v_j)^2 + \frac{1}{4} (v_{j-2} - 4v_{j-1} + 3v_j)^2$$

$$IS_{1_{weno5}} = \frac{13}{12} (v_{j-1} - 2v_j + v_{j+1})^2 + \frac{1}{4} (v_{j-1} - v_{j+1})^2$$

$$IS_{2_{weno5}} = \frac{13}{12} (v_j - 2v_{j+1} + v_{j+2})^2 + \frac{1}{4} (3v_j - 4v_{j+1} + v_{j+2})^2$$

Observamos que el indicador central es exactamente el mismo.

Los desarrollos de Taylor de (8.71), (8.72) y (8.73) en regiones suaves son

$$IS_0 = \frac{13}{12} (u''h^2)^2 + \frac{1}{4} \left(2u'h - u''h^2 + \frac{1}{6}u'''h^3 \right)^2 + O(h^6)$$

$$IS_1 = \frac{13}{12} (u''h^2)^2 + \frac{1}{4} \left(2u'h + \frac{1}{3}u'''h^3 \right)^2 + O(h^6)$$

$$IS_2 = \frac{13}{12} (u''h^2)^2 + \frac{1}{4} \left(2u'h - u''h^2 + \frac{1}{6}u'''h^3 \right)^2 + O(h^6)$$

y por lo tanto tenemos las mismas ventajas que las obtenidas para el método WENO5 de Jiang-Shu.

En el Capítulo 4 de la Memoria comparamos la medida de suavidad de nuestro método Weighted PowerENO y la del WENO en regiones suaves y cerca de puntos críticos (discontinuidades de salto y en derivada) mediante la reconstrucción de funciones específicas que contienen estos puntos críticos.

8.4.2.3 Algoritmo del método Weighted PowerENO method

Sean v_{j-2} , v_{j-1} , v_j , v_{j+1} y v_{j+2} los datos necesarios (*stencil*) para calcular la aproximación lateral en $x_{j-\frac{1}{2}}$ y $x_{j+\frac{1}{2}}$.

Calculamos $d_{j-\frac{1}{2}}$ y $d_{j+\frac{1}{2}}$ como en (8.38), d_j como en (8.55), y D_{j-1} , D_j y D_{j+1} como en (8.56).

Con estos valores podemos calcular $P_{j-\frac{1}{2}} = \text{powereno}(D_{j-1}, D_j)$ y $P_{j+\frac{1}{2}} = \text{powereno}(D_j, D_{j+1})$ como se explicó en la sección 8.3 y entonces, calculamos IS_0 , IS_1 and IS_2 utilizando las expresiones (8.71), (8.72) y (8.73).

- Para la aproximación en $x_{j+\frac{1}{2}}$, calculamos:

$$a_0 = \frac{0.2}{\sqrt{\epsilon + IS_0}}, \quad a_1 = \frac{0.2}{\sqrt{\epsilon + IS_1}}, \quad a_2 = \frac{0.6}{\sqrt{\epsilon + IS_2}}$$

$$w_0 = \frac{a_0}{a_0 + a_1 + a_2}, \quad w_1 = \frac{a_1}{a_0 + a_1 + a_2}, \quad w_2 = \frac{a_2}{a_0 + a_1 + a_2}$$

Considerando expresiones simples para las paráolas (8.62), (8.63) y (8.64) en la interfase derecha $x_{j+\frac{1}{2}}$,

$$p_{j-\frac{1}{2}}(x_{j+\frac{1}{2}}) = v_j + \frac{1}{2}d_{j-\frac{1}{2}} + \frac{1}{3}P_{j-\frac{1}{2}}$$

$$p_j(x_{j+\frac{1}{2}}) = v_j + \frac{1}{2}d_j + \frac{1}{12}D_j$$

$$p_{j+\frac{1}{2}}(x_{j+\frac{1}{2}}) = v_j + \frac{1}{2}d_{j+\frac{1}{2}} - \frac{1}{6}P_{j+\frac{1}{2}}$$

obtenemos la aproximación a partir de la combinación convexa:

$$w_0 \cdot p_{j-\frac{1}{2}}(x_{j+\frac{1}{2}}) + w_1 \cdot p_j(x_{j+\frac{1}{2}}) + w_2 \cdot p_{j+\frac{1}{2}}(x_{j+\frac{1}{2}})$$

- Para la aproximación en $x_{j-\frac{1}{2}}$, calculamos:

$$a_0 = \frac{0.6}{\sqrt{\epsilon + IS_0}}, \quad a_1 = \frac{0.2}{\sqrt{\epsilon + IS_1}}, \quad a_2 = \frac{0.2}{\sqrt{\epsilon + IS_2}}$$

$$w_0 = \frac{a_0}{a_0 + a_1 + a_2}, \quad w_1 = \frac{a_1}{a_0 + a_1 + a_2}, \quad w_2 = \frac{a_2}{a_0 + a_1 + a_2}$$

Consideramos las expresiones simples para las paráolas (8.62), (8.63) y (8.64) en la interfase de la izquierda $x_{j-\frac{1}{2}}$,

$$p_{j-\frac{1}{2}}(x_{j-\frac{1}{2}}) = v_j - \frac{1}{2}d_{j-\frac{1}{2}} - \frac{1}{6}P_{j-\frac{1}{2}}$$

$$p_j(x_{j-\frac{1}{2}}) = v_j - \frac{1}{2}d_j + \frac{1}{12}D_j$$

$$p_{j-\frac{1}{2}}(x_{j+\frac{1}{2}}) = v_j - \frac{1}{2}d_{j+\frac{1}{2}} + \frac{1}{6}P_{j+\frac{1}{2}}$$

obtenemos la aproximación a partir de la combinación convexa:

$$w_0 \cdot p_{j-\frac{1}{2}}(x_{j-\frac{1}{2}}) + w_1 \cdot p_j(x_{j-\frac{1}{2}}) + w_2 \cdot p_{j+\frac{1}{2}}(x_{j-\frac{1}{2}})$$

8.5 Experimentos Numéricos

En el Capítulo 5 de la Mamoria se pone a prueba numéricamente el comportamiento de los procedimientos de reconstrucción propuestos anteriormente.

Implementamos los esquemas de alto orden de captura de ondas de choque basándonos en la llamada “flux formulation” de Shu y Osher ([36]). Para ser consistentes con la precisión espacial, la discretización en tiempo de los esquemas

bajo estudio se implementa mediante el método de tercer orden TVD Runge-Kutta desarrollado por Shu y Osher ([36]).

Formulamos las ecuaciones de Euler en dos dimensiones proporcionando las expresiones explícitas de la descomposición espectral de los Jacobianos que son necesarios para la implementación del algoritmo.

Describimos la implementación numérica que utilizamos para sistemas de leyes de conservación. Esta basada en la fórmula de flujo de Marquina (MFF) de primer orden que precisa de la descomposición espectral de los jacobianos de los flujos.

En la sección 5.4 de la Memoria se realiza un estudio numérico del esquema de tercer orden Power PHM para la advección lineal con datos iniciales que contienen discontinuidades de salto y en derivada, y se compara con el método PHM.

Se realizan diversos experimentos en una y dos dimensiones con las ecuaciones de Euler donde se observa una mejora sensible de la resolución de las discontinuidades y los extremos locales del método Power PHM respecto del PHM.

La sección 5.5 de la Memoria la dedicamos al estudio numérico del esquema Weighted PowerENO. En primer lugar realizamos un análisis de la precisión incluyendo tablas de errores y órdenes numéricos del esquema de quinto orden utilizando la ecuación de la advección lineal con datos suaves. A continuación realizamos un conjunto de experimentos numéricos donde comparamos la resolución de nuestro esquema de quinto orden con el WENO5 para la advección lineal de datos suaves a trozos y diversos problemas de valores iniciales para las ecuaciones de Euler en una y dos dimensiones. Observamos una mejora sustancial de nuestro esquema en las discontinuidades de contacto y en los extremos locales

donde la reducción de viscosidad numérica es evidente.

Todos estos resultados numéricos y sus representaciones gráficas se encuentran en el Capítulo 5 de la Memoria.

8.6 Aplicaciones: Simulaciones Numéricas de inestabilidades de Rayleigh-Taylor y Richtmyer-Meshkov

En el Capítulo 6 de la Memoria aplicamos los esquemas numéricos propuestos a la reolución de inestabilidades de Rayleigh-Taylor y Richtmyer-Meshkov. Introducimos el modelo de fluidos compresible multicomponente en dos dimensiones y calculamos el Jacobiano de los flujos correspondiente.

Realizamos simulaciones numéricas en una y dos dimensiones de la evolución de una interfase entre dos gases ideales perturbados por una onda de choque a Mach 1.52 y analizamos los resultados para los diferentes esquemas.

8.7 Resumen y Conclusiones

Hemos introducido nuevos métodos de captura de ondas de choque que reducen la difusión numérica en las discontinuidades, definen nítidamente las discontinuidades en derivada y evitan las oscilaciones espúreas, mejorando el comportamiento de los esquemas esencialmente no oscilatorios y los métodos hiperbólicos a trozos. Hemos introducido y analizado en este trabajo una nueva clase de funciones limitadoras, los llamados “power limiters” que son una herramienta esencial para la construcción de estos esquemas. Hemos utilizado el limitador

“powereno” como limitador de pendiente para el diseño de un nuevo método hiperbólico a trozos que llamamos método Power PHM. También hemos utilizado el limitador powereno aplicado a segundas diferencias contiguas para construir el método Power ENO. Hemos analizado un nuevo método de quinto orden de precisión espacial, el método Weighted PowerENO, como una combinación convexa no lineal de las tres paráolas PowerENO. Hemos comprobado la robustez, estabilidad y precisión de los esquemas propuestos para un conjunto de problemas modelo mediante varios experimentos numéricos. Finalmente hemos demostrado la capacidad de los esquemas presentados en la resolución de las escalas finas en el entorno de interfases inestables mediante el cálculo de inestabilidades de Rayleigh-Taylor y Richtmyer-Meshkov.

Como comentario general acerca de las ventajas de los esquemas propuestos hacemos las siguientes observaciones.

El método de tercer orden Power PHM mejora el comportamiento del PHM en los extremos locales y en las discontinuidades de contacto y comparte las ventajas del PHM. Puesto que estos esquemas son compactos, el Power PHM es más recomendable que el PHM cuando esta condición es conveniente para el cálculo, (e.g. esquemas de relajación).

Nuestro método de quinto orden Weighted Power ENO mejora el comportamiento del WENO reduciendo la viscosidad numérica en las discontinuidades de contacto y en los extremos locales. Captura escalas más finas para una malla computacional fija. Nuestro esquema es recomendable cuando la alta precisión es un objetivo y también cuando se tratan esquemas numéricos y simulaciones en

las que un stencil reducido no es necesario.

La mayor parte de la investigación presentada en este trabajo es general y no se restringe a las ecuaciones de Euler de la dinámica de gases y, por lo tanto, los resultados teóricos podrían ser aplicados a muchos otros problemas. De hecho, la nueva clase de limitadores y los procedimientos de reconstrucción pueden ser utilizados también con otras técnicas para el cálculo del flujo numérico como los esquemas centrados y las ecuaciones de Hamilton-Jacobi. Esta investigación prospectiva esperamos desarrollarla en un futuro próximo.

REFERENCES

- [1] R. Artebrant and H. J. Schroll, *High-resolution Riemann-solver-free methods for conservation laws*, Hyperbolic Problems: Theory, Numerics, Applications, pp. 305–314, Springer, Berlin, 2003.
- [2] R. Artebrant and H. J. Schroll *Conservative logarithmic reconstructions and finite volume methods*, (to appear in SIAM J. Sci. Comput.) (2004)
- [3] R. Courant and K.O. Friedrichs, *Supersonic Flow and Shock Waves*, Springer-Verlag, New York, (1976).
- [4] R. Donat and A. Marquina, *Capturing shock reflections: an improved Flux Formula*, J. Comput. Phys., 125 (1996), pp. 42–58.
- [5] B. Engquist and S. Osher, *Stable and entropy satisfying approximations for transonic flow calculations*, Math. Comp., vol. 34, pp. 45–75, (1980).
- [6] A. F. Emery, J. Comput. Phys., 2, 306 (1968).
- [7] R.P. Fedkiw, A. Marquina and B. Merriman, *An isobaric fix for the over-heating problem in multimaterial compressible flows*, J. Comput. Phys., 148 (1999), pp. 545–578.
- [8] S.K. Godunov, *A Finite Difference Method for the Numerical Computation of Discontinuous Solutions of the Equations of Fluid Dynamics*, Matematicheskii Sbornik, 47,p. 271 (1959).
- [9] Gottlieb, D. and Orszag, S. A., *Numerical Analysis of Spectral Methods: Theory and Applications*, SIAM, Philadelphia, (1977).
- [10] G. H. Hardy, J. E. Littlewood and G. Polya, *Inequalities*, Cambridge University Press, Cambridge (1973).
- [11] A. Harten, *High resolution schemes for hyperbolic conservation laws*, J. Comput. Phys., 49, (1983), pp. 357–393.
- [12] A. Harten, B. Engquist, S. Osher and S. Chakravarthy, *Uniformly high order accurate essentially non-oscillatory schemes III*, J. Comput. Phys., 71, No. 2, (1987), pp. 231–303.
- [13] G.S. Jiang and C. W. Shu, *Efficient Implementation of weighted ENO schemes*, J. Comput. Phys., 126, (1996), 202–228.

- [14] D. Kroener, *Numerical Schemes for Conservation Laws*, Wiley-Teubner, Chichester, (1997).
- [15] P.D. Lax, *Weak solutions of nonlinear hyperbolic equations and their numerical computation*, Commun. Pure Appl. Math., 7 (1954), pp. 159–193.
- [16] P.D. Lax, *The mathematical theory of shock waves. Regional Conference Series Lectures in Applied Mathematics*, 11, SIAM, Philadelphia, (1973).
- [17] P. D. Lax and B. Wendroff, *Systems of Conservation Laws*, Appl. Math., 13, (1960), 217-237.
- [18] S. Li and L. Petzold, *Moving mesh methods with upwinding schemes for time-dependent PDEs*, J. Comput. Phys., 131,(1997), pp. 368–377.
- [19] R.J. LeVeque *Numerical methods for conservation laws*, Birkhauser Verlag , Zuerich, (1990).
- [20] X-D. Liu and S. Osher and T. Chan *Weighted essentially non-oscillatory schemes*, J. Comput. Phys., 115, (1994), 200–212.
- [21] A. Marquina, *Local piecewise hyperbolic reconstructions for nonlinear scalar conservation laws*, SIAM J. Sci. Comput., 15,(1994), pp. 892–915.
- [22] A. Marquina and P. Mulet, *A flux-split algorithm applied to conservative models for multicomponent compressible flows* , J. Comput. Phys., 185, (2003), pp. 120–138.
- [23] A. Marquina and S. Serna, *Afternotes on PHM: Harmonic ENO methods*, Proceedings of the Ninth International Conference on Hyperbolic Problems: Theory, Numerics, Applications, HYP2002, Caltech, Pasadena, (California), (2002) , Springer, (in press).
- [24] E.E. Meshkov, NASA Tech T F, vol 13 p.74 (1970)
- [25] W. Mulder, S.J. Osher, J. Sethian, *Computing interface motion in compressible gas dynamics* , J. Comput. Phys., 100, (1992), pp. 209–228.
- [26] S. J. Osher, *Riemann solvers, the entropy condition and difference approximations*. SIAM J. Numer. Anal., 21, (1984), pp. 339–374.
- [27] S. J. Osher and S. Chakravarty, *High resolution schemes and the entropy condition*, SIAM J. Numer. Anal., 21, (1984), pp. 955–984.
- [28] R. Richtmyer, *Taylor instability in shock acceleration of compressible fluids*, Commun. Pure Appl. Math., 23, (1960), pp. 297–319.

- [29] A. Rogertson and E. Meiburg, *A Numerical Study of the Convergence of ENO schemes*, J. Sci. Comp., 5,(1990), 151–167.
- [30] H. J. Schroll , *High resolution relaxed upwind schemes in gas dynamics* , J. Sci. Comput., 17 (2002) pp. 599–607.
- [31] H. J. Schroll , *Relaxed high resolution schemes for hyperbolic conservation laws* , J. Sci. Comput., 21, 2, (2004).
- [32] C.W. Schulz-Rinne, J.P. Collins, and H.M. Glaz, *Numerical Solution of the Riemann problem for two-dimensional gas dynamics* , SIAM J. Sci. Comput., 14, (1993), pp. 1394–1414.
- [33] S. Serna and A. Marquina, *Power ENO Methods: A fifth order accurate Weighted Power ENO method*, J. Comput. Phys., 194, (2004), pp. 632–658.
- [34] J. Shi, YT Zhang, CW Shu, *Resolution of high order WENO schemes for complicated flow structures*, J. Comput. Phys., 186, (2003), pp. 690–696.
- [35] C. W. Shu, *Numerical Experiments on the Accuracy of ENO and modified ENO schemes*, J. Sci. Comp., 5, (1990), 127–150.
- [36] C. W. Shu and S. J. Osher, *Efficient Implementation of Essentially Non-Oscillatory Shock Capturing Schemes II*, J. Comput. Phys., 83, (1989), 32–78.
- [37] J. Smoller, *Shock Waves and Reaction-Diffusion Equations*, Springer Verlag, New York, (1983)
- [38] G. Sod, *A Survey of Several Finite Difference Methods for Systems of Non-linear Hyperbolic Conservation Laws*, J. Comput. Phys., 27, (1978), 1–31.
- [39] Y. Stiriba, *A nonlinear flux split method for hyperbolic conservation laws* , J. Comput. Phys., 176, (2002), pp. 20–39.
- [40] B. Van Leer, *Towards the ultimate conservative difference scheme V. A second order sequel to Godunov’s method*, J. Comput. Phys., 32,(1979), p.101–136.
- [41] P. Woodward and P.Colella, *The Numerical Simulation of Two-Dimensional fluid flow with strong shocks*, J. Comput. Phys., 54, (1984), 115–173.
- [42] YN Young, H. Tufo, A. Dubey, R. Rosner, *On the miscible Rayleigh-Taylor instability: two and three dimensions*, J. Fluid. Mech., 447,(2001), p.377-408.

